RTTOV-9

SCIENCE AND VALIDATION REPORT

Roger Saunders[1],

with contributions from

Marco Matricardi[2], Alan Geer[2], Peter Rayer[1]
and
Owen Embury[3] and Chris Merchant[3] for Annex A

Affiliations:
[1]Met Office, U.K.
[2]European Centre for Medium Range Weather Forecasts
[3]Edinburgh University

This documentation was developed within the context of the EUMETSAT Satellite Application Facility on Numerical Weather Prediction (NWP SAF), under the Cooperation Agreement dated 1 December, 2006, between EUMETSAT and the Met Office, UK, by one or more partners within the NWP SAF. The partners in the NWP SAF are the Met Office, ECMWF, KNMI and Météo France.

Change record			
Version	Date	Author / changed by	Remarks
0.1	18 Mar 08	R W Saunders	First draft version
0.2	22 Oct 08	R W Saunders	Draft to co-authors for comment
0.3	12 Nov 08	R W Saunders	Modified according to comments from co-authors
1.0	13 Nov 08	R W Saunders	Version ready for release
1.1	13 Oct 10	R W Saunders	Updated lgradp text in 2.8

Table of contents

1. Introduction and Documentation

The purpose of this report is to document the scientific aspects of the latest version of the NWP SAF fast radiative transfer model, referred to hereafter as RTTOV-91, which are different from the previous model RTTOV-87 and present the results of the validation tests which have been carried out. The enhancements to this version, released in March 2008, have been made as part of the activities of the EUMETSAT NWP-SAF. The RTTOV-91 software is available to users on request from the NWP SAF (email: mailto:nwpsaf@metoffice.gov.uk). The RTTOV-91 documentation can be viewed on the NWP SAF web site at: http://www.metoffice.gov.uk/research/interproj/nwpsaf/rtm/ which may be updated from time to time. Technical documentation about the software can be found in the RTTOV-9 user's guide which is also available and can be downloaded from the RTTOV web site at the link above. The latest versions of the documentation are included in the RTTOV-91 distribution file.

The baseline document for the original version of RTTOV is available from ECWMF as Eyre (1991). This was updated for RTTOV-5 (Saunders *et. al.* 1999a, Saunders *et. al.,* 1999b) and for RTTOV-6 with the RTTOV-6 science and validation report hereafter referred to as R6REP2000, for RTTOV-7 with the RTTOV-7 science and validation report hereafter referred to as R7REP2002, and for RTTOV-8 with the RTTOV-8 science and validation report hereafter referred to as R8REP2006 all available from the NWP SAF web site at the link above. The changes described here only relate to the scientific differences from RTTOV-87. For details on the technical changes to the software, user interface etc. the reader is referred to the RTTOV-91 user manual.

2. Scientific Changes from RTTOV-8 to RTTOV-9

2.1 Changes to computation of gaseous transmittances

The original basis for the RTTOV fast computation of transmittances is based on Eyre and Woolf (1988). This was successively modified for RTTOV by Eyre (1991), Rayer (1995), Rizzi and Matricardi (1998), Saunders *et. al.* (1999b) and Matricardi *et. al.* (2004) to the point that forward model computed transmittances are at an accuracy below the instrument noise of most sensors for RTTOV-7. However use of RTTOV-7 in NWP data assimilation runs have demonstrated that in some cases of extreme water vapour profiles anomalous values in the water vapour jacobians have been seen especially for AIRS simulations but also noted in AMSU-A simulations. This has provided motivation to update the water vapour transmittance computation. Another motivation is that the new line-by-line (LbL) transmittances provide the option of separating the water vapour line and continuum absorption which allows for a more flexible update of the spectroscopic datasets. A third motivation is the requirement to simulate IASI radiances which are at much higher spectral resolution than previous sensors simulated by RTTOV and finally the requirement to simulate more trace gases has required an update to the prediction scheme. As a result RTTOV-9 has been provided with 3 options for computing the atmospheric transmittance the original RTTOV-7 scheme, the RTTOV-8 scheme, for backward compatibility, and a new scheme in RTTOV-9 but only for high resolution spectral sounders (e.g. AIRS and IASI). The

latter is based on the predictors and the updated set of line by line transmittances as described in Matricardi (2008).

The simulation of transmittances in RTTOV is based on a regression scheme with a variety of predictors from the profile variables which are related to the layer optical depth, ($d_{i,j}$ - $d_{i,j-1}$), where $d_{i,j}$ is the level to space optical depth from level *j* and channel *i.* The regression is actually performed in terms of its departure from a reference profile, for mixed gases, water vapour, ozone etc. For RTTOV the formulation is:

$$d_{i,j} = d_{i,j-1} + \sum_{k=1}^{K} a_{i,j,k} X_{k,j} \qquad (1)$$

where *K* is the number of predictors and their definitions (i.e. $X_{k,j}$) are given in Tables 1 to 4 in the R8REP2006. For the new RTTOV-9 predictors developed for the high resolution IR sounders Tables 1 to 4 define them for each variable gas. $a_{i,j,k}$ are the regression coefficients provided in the coefficient files with each release of RTTOV. For the RTTOV-9 predictors three new variable gases have been added (i.e. methane, nitrous oxide and carbon monoxide). To compute the regression coefficients the spectral range from 645 cm^{-1} to 2760 cm^{-1} has been divided into 16 sub-sets and computed LbL transmittances for the combinations of gases shown in Table 5. It can be seen that all the terms but the one accounting for the correct total convolved transmittance cancel (in each spectral range only those molecules that contribute to the total absorption are included). The effective optical depths predicted by the fast model are the quantities obtained by taking the ratio of the LbL optical depths as shown in Table 5. The new predictors and their generation are described in more detail in Matricardi (2008).

All the variable gases except water vapour are optional and the computation can be turned off with a logical switch (e.g. ozone is off for all microwave channels) and the appropriate coefficient file with only the required coefficients. The coefficient file defines which set of optical depth predictors to use (RTTOV-7 or 8 or 9) and which gases to include as variable. Note if the gas is not assigned as variable it must be included within the 'fixed gas' coefficients.

2.2 The addition of a reflected solar radiance contribution

In RTTOV-9 a solar contribution to the top of atmosphere radiance has been introduced that allows the solar radiance to be computed that is transmitted through the atmosphere and then partially reflected back upward through the atmosphere. Since solar radiation gives a significant contribution to the top of atmosphere radiance for the shorter wavelengths (<5 μm), the introduction of a solar term in RTTOV-9 may enable the daytime assimilation of the short wave sounding channels.

i) Perfectly diffusing surface following the Lambert law.

For a non-scattering atmosphere and in clear sky, the monochromatic radiance at the point of reflection at the surface can be written as

$$L_{\tilde{\nu}}^{\uparrow}(\tau^{\downarrow},\mu,\phi) = \frac{1}{\pi}\iint_{\Omega_{\oplus}} \rho_{\tilde{\nu}}(\mu,\phi,\mu',\phi')\,\mu'\,L_{\tilde{\nu}}^{\oplus}(-\mu',\phi')\,\tau_{\tilde{\nu}}^{\downarrow}(\mu')\,d\mu'\,d\phi' \qquad (2)$$

If $\vec{U}_r(\theta,\phi)$ is the unit vector pointing toward the receiver, then $L_{\tilde{\nu}}^{\uparrow}(\tau^{\downarrow},\mu,\phi)$ is the radiance reflected upward along the direction of the unit vector $\vec{U}_r(\theta,\phi)$ where μ denotes the cosine of the zenith angle θ and ϕ is the azimuth angle. On the right hand side of equation (2), $\rho_{\tilde{\nu}}$ is the bi-directional reflectance (it depends on the direction of the unit vector $\vec{U}_r(\theta,\phi)$ and on the direction of the unit vector pointing toward the source ($\vec{U}_s(\theta',\phi')$) and is generally a complex function of both), $L_{\tilde{\nu}}^{\oplus}(-\mu',\phi')$ is the solar radiance along the direction of the unit vector $\vec{U}_s(\theta',\phi')$ and $\tau_{\tilde{\nu}}^{\downarrow}(\mu')$ is the surface-to-space transmittance along the downward path through the atmosphere. Note that the integral in equation (2) has to be evaluated over the solar disk ($\Omega_{\oplus}$ is the solid angle subtended by the solar disk at the Earth).

For the case of solar radiance reflected by a land surface, a proper treatment of the solar term would then require the knowledge of the bi-directional reflectance of the considered surface. Given that the bi-directional reflectance is not currently available in RTTOV-9, we treat the reflecting surface as a perfect diffuser. For a Lambertian surface the bidirectional reflectance is constant and is equal to the surface albedo ρ^L. If $\tau_{\tilde{\nu}}^{\uparrow}(\mu)$ is the surface-to-space transmittance along the upward path through the atmosphere, then the reflected radiance that reaches the receiver is (see Matricardi (2003) for details):

$$L_{\tilde{\nu}}(\mu) = \frac{1}{\pi}\rho^L I_{\tilde{\nu}}^{\oplus}\mu_{\oplus}\tau_{\tilde{\nu}}^{\downarrow}(\mu_{\oplus})\tau_{\tilde{\nu}}^{\uparrow}(\mu) \qquad (3)$$

where $I_{\tilde{\nu}}^{\oplus}$ is the irradiance of the solar disk at the top of the atmosphere and $\mu_{\oplus}$ is the cosine of the solar zenith angle. Although a perfectly diffusing surface is an approximation, it can be used as a reasonable estimate for a variety of soil types.

ii) Calm sea surface. For an ideal flat water surface we have specular reflection and

$$\rho_{\tilde{\nu}}(\mu,\phi,\mu',\phi') = \delta(\mu-\mu')\delta(\phi-\phi'+\pi)\rho_{\tilde{\nu}}^F(\mu) \qquad (4)$$

where δ is the delta Dirac function and $\rho_{\tilde{\nu}}^F(\mu)$ is the reflectance obtained from the Fresnel's formula. For a flat water surface the solar radiance that reaches the receiver can then be written as:

$$L_{\tilde{\nu}}(\mu) = \frac{1}{\pi}\rho_{\tilde{\nu}}^F(\mu_{\oplus})I_{\tilde{\nu}}^{\oplus}\mu_{\oplus}\,\tau_{\tilde{\nu}}^{\downarrow}(\mu_{\oplus})\tau_{\tilde{\nu}}^{\uparrow}(\mu_{\oplus}) \qquad (5)$$

iii) Wind roughened water surface. A real water surface such as the ocean is roughened by the wind. However, since the radius of curvature of an ocean capillary wave is of the order of a

centimetre, whereas the wavelength of infrared radiation is typically between 3 and 15 microns, one can regard the water surface as being locally flat and study the reflection of infrared radiation by the water surface with an approximation that uses geometric optics. One can calculate the optical properties of the water surface (in our case the reflectivity) by first considering the reflection of light from a single mirror-like facet and then regard the water surface as a collection of all such facets, each randomly tilted with respect to the local horizon. As time passes, the tilt of a facet varies under the influence of the wind. When the open ocean reflects the solar disk, these fluctuating facets produce a pattern known as sun glint. The radiance reflected by the sea surface can then be obtained using the effective reflectivity computed by taking the average of the reflectivity of the flat-water surface over the statistical variations of the surface slopes.

To model the reflective characteristics of a wind-roughened water surface, RTTOV-9 follows the approach by Yoshimori et al. (1995). In this model the probability density of the wave slope obeys a Gaussian distribution whereas the spectrum of the wave slope is specified by the Joint North Sea Wave Project (Hasselmann *et. al.*1973) wave-spectral model. The computation of the total variance of the wave slope requires the knowledge of the inverse function of the dispersive relation of the full-gravity capillary wave. Since this dispersive relation of the full-gravity capillary wave cannot be inverted analytically, pre-computed values of the inverse function are available in RTTOV-9 for a water depth of 50m (deep water approximation). Note that in RTTOV-9, the total variance of the slope depends on the wind speed, wind direction and wind fetch. The geometry of reflection of light by a wind-roughened water surface is shown in Figure 1. The origin of the coordinate system is in the point of reflection. The *X-Y* plane coincides with the mean sea level at the reflection point. The *X*-axis is the axis formed by the projection on the X-Y plane of the vector pointing towards the receiver, $\vec{U}_r(\theta,\phi)$. Since the *Z*-axis points towards the zenith, a right-handed system is formed. The angle χ is positive if the vector $\vec{U}_r(\theta,\phi)$ and $\vec{U}_s(\theta,\phi)$ are in opposite hemispheres, otherwise χ is negative. The angle α is positive if counted clockwise from the negative X-axis, negative is counted counter-clock wise. Finally, Ψ is the angle that the direction of the wind forms with the *X* axis.

For a wind-roughened water surface the solar radiance that reaches the receiver can then be written as:

$$L_{\tilde{\nu}}(\theta) \cong w_{\tilde{\nu}}(\theta,\chi^{\otimes},\alpha^{\oplus},\Psi)\ \ I_{\tilde{\nu}}^{\oplus}\ \ \tau_{\tilde{\nu}}^{\downarrow}\ \ \tau_{\tilde{\nu}}^{\uparrow} \qquad (6)$$

where $w_{\tilde{\nu}}(\theta,\chi^{\otimes},\alpha^{\oplus},\Psi)$ is the effective reflectivity of the water surface.

The solar source function $I_{\tilde{\nu}}^{\oplus}$ used in RTTOV-9 is based on theoretical radiative transfer calculations for the solar atmosphere made by Kurucz (1992). In the infrared spectral region it is strongly dependent on measurements made by the ATMOS instrument on the Space Shuttle. Equations (3), (5) and (6) give the monochromatic solar radiance that reaches the detector. To represent the solar radiance as viewed by the sensor, the spectrum of monochromatic radiances given by these equations must be convolved with the appropriate spectral response function. One can write

$$\hat{L}^{\uparrow}_{\tilde{\nu}^*}(\mu,\phi) = \int_{-\infty}^{+\infty} L^{\uparrow}_{\tilde{\nu}}(\mu,\phi)\, f(\tilde{\nu}^* - \tilde{\nu})\, d\tilde{\nu} \qquad (7)$$

where $f(\tilde{\nu}^* - \tilde{\nu})$ is the normalised spectral response function, $\tilde{\nu}^*$ is the central wave number of the channel and the circumflex over the symbol denotes convolution. In RTTOV-9 we assume that the atmosphere is the same along both downward and upward paths through the atmosphere. The product of the monochromatic transmittances $\tau^{\downarrow}_{\tilde{\nu}}(\mu_{\oplus})\,\tau^{\uparrow}_{\tilde{\nu}}(\mu)$ can then be written as:

$$\tau^{\downarrow}_{\tilde{\nu}}(\mu_{\oplus})\,\tau^{\uparrow}_{\tilde{\nu}}(\mu) = \tau_{\tilde{\nu}}(\mu_{eff}) \qquad (8)$$

Where $$\frac{1}{\mu_{eff}} = \frac{1}{\mu} + \frac{1}{\mu_{\oplus}} \qquad (9)$$

this is equivalent to saying that the reflected solar radiance depends on a single transmittance whose secant is equal to the sum of the secants of the viewing and solar zenith angles. Equation (6) can then be written as

$$L_{\tilde{\nu}}(\theta) \cong w_{\tilde{\nu}}(\theta,\chi^{\otimes},\alpha^{\oplus},\Psi)\;\; I^{\oplus}_{\tilde{\nu}}\;\; \tau_{\tilde{\nu}}(\mu_{eff}) \qquad (10)$$

The polychromatic form of the solar term then becomes

$$\hat{L}^{\uparrow}_{\tilde{\nu}^*} \cong \hat{I}_{\tilde{\nu}^*}{}^{\oplus}\;\; w_{\tilde{\nu}^*}(\theta,\alpha^{\oplus},\chi^{\oplus},\Psi)\;\; \hat{\tau}_{\tilde{\nu}^*}(\mu_{eff}) \qquad (11)$$

2.3 The fast transmittance model for the shortwave channels with solar radiation

Given the wide range of solar zenith angles, the computation of $\hat{\tau}_{\tilde{\nu}}(\mu_{eff})$ requires the evaluation of transmittances at zenith angles considerably larger than the ones involved in the computation of top of the atmosphere radiances in absence of solar radiation. The standard fast transmittance model used in RTTOV-9 can accurately simulate transmittances for zenith angles less then 64°. For the fast transmittance model to be able to simulate transmittances for a wider range of zenith angles, the database of line-by-line transmittances has been extended by computing data for an additional number of eight more path angles, namely, the angles for which the secant assumes the following values: 2.58, 3.04, 3.72, 4.83, 6.1, 7.2 and 9. This extended range allows the solar term to be estimated for zenith angles as large as $\approx 84°$. The larger range of zenith angles increases the difficulty of fitting the line-by-line optical depths. We have formulated a revised set of predictors to be used in the shortwave range only. The new set of predictors for the shortwave channels ($2000\,cm^{-1} \le \tilde{\nu}^* \le 2760\,cm^{-1}$) are tabulated in Tables 6-8 Note that in the spectral region $2250\,cm^{-1} \le \tilde{\nu}^* \le 2380\,cm^{-1}$ the standard predictors are used since in this region there is no contribution from the solar radiance. The definition of the profile variables used in the predictors

can be found in Table 4. In the spectral regions where the effect of reflected solar radiance is not included, the standard RTTOV-9 predictors are used (Tables 2-3).

2.4 Improvements to the atmospheric path length computation

The larger range of zenith angles involved in the computation of the solar term also has implications on the way the layer optical depths are evaluated in RTTOV-9. In the fast transmittance model the angular dependence of the optical depths is generally addressed by scaling the predictors through the secant of the local path angle. Ideally the satellite viewing angle (or the solar zenith angle) should be converted into a local path angle that decreases with altitude because of the curvature of the Earth and its surrounding atmosphere. This effect is largest at the maximum satellite viewing angle or at the maximum solar zenith angle and was ignored in previous versions of RTTOV where a constant local path angle is used throughout the atmosphere (i.e. plane parallel assumption).

The dependence of the local path angle on altitude has been explicitly introduced in RTTOV-9 by considering the geometry of the situation and the bending of rays as they traverse the atmosphere. The atmospheric layers are considered as concentric rings. If we trace a ray across these rings at any angle other than nadir, the local zenith angle relative to the vertical at the point of intersection will be different at each ring due to the curvature of the Earth and to atmospheric refraction. The local zenith angle at the bottom of each layer can be computed according to Snell's law and the sine of the local path angle at the bottom of layer *j* can be written as

$$\sin(\theta_j) = \sin(\theta_{sat}) \frac{R_{earth} + H_{sat}}{R_{earth} + h_j} \cdot \frac{n_{top}}{n_j} \qquad (12)$$

where θ_{sat} is the local satellite zenith angle, R_{earth} is the radius of the Earth for a given latitude, H_{sat} is the altitude of the satellite, h_j is the height of the bottom of layer *j*, n_j is the index of refraction of air through layer *j* and n_{top} is the index of refraction of air at the top of the atmosphere (0.005 hPa). Similarly for the solar zenith angle at the bottom of layer *j* we can write

$$\sin(\theta_j^{\oplus}) = \sin(\theta_s^{\oplus}) \quad \frac{R_{earth}}{R_{earth} + h_j} \quad \frac{n_s}{n_j} \qquad (13)$$

where $\theta_s^{\oplus}$ is the solar zenith angle at the surface and n_s is the index of refraction of air at the surface. The ratio of the refractive indices on the RHS of equations (12) and (13) is only applied if the refraction flag is set to true otherwise unity is assumed for this term. More details are given in Matricardi (2003).

2.5 The linear in τ approximation

In RTTOV-8 it was assumed the atmospheric layer can be considered to be sufficiently optically thin that equal weight can be given to radiance emitted from all regions within the layer, i.e. the average value of the Planck function is used. In the presence of optically thick layers only the upper regions of the layer give a significant contribution to the radiance. In this case the use of the average value of the Planck function would put too much weight on the radiance coming from the lower part of the layer. To improve the accuracy of radiance calculations in RTTOV-9, we have introduced a new parameterization of the Planck function based on the linear in τ assumption that the source function throughout the layer is linear with the optical depth of the layer:

$$B[T(\tau)] = B_0 + (B_1 - B_0)\frac{\tau}{\tau^*} \tag{14}$$

where B_0 is the Planck function for the top of the layer, B_1 is the Planck function at the bottom of the layer and τ^* is the optical depth of the layer. The parameterization is exact at the top ($\tau = 0$) and the bottom ($\tau = \tau^*$) of the layer. Based on Eq. (14), the radiance emitted by a homogeneous layer can be written as:

$$L_j = B_o(1 - e^{\frac{-\tau}{\mu}}) + (B_1 - B_o)\left[\frac{1 - e^{\frac{-\tau}{\mu}}}{\frac{\tau}{\mu}} - e^{\frac{-\tau}{\mu}}\right] \tag{15}$$

When the new formulation of the source function was introduced in RTTOV-9, the radiance error due to the use of the mean layer source function could be as large as 2degK if an optically thick water cloud is introduced in the radiative transfer. More details are given in Matricardi (2003).

2.6 Refinements in the Line-by-Line transmittance databases for coefficient generation

2.6.1 New diverse profile dataset

The diverse profiles computed from the ECMWF reanalysis have been updated for RTTOV-9 coefficient generation and are described in Chevallier *et. al.* (2006). A subset of 83 profiles has been generated from this new profile database for line-by-line transmittance calculations and the details are described in Matricardi (2008). Both documents are linked from the RTTOV web site and also the new profile datasets.

Briefly the improvements have been to extend the number of pressure levels to 91 and use the ERA-Interim reanalysis fields as the basis for the new profile dataset. There have also been improvements in the representation of ozone and the addition of variable trace gases now required for RTTOV-9 coefficient generation. Matricardi (2008) demonstrates the improvements

of the new profile set relative to the older 52 profile set used for RTTOV-8 and still used for RTTOV-9 microwave coefficient generation.

2.6.2 Infrared transmittances

There have been several updates to the infrared transmittances used in RTTOV over the past 10 years. The RTTOV-7 coefficient files are based on transmittances computed using the GENLN2 line-by-line model and the HITRAN-1996 line database with a 43 profile dataset derived from the TIGR profiles. This combination is still widely used for many of the infrared radiometers. To update the spectroscopic parameters for RTTOV-8 GENLN2 was rerun on a new set of 52 diverse profiles using more up to date spectroscopy from HITRAN-2002. In addition a set of RTTOV-8 coefficient files have also been produced using kCARTA to compute the transmittances (including separate continuum) and for AIRS and IASI these are what are used operationally at ECMWF and the Met Office at the time of writing. All these coefficients can still be used with the RTTOV-9 code and every coefficient file contains the details of the line-by-line model used and the profile dataset on which it is based in the header section.

For RTTOV-9 new coefficients, for clear sky optical depth calculations (including several new trace gases), have been computed using the LBLRTM line-by-line model (version 11.1) with a mix of HITRAN 2004 (with 2006 updates) and GEISA 2003 both based on the new 83 profile dataset. The LBLRTM model and HITRAN/GEISA combination was shown to give lower biases and variances between measurements and calculations from the ECMWF forecast model (Matricardi, 2008) as compared with only using HITRAN on its own. The generation of this new transmittance database is described in Matricardi (2008).

2.6.3 Refinements to microwave transmittances

A new set of microwave transmittances and coefficients has been generated for RTTOV-9. These are based on a modified version of the MPM-89/92 line-by-line model (Liebe, 1989 and Liebe *et. al*.,1993).

The MPM model has been modified to include ozone among the mixed gases using a climatological profile. This has been included in the mixed gas coefficient files for sensors like AMSU-B and SSMIS in channels that are affected by ozone lines. The effect of including ozone in the profile gases for AMSU-B channel 3 is, for a mid-latitude winter profile, to reduce by about 0.3K the top of atmosphere brightness temperature (John and Buehler, 2004). The implementation could be extended to include ozone as a variable gas, on the same basis as water vapour. However, the effect is a systematic reduction in brightness temperature, so the additional cost of another stage of prediction was not felt to be justified. In the present code, therefore, the prediction of the mixed gas transmittance includes, when appropriate, the effect of ozone at the abundance of the climatological profile.

The halfwidth of the 22 GHz water vapour line has been reduced in the MPM model to the more recent value given by the HITRAN molecular line database. This has removed systematic differences between measured and calculated brightness temperatures near the centre of the line (Liljegren *et. al.* 2005).

Comparisons between MPM and a fully polarized radiative transfer model (Kobayashi *et al.* 2008) has shown that the scalar approximation for the Zeeman effect in the MPM oxygen calculations is only adequate near the line centres. This affects simulations for AMSU-A channels 13-14 and SSMIS channels 19-22. As installed in the present line-by-line code, the same field strength is used for all transmittance paths, and no account is taken of the orientation of the magnetic field in each case. Results for AMSU-A channel 14, which has sidebands a few MHz off the centre of the 11$^-$ oxygen line, were found to be closer to a fully polarized calculation when the MPM scalar approximation was omitted. Hence RTTOV-9 coefficient files now omit the scalar approximation for the Zeeman effect. In the future RTTOV-9 will be updated with a fuller treatment for use with the high-peaking channels of AMSU-A and SSMIS but there is no representation of the Zeeman effect in the initial RTTOV-9 release.

RTTOV-9 coefficient files for water vapour are based on the model-based 52 profile set. These changes were found to remove anomalous values seen in the RTTOV-7 water vapour Jacobians for AMSU-A. Much of the improvement was due to the better representation of the model-based profile set. The newer profiles and optical depths from the modified MPM model, provide a more accurate forward calculation of microwave brightness temperatures and have been used for the RTTOV-9 microwave coefficients.

2.7 New profile interpolation

A new feature of RTTOV-9 is greater flexibility in the profile levels for input and output. The possibility of running with user-defined pressure levels when reading the profile and when integrating the radiative transfer equation has been introduced. The prediction of the optical depth due to gas absorption, still uses the pre-calculated coefficients $a_{i,j,k}$ that appear in equation (1), defined on a standard RTTOV defined set of pressure levels (normally 43 or 100 levels). With the interpolation option invoked the input profile on user levels are interpolated to coefficient levels for the prediction of the optical depths, and then these optical depths are interpolated back to user levels for the radiative transfer integration. It is preferable to return to user levels before the calculation of transmittances because the optical depths, cumulated from space to each level, provide a more appropriate variable for interpolation.

Each run of RTTOV-9 calculates the top of atmosphere brightness temperature T^B in each channel of a given sensor for the input profile of variables, and will include two sets of interpolations in opposite directions, one for profile variables X, and one for the accumulated optical depths, here referred to as D. This is shown schematically for the direct form of the code in

$$(X_u) \rightarrow \text{INT} \rightarrow (X_c) \rightarrow (D_c) \rightarrow \text{INT} \rightarrow (D_u) \rightarrow T^B{}_u \qquad (16)$$

where the subscript indicates user levels or coefficient levels and 'INT' refers to the interpolation operator. The brackets identify level-by-level column vectors, which means that, when X_u is a

scalar, like the surface pressure P_s, the first interpolation will be unnecessary. There is also a loop over all channels of the sensor for the second interpolation.

The corresponding tangent linear code, the incremental form obtained by differentiating (16), may be used to calculate the corresponding Jacobian vector for that channel brightness temperature, its sensitivity to individual changes, level-by-level, in the variable X. This, however, is done much more efficiently using the adjoint of the tangent linear code, which translates (16) into

$$\partial T^B{}_u / \partial T^B{}_u \rightarrow \left(\partial T^B{}_u / \partial D_u\right) \rightarrow \text{INT} \rightarrow \left(\partial T^B{}_u / \partial D_c\right) \rightarrow \left(\partial T^B{}_u / \partial X_c\right) \rightarrow \text{INT} \rightarrow \left(\partial T^B{}_u / \partial X_u\right) \qquad (17)$$

Again there are two sets of interpolations, although, when X_u is a scalar like P_s, the second interpolation will be unnecessary. The input on the left is just unity, and the output on the right is the Jacobian vector on user levels for variable X. Note that (17) supplies just one column vector of the Jacobian matrix for the variable, that relating to a single channel, so there will be a loop to cover all channels. The K code is a variant that will, if called instead, store the entire matrix for all levels and channels.

Many interpolators use the 'nearest neighbour' approach, in which the value for a variable on a given target level comes from an interpolation between values on the two nearest source levels above and below. However, when the RTTOV adjoint code is run, there may be a problem if the interpolator does not use *all* the source levels, because the information carried by the blind levels (i.e. those unused) carry information that is lost. The final Jacobian column on user levels, a channel sensitivity profile, may suffer significant distortion compared to the case where no interpolation has been performed.

The interpolator used in RTTOV-9 closely follows that described in Rochon *et al*. (2007) which has been designed to overcome this problem. It calculates a set of weights that, each time an interpolated value is required, will bring in *all* the source levels between the target level and its own neighbours above and below. Because it deals with triplets of target levels and the source levels used each time enter in a weighted sum, the method used is one of piecewise weighted averaging.

As well as the usual input profiles, the user interface calling RTTOV-9 has to provide additional inputs

- a logical switch to include or exclude the interpolation stage
- the number of user levels
- the corresponding pressure values on those user levels.

The number of user levels is expected to remain fixed for a set of profiles, but the pressure values may differ from one profile to the next in any run. The interpolation to coefficient levels is done immediately RTTOV-9 is called and the usual profile variable limit checks are then carried out on coefficient levels. This allows an early rejection of any profile that exceed the bounds of validity set for the coefficients.

Special considerations apply at the boundaries of the profile. Since the top target level cannot be the inner member of a triplet, the triplet is completed by introducing another level as far above (in pressure terms) as the next one below, and the same applies for the bottom target level. If the range of a target triplet extends above the topmost source level, a fake source level is created to coincide with the triplet top and assigned values by constant extrapolation. The usual procedure is then followed.

In a surface extrapolation of optical depth, this being the optical depth along the path from space, it is the *gradient* that is held fixed. Otherwise the additional layer of gas would become non-absorbing.

2.8 Interpolation with variable pressure levels

Using the internal RTTOV interpolation allows the user to provide input profiles on any pressure levels (and it is up to the user to ensure that the pressure levels adequately represent the atmosphere in terms of the vertical extent and resolution). When called with several profiles at a time, these input pressure levels can differ from profile to profile, and RTTOV will interpolate the atmospheric fields from the input pressure levels to the fixed pressure levels used in the optical depth calculations as required by the coefficient file. Throughout the code, input pressure levels are treated as a profile-specific variable.

In the default configuration of RTTOV, the input user pressure levels are assumed to be constant in the variational sense, ie., tangent linear perturbations for pressure levels or gradients/Jacobians with respect to the pressure levels are assumed to be zero. If the internal interpolation is activated, the *lgradp* option may be invoked by setting the logical variable *lgradp* to 'true'. The pressure assigned to a given vertical level will then be treated as a variable like, say, the temperature. This, for instance, can be used for 'sigma' coordinates commonly used in NWP. Setting *lgradp* to 'true' will allow the user to provide non-zero tangent linear perturbations for each input pressure level (and non-zero AD/K output), these being consistent with their own vertical coordinate specification.

Using *lgradp*, all assignments in the direct code that involve the input pressure, now a variable in the variational sense, will acquire extra terms in the tangent linear code, with consequent changes to the AD and K. For the default RTTOV case, this will only be true for the surface pressure, which has always been the case for RTTOV. Note that computations on the fixed pressure levels internally used by RTTOV for the optical depth calculations continue to be treated as constant in the variational sense, so they do not require tangent linear (AD/K) terms.

The use of *lgradp* also has implications for the interpolator. The direct and tangent linear forms of the interpolation may be written as

$$X'_i = \sum_j W_{ij} X_j \qquad (18)$$

$$dX'_i = \sum_j \left(W_{ij}\, dX_j + X_j\, dW_{ij} \right) \qquad (19)$$

where W_{ij} represents the weights applied to source values, either X_j or dX_j, for channel i and level j. Using *lgradp* = .false. means neglecting the dW_{ij}, since the weights are entirely determined by the pressure levels, and input as well as output pressure levels are assumed to be fixed in the variational sense. Using *lgradp* = .true. allows non-zero dW_{ij}, arising from non-zero perturbations of some of the pressure levels.

In summary, when *lgradp* is used, pressure is treated as a variable in the variational sense. For assignments throughout the direct code that involve the user input pressure levels, counterparts in the tangent linear code will acquire extra terms. For the option *lgradp* to work correctly, the internal interpolator has to be used.

2.9 Infrared cloud and aerosol affected radiance simulations

2.9.1 A scientific overview of the model

The parameterization of multiple scattering introduced in RTTOV-9 is performed by scaling the optical depths by a factor which is derived by including the backward scattering in the emission of a layer and in the transmission between levels. The introduction of multiple scattering allows RTTOV to simulate AIRS and IASI radiances in the presence of eleven different types of aerosol components, five different types of water clouds and 30 different types of ice clouds. Finally, to solve the radiative transfer for an atmosphere partially covered by clouds, RTTOV uses a scheme (stream method) that divides the field of view into a number of homogeneous columns, each column containing either cloud-free layers or totally cloudy layers. Each column is assigned a fractional coverage and the number of columns is determined by the cloud overlapping assumption (maximum-random overlap in RTTOV) and the number of layers the atmosphere is divided into. The total radiance is then obtained as the sum of the radiances for the single columns weighted by the column fractional coverage.

The basic methodology is documented in detail in Matricardi (2003) and Matricardi (2005). In the following sections we give a general description of the main components of the scattering model that was implemented in RTTOV-9.

2.9.2 The radiative transfer for multiple scattering

The scheme implemented in RTTOV to parameterize multiple scattering is based on the approach followed by Chou et al. (1999). In this scheme (referred to hereafter as scaling approximation), the effect of scattering is parameterised by scaling the optical depth by a factor derived by including the backward scattering in the emission of a layer and in the transmission between levels. Since this parameterisation of multiple scattering relies on the hypothesis that the diffuse radiance field is isotropic and can be approximated by the Planck function, it can be expected to have an effect on the accuracy of the radiance calculations. However, the scaling approximation

does not require explicit calculations of multiple scattering and since the radiative transfer equation is formulated in the same form as for clear sky conditions, the computational efficiency of RTTOV can be retained. In the scaling approximation the contribution of the thermal diffuse scattered radiation is simulated by replacing in the radiative transfer equation the absorption optical depth, τ_a, with an effective extinction optical depth, $\tilde{\tau}_e$, defined as:

$$\tilde{\tau}_e = \tau_a + b\tau_s \tag{20}$$

where τ_s is the scattering optical depth and b is the integrated fraction of energy scattered backward for incident radiation from above or below. If $\bar{P}(\mu,\mu')$ is the azimuthally averaged value of the phase function and μ is the cosine of the scattering angle, b can be written in the form:

$$b = \frac{1}{2}\int_0^1 d\mu \int_{-1}^0 \bar{P}(\mu,\mu')d\mu' \tag{21}$$

In the presence of solar radiation we have to consider the contribution of the solar scattering term. In RTTOV we assume that the solar scattering term and the thermal diffuse scattering term are independent which allows the solar term, the effective extinction optical depth, $\tilde{\tau}_e$, to be replaced by the canonical extinction optical depth, τ_e, defined as:

$$\tau_e = \tau_a + \tau_s \tag{22}$$

For a homogeneous atmospheric layer the contribution of the solar scattering term to the upward radiance from the layer, $I_{\otimes}^{\uparrow}$, can be written in the form:

$$I_{\otimes}^{\uparrow} = F_{\otimes}\varpi\mu_{\otimes}\frac{\bar{P}(\mu,-\mu_{\otimes})}{4\pi(\mu+\mu_{\otimes})}[1-e^{\frac{\tau_e}{\mu+\mu_{\otimes}}}] \tag{23}$$

where $F_{\otimes}$ is the solar irradiance at the top of the layer, ϖ is the single scattering albedo, $\mu_{\otimes}$ is the cosine of the solar zenith angle, μ is the cosine of the viewing angle, $\bar{P}(\mu,-\mu_{\otimes})$ is the azimuthally averaged value of the phase function and τ_e is the extinction optical depth of the layer. To evaluate the solar scattering term in RTTOV, the quantity $\bar{P}(\mu,-\mu_{\otimes})$ in Eq.(23) must be computed explicitly (similar considerations apply to the downward radiance). Since this involves solving of an integral numerically, the choice of the number of quadrature points can significantly affect the computational efficiency of the code and the accuracy of the results. The capability of RTTOV to process radiances in the presence of clouds required a revision of the way the Planck function, B, is parameterized in the radiative transfer equation as described in section 2.5.

2.9.3 The database of optical properties for aerosols

The introduction of scattering in the RTTOV radiative transfer requires the knowledge of the optical parameters for any of the atmospheric particulates to be included in the computations. Particulates contained in the Earth's atmosphere vary from aerosols, to water droplets and ice crystals. For aerosols, the range and shape vary from quasi-spherical to highly irregular with a size typically less that 1 μm although particles as large as 10 to 20μm have been observed. The interaction of a plane wave with a dielectric sphere can be solved exactly by the Lorentz-Mie theory of light scattering by spheres (Van de Hulst 1981). In RTTOV aerosols are assumed to have a spherical shape.

A database of optical properties has been generated using the microphysical properties assembled in the Optical Properties of Aerosols and Clouds (OPAC) software package (Hess et al. 1998). This database provides the microphysical properties (size distribution and refractive indices) for ten aerosol components. If *n(r)* is the size distribution function in units of particles per volume per radius *r*, then *n(r)dr* represents the number of particles per unit volume in the interval *(r, r+dr)*. The total number concentration, *N*, can then be written as:

$$N = \int_{r_{\min}}^{r_{\max}} n(r)dr \qquad (24)$$

where $r_{\min}$ and $r_{\max}$ are the minimum and maximum value of the particle radius range. To be able to simulate the radiative properties of the atmosphere in the presence of a volcanic eruption, we have supplemented the OPAC database with the microphysical properties of the volcanic ash component. Once the size distribution is known, we can write the extinction coefficient, β_e, in the form:

$$\beta_e = N\beta_e^1 = N\int_{r_{\min}}^{r_{\max}} \sigma_e(r)n^1(r)dr \qquad (25)$$

where σ_e, the extinction cross section, is computed using the Lorentz-Mie theory and $n^1(r)$ is the size distribution function normalized to 1 particle cm^{-3}. Note that, at least for aerosols and water clouds, the optical parameters stored in RTTOV are normalized to 1 particle cm^{-3} (e.g β_e^1). To obtain the general value the user must then provide, directly or indirectly, the value of the particle number concentration. The extinction optical depth for a homogeneous atmospheric layer can then be written as:

$$\tau_e = \beta_e \Delta z \qquad (26)$$

where Δz is the thickness of the layer. In RTTOV the units of β_e and Δz are km^{-1} and km respectively. The absorption and scattering extinction coefficients can be computed from Eq.(25) using the absorption and scattering cross sections. For the computation of the phase function and the backscatter parameter, *b* , the reader can refer to Matricardi (2005).

The values of the refractive indices were interpolated to the central wavelength of each channel and then used to compute the absorption coefficient, scattering coefficient, extinction coefficient, phase function and the backscattering parameter *b* defined in Eq. (20) for every single aerosol component. A lognormal size distribution was used for all the aerosol components except for the volcanic ash component for which a modified Gamma distribution was used. Values of the phase function were computed for every 0.1º from 0º to 3º otherwise they are given for every 1º. For those aerosols that can take up water, we have computed the optical properties for eight different values of the relative humidity assuming the width of the distribution does not change. The optical properties for an arbitrary value of the relative humidity can then by obtained by linear interpolation. Aerosols can be classified in terms of their location (i.e. continental, maritime, polar, etc.) and type (i.e. clear, polluted, desert, urban, etc.). Each aerosol type/location is composed of a mixture of several aerosol components. RTTOV can compute optical properties for any mixture of aerosol components or, alternatively, it can compute optical properties for ten aerosol types composed of pre-defined mixtures of aerosol components, each mixture forming a typical climatological aerosol. In the first case the user must provide, for each aerosol component, a vertical profile of aerosol number densities, in the second case the vertical profiles are provided as default in RTTOV.

To obtain the vertical profiles for the latter case we have applied the methods described in Hess et al. (1998). In particular, the surface number densities have been extrapolated to 35 km altitude assuming the atmosphere is divided up into three layers. The first layer is the planetary layer, the second represents the free troposphere and the third is the stratospheric layer. The upper boundary of the planetary layer is placed at 2 km with the exception of the Desert and Antarctic aerosol types for which the top of the layer is placed at 6 and 10 km respectively. The top of the free troposphere is always placed at 12 km and the stratosphere extends up to 35 km. The variation of the number densities with altitude is described by an exponential profile and a background concentration profiles is assumed in the free troposphere and stratosphere irrespective of the aerosol type. The composition of the 10 aerosol types is tabulated in Table 9 along with the surface number concentration for each component whereas the 11 aerosol components available in RTTOV are listed in Table 10.

2.9.4 The database of optical properties for water clouds

Water clouds are by their nature composed of spherical water droplets whose size ranges from ~1 μm to 20 μm. The OPAC package gives the microphysical properties for 5 types of water clouds: two stratus clouds (Stratus Continental and Stratus maritime) and 3 cumulus clouds (Cumulus Continental Clean, Cumulus Continental Polluted, and Cumulus Maritime) with the size distribution described by the modified Gamma distribution. The particle number concentration can be related to the cloud liquid water content, *LWC*, as follows:

$$LWC = \frac{4\pi}{3}\rho_l N \int_{r_{\min}}^{r_{\max}} r^3 n^1(r) dr \qquad (27)$$

where ρ_l is the density of liquid water. In Table 11 we have tabulated the values of *N* and *LWC* for the five size distributions given in the OPAC package. From Table 11, a scaling factor, *S*, can be derived in the form

$$S = \frac{LWC}{N} \qquad (28)$$

If the user wants to introduce a water cloud type in the RTTOV radiative transfer, an input value of LWC must be provided in one or more atmospheric layers. The liquid water content is then converted into the particle number concentration using Eq.(28). Once *N* is known, the absorption, scattering and extinction optical depths can be derived from the normalized values of the optical parameters stored in RTTOV using for instance Eq.(26).

Following the approach adopted for the database of optical properties for aerosols, we have firstly interpolated the refractive indices of water to the central wavelength of each channel and then used these values to generate a database of optical properties for every single water cloud type using the Lorentz-Mie theory of light scattering by spheres.

2.9.5 The database of optical properties for clouds cirrus

Optical properties for ice crystals are optionally available for randomly oriented hexagonal columns and for randomly orientated ice aggregates. 30 ice crystal size distributions are available in RTTOV.

The size and shape of ice crystals vary greatly from polar regions to midlatitudes to tropics. Typical shapes for ice crystals include bullet rosettes, hollow and solid columns, plates and aggregates. Columns and plates are predominant in the pristine regions on the top of the cloud, especially in midlatitude clouds. However, at the cloud bottom, because of the vertical mixing and gravitational pull, ice crystals tends to collide and to coalesce producing aggregates and bullet rosettes. Pristine hexagonal ice columns have often been used in the literature to represent the radiative properties of cirrus clouds and this was the choice originally made in RTIASI. However, recent measurements, although limited to only one cirrus case study, show that cirrus radiative properties might be better represented by ice aggregates (Baran and Francis 2004). Given the recent availability of a database of optical properties for ice aggregates (Baran and Francis 2004), the choice of representing the radiative properties of cirrus clouds in terms of either hexagonal ice columns or ice aggregates has been provided in RTTOV-9.

2.9.6 The optical properties for hexagonal ice columns

An exact solution for the interaction of a plane wave with a hexagonal ice crystal cannot be found using the Lorentz-Mie theory. The problem is complicated by the fact that there is no practical solution that can be used to cover all the crystal sizes that occur in the Earth's atmosphere. For the case when the size of an ice crystal is much larger that the wavelength of the incident radiation the only practical approach to solve the problem of light scattering is the Geometric Optics (GO) method (Takano and Liou 1989). The GO method is based on the assumption that a light beam is made of a bundle of parallel rays that undergo reflection and refraction outside and inside the crystal. The directions of propagation are determined using Snell's law at the surface of the crystal and the total field is made of the diffracted rays plus the reflected and refracted rays. For the problem of light scattering by small ice crystals a number of methods have been developed such as the Finite-Difference Time domain Method (FDTD) (Yang and Liou 1996) and the Direct Dipole Approximation (DDA) (Draine and Flatau 1994). An inherent shortcoming of these methods is that they are computationally expensive to the extent that they can become impractical if a solution is sought for randomly oriented particles. The most effective method for calculations of light scattering by small ice crystals is probably the T-matrix (Mishchenko 1991) that relates the incident and scattered fields by means of a T-matrix after they have been expanded in terms of spherical wave functions.

For RTTOV we have generated a composite database of optical properties for hexagonal ice crystals randomly oriented in space using the GO method for large crystals and the T-matrix method for small crystals. The publicly available codes developed by Macke et al. (1996) and Kahnert (2004) have been used respectively. The GO code uses the Monte Carlo method for geometric ray tracing and includes the contribution of absorption. The total phase function computed using the GO technique is a combination of the ray-tracing phase function and the Fraunhofer diffraction component. The standard GO method produces a ray-tracing phase function with strong and narrow peak in the forward scattering direction. This effect is an artefact of the GO technique that ignores physical optics effects and is known as δ-function transmission (Takano and Liou 1989). To reconcile the approximated GO results with exact results and produce a phase function with an angular profile similar to the diffraction component we have modified the GO code applying the methodology described in Mischenko and Macke (1998). Modifications to the GO code were also made to make it possible to compute the phase function at a number irregularly spaced angles.

Convergent results for the T-matrix code could only be obtained for the smaller and less elongated hexagonal columns. In fact part of the numerical procedure associated with the T-matrix method is a numerical matrix inversion. This can become an ill-conditioned problem that leads to non-convergent results if the size of the matrix is too large as is the case for the larger columns when a high number of expansion orders is required to expand the electromagnetic fields. The T-matrix computations have required extensive pre-processing. For a given crystal geometry the T-matrix code was not designed to give convergent results. The expansion orders needed to obtain convergent results (within a given accuracy) for a particular crystal size and frequency had to be determined by trial and error since no guidance was available for the geometries and refractive indices involved in this exercise. The wavelength range covered by each technique is given in Table 12.

The refractive indices of ice are important parameters in the computation of the scattering and absorption properties of ice crystals. For the hexagonal ice columns database we have used real refractive indices compiled by Warren (1984) for all wavelengths covered by IASI. Complex refractive indices compiled by Warren were also used for wavelengths longer than 7.8 μm. For wavelengths shorter than 7.8 μm more recent values of the complex refractive indices compiled by Gosse et al. (1996) have been used. In this spectral range they can differ from the ones compiled by Warren by as much as 30%. In the IASI spectral range, refractive indices for ice are tabulated at 89 different frequencies. Given the computational time required to perform the GO and T-matrix computations, the procedure of interpolating the refractive indices to the AIRS and IASI central frequencies and then perform the GO and T-matrix computations for each channel is impractical. We have instead performed computations for each of the 89 tabulated refractive indices and then interpolated the results to each AIRS and IASI channel. Since the refractive indices for ice are a slowly varying function of the wavelength, for any practical purpose we can consider the ice crystal optical properties to be constant over the width of a channel.

To represent the microphysical properties of ice clouds the 8 size distributions prepared by Heymsfield and Platt (1984) were used initially. These size distributions for mid-latitude cirrus are a function of temperature at 5ºC intervals from -20ºC to -60ºC. Given the availability of a wider range of observed ice crystal size distributions, in RTTOV we have complemented the 9 RTIASI size distributions with 22 additional size distributions from Fu (1996). The size distribution functions used in RTTOV are plotted in Figure 2. These size distributions are representative of cirrus clouds from mid-latitude regions (Heymsfield and Platt, Takano and Liou, FIRE I, FIRE II, and FU) and from tropical regions (CEPEX IWC and CEPEX). All the size distributions have been obtained from in situ aircraft observations. However, for the size distributions measured in mid-latitude regions, the technique used (optical array probes) could not allow the measure of particles smaller than 20-40 μm whereas the replicator sonde used in the tropical regions could measure the small ice crystals that cannot be measured by the optical array probes. To account for the radiative effect due to the presence of small ice crystals, the mid-latitude size distributions have been extrapolated to small values of the particle size assuming that the logarithm of the number concentration varies linearly with the logarithm of the particle dimension (Heymsfield and Platt 1984).

To compute the optical parameters for hexagonal ice crystals (see Eq.(25) for instance) we have discretized the size distributions into 24 bins. The midpoint crystal length, L, varies from 4μm to 3500μm and is tabulated in Table 13.

The width, D, of the crystal has been derived from the length, L, of the crystal using the aspect ratio given in Yang et al. (2003)

$$\frac{D}{L}=\begin{cases}1 & L\le 40\mu m\\ \exp(-0.017835(L-40)) & 40<L\le 50\mu m\\ \dfrac{5.916}{\sqrt{L}} & L>50\mu m\end{cases} \qquad (29)$$

For each ice crystal size distribution we define a generalized effective diameter, D_{ge}, in the form (Fu 1996):

$$D_{ge}=\frac{2\sqrt{3}\,IWC}{3\rho_l A_c} \qquad (30)$$

where IWC is the ice water content, ρ_i is the density of ice and A_c is the total cross-sectional area of the cloud particles per unit volume. The ice water content, IWC, can be related to the volume, V, of the crystal in the form:

$$IWC=\rho_l N\int_{L_{\min}}^{L_{\max}} V(L)n^1(L)dL \qquad (31)$$

For a randomly oriented hexagonal column the projected cross-sectional area is equal to one-quarter of its surface area. The generalized effective diameter for an ensemble of randomly oriented hexagonal columns can therefore be written as:

$$D_{ge}=\frac{\int_{L_{\max}}^{L_{\min}} D^2 Ln(L)dL}{\int_{L_{\max}}^{L_{\min}}[DL+\frac{\sqrt{3}}{4}D^2]n(L)dL} \qquad (32)$$

The values of the generalized effective diameter and ice water content for the size distributions considered in this study are tabulated in Table 14.

To generate the database of optical properties for randomly oriented ice crystals we have computed the absorption cross section, scattering cross section, extinction cross section, phase function at 208 angles, and asymmetry parameter for each ice crystal defined in Table 13 and then performed the convolution with the size distribution function (see Eq.(25) for instance) to obtain the optical properties for each sample of cloud particles. The optical properties for a selected number of ice crystal size distributions are plotted in Figures 3 and 4 for the IASI channels. Note how in most of the cases the value of the asymmetry parameter is consistently larger than 0.9 across the whole spectral range; this is a direct a result of the phase function with a strong and narrow peak in the forward direction.

The data from the 30 size distributions have been used to parameterize the absorption coefficient, the scattering coefficient, the extinction coefficient and the backscatter parameter, b, as a function

of *IWC* and D_{ge}. It can be shown that in the limit of geometric optics (i.e. the size of the crystal is much larger than the wavelength of the incident radiation), since the extinction cross section is twice the projected area A_c, the extinction coefficient β_e can be related to *IWC* and D_{ge} in the form

$$\beta_e = \frac{4\sqrt{3}}{3\rho_l}\frac{IWC}{D_{ge}} \tag{33}$$

Although a theoretical relationship cannot be derived for the more general case, we can still expect that the extinction coefficient, the scattering coefficient, the absorption coefficient, the backscatter parameter and, possibly, the phase function can be related to the ice water content and the generalized diameter. In RTTOV we assume that

$$\frac{\beta_e}{IWC} = r_{e,0} + r_{e,1}D_{ge} + \frac{r_{e,2}}{D_{ge}} + \frac{r_{e,3}}{D_{ge}^2} \tag{34}$$

$$\frac{\beta_s}{IWC} = r_{s,0} + r_{s,1}D_{ge} + \frac{r_{s,2}}{D_{ge}} + \frac{r_{s,3}}{D_{ge}^2} \tag{35}$$

$$\frac{\beta_a}{IWC} = r_{a,0} + r_{a,1}D_{ge} + \frac{r_{a,2}}{D_{ge}} + \frac{r_{a,3}}{D_{ge}^2} \tag{36}$$

$$b = r_{b,0} + r_{b,1}D_{ge} + r_{b,2}D_{ge}^2 + r_{b,3}D_{ge}^3 \tag{37}$$

where β_e is the extinction coefficient, β_s is the scattering coefficient, β_a is the absorption coefficient and b is the backscatter parameter. The expansion coefficients for each IASI and AIRS channel are computed by linear regression using the reference optical parameters and then stored in RTTOV. In this respect, RTTOV differs significantly to RTIASI where a less general approach was used. In RTIASI normalized optical parameters for the Heymsfield and Platt size distributions were stored in the code. One of the eight size distributions could be selected based on the temperature of the layer and a scaling factor was derived from Eq.(31) that relates ice water content and particle concentration. A value of the particle concentration was then obtained from the *IWC* value provided by the user and then used to compute the cirrus cloud optical depth from the normalized values of the optical parameters stored in the code.

The fitting for a selected number of parameters is shown in Figure 5 for IASI channel 1421 (wave number 1000 cm^{-1}).The black stars represent the reference values whereas the red squares represent the results from the parameterization. In RTTOV we also store the values of the phase function for each size distribution. The phase function is in fact not parameterized; for a given D_{ge}, values are obtained from the RTTOV database by linear interpolation.

To estimate the value of $D_{ge,}$ parameterizations are available that relate the generalized diameter to the ice water content and/or the temperature provided by the user. Since this capability was already present in RTTOV-8 (RTTOV_CLD), we have just retained it to be used with the new cloud model. The user can select four possible options: two of the options (Boudala et al. 2002, Wyser 1998) use both temperature and ice water content to predict $D_{ge,}$ one option (Ou and Liou 1995) uses the temperature and the final option (McFarquhar 2003) uses only the ice water content.

2.9.7 The optical properties for ice aggregates

The database of optical properties for randomly oriented ice aggregates used in RTTOV is described in Baran and Francis (2004). The exact aggregate geometry is due to Yang and Liou (1998) and consists of eight hexagonal columns attached to one other. In the Yang and Liou model the aspect ratio (i.e. the ratio of the major and minor axes of a circumscribed ellipse) does not vary with size and is close to unity. For wavelengths longer than 5 μm the database described in Baran and Francis (2004) has been computed using an approximate method that represents the complex geometry of the ice aggregates by a size/shape distribution of circular ice cylinders (Baran 2003). Simulated ice aggregates are assumed to be composed of ensembles of circular cylinders. The aspect ratio (i.e. diameter-to-length ratio) of the cylinders can vary but the volume-to-area ratio of the aggregate is conserved and is equal to the value of the exact aggregate geometry due to Yang and Liou (1998). For cylinders with maximum dimensions of 3-225 μm the optical parameters of the size/shape distribution of circular ice cylinders are computed using the T-matrix method (Mishchenko 1991) whereas for cylinders with maximum dimension up to 3500 μm optical parameters are computed using the complex angular momentum (CAM) method (Nussenz and Wiscombe 1980). For wavelengths less than 5μm the database is supplemented with optical parameters computed using the exact model due to Yang and Liou (1998). Note that the values of the phase function included in the database were not computed analytically but derived instead using a modified Henyey-Greenstein phase function (Baran et al. 2001). Values of the optical parameters are given at 65 wavelengths for each of 24 different values of the ice aggregate maximum dimension. The refractive indices for ice are from Warren (1984) and the midpoint crystal length, L, varies from 3μm to 3500μm. Note that apart from the first bin (3μm instead of 4μm) the values of the midpoint crystal length are the same as those in Table 13. The values of the generalized effective diameter and ice water content for the size distributions considered in this study are tabulated in Table 15.

The values tabulated in Table 15 have been obtained using Equations (30) and (31). The volume, V, and the projected area, A, of the ice aggregate have been computed using the methods described in Yang et al. (2000): the diameter of a sphere of equivalent area, D_a, and the diameter of a sphere of equivalent volume, D_v, are firstly related to the maximum dimension of the ice aggregate:

$$D_a = \exp[\sum_{n=0}^{4} a_n (\ln D_{\max})^n \qquad (38)$$

$$D_v = \exp[\sum_{n=0}^{4} b_n (\ln D_{\max})^n \quad (39)$$

The area and volume of the ice aggregate can then be written as:

$$A = D_a^2 \pi / 4 \quad (40)$$

$$V = D_v^3 \pi / 6 \quad (41)$$

The expansion coefficients a_n and b_n are derived by linear regression. Optical properties for ice aggregates have been computed for the AIRS and IASI channels interpolating the results obtained for the 65 values of the refractive indices. Results for the IASI channels are plotted in Figures 6 and 7. Values are shown for the same sample of size distributions used for the hexagonal ice crystals. It can be seen that the different crystal habit results in smaller values of the absorption, scattering and extinction coefficients. Following the approach used for hexagonal ice crystals we have parameterized the extinction coefficient, the scattering coefficient, the absorption coefficient, and the backscatter parameter using Equations (34), (35), (36), and (37). The fitting for a selected number of parameters is shown in Figure 8 for IASI channel 1421 (wave number 1000 cm^{-1}).The black stars represent the reference values whereas the red squares represent the results from the parameterization.

It should be mentioned that for all the scattering particles included in RTTOV-9 the optical properties have been computed on the basis of microphysical properties that, given their highly variable nature, do not necessarily reflect an actual situation. For this reason, RTTOV-9 allows the user to provide customised values of the optical properties used in the radiative transfer. The RTTOV-9 users guide gives a summary of the input profile configuration required by RTTOV to perform multiple scattering computations in the presence of aerosols and clouds.

2.9.8 The stream method

To solve the radiative transfer for a horizontally non-homogeneous atmosphere (i.e. an atmosphere partially covered by clouds) we follow the approach (referred to hereafter as the stream method) of dividing the atmosphere into a number of homogeneous columns (Amorati and Rizzi 2002). Each column is characterized by a different number of cloudy layers, hence different radiative properties, and contributes to a fraction of the overcast radiance that depends on the cloud overlapping assumption. To describe the stream method we give here an example where seven atmospheric layers are considered. Once the cloud fractional cover in each layer is known (*CFR* in Figure 9), we compute the cumulative cloud coverage, $N_{tot}(j)$, from layer 1 to layer j using the maximum-random overlap assumption . For a slab extending from layer 1 to layer j, the total cloud cover is written as

$$N_{tot} = 1 - (1 - N_1) \prod_{i=2}^{j} \frac{1 - \max(N_{i-1}, N_i)}{1 - N_{i-1}} \quad (42)$$

A cloud (blue shaded region in Figure 9) is then placed in layer j that covers the range from $N_{tot}(j)$-$CFR(j)$ to $N_{tot}(j)$. To determine the number of columns, we consider all the cloud configurations that result in a totally overcast column. In our example we obtain five, n_c, columns and one clear column.

Once the top of the atmosphere radiance has been computed for each homogeneous column, the cloudy radiance is written as the sum of all the single column radiances weighted by the column fractional coverage

$$L^{cloudy} = \sum_{s=1}^{n_c} (X_{s+1} - X_s) L_s^{overcast} + L^{clear} (1 - X_{n_c+1}) \qquad (43)$$

Note that if a clear column is present, this will be given a weight equal to $(1 - X_{n_c+1})$.

3. Changes to the microwave scattering code for RTTOV-9

The microwave scattering code provided with RTTOV-8 has been updated and interfaced with the new RTTOV-9 code. As well as simply updating the code for compatibility with the core RTTOV-9 routines, the following minor improvements were made:

- Better handling of hydrometeor amounts smaller than the lowest bin in the Mie tables. Scattering parameters are now extrapolated to zero, rather than set directly to zero below the lowest bin.
- An additional `total ice' hydrometeor type was include in the Mie lookup tables for use at the Met Office, whose model considers all frozen hydrometeors as one variable. The original ECMWF implementation has separate snow and cloud ice water hydrometeors. The user can now choose one or other of these options, but not both at the same time. The total ice hydrometeor type has been tested by Doherty *et. al.* (2007).
- The user was previously required to specify some inputs on fixed, internal RTTOV levels, and others on their own model levels. With the availability of an internal interpolation in the core RTTOV-9 code, all profile inputs are now made on user levels, considerably simplifying the interface.
- K matrix code functionality has been made part of the adjoint routines. This makes for greater efficiency and easier code maintenance, as duplication of code is a prime source of errors.
- The microwave scattering module was updated to be compatible with the linear-in-tau approximation used in the rest of the RTTOV code. Note that the cloudy/rainy-sky source functions in RTTOV-SCATT have always been based on the linear-in-tau approximation, so no changes were needed there. However, if hydrometeor amounts are smaller than a particular threshold, a clear sky source function is used instead. This clear sky source function needed to be changed to use the linear-in-tau approximation. The change is significant because many model levels can be unaffected by cloud or rain even when it is cloudy or raining at other levels.

The impact of these changes on the RTTOV_SCATT calculations is demonstrated in section 4.5.

4. Testing and Validation of RTTOV-9

To ensure no bugs have entered in the RTTOV code during the introduction of the above changes an extensive set of tests were applied to the new model before it was released to users. For example the use of the RTTOV-7 optical depth predictors should give identical results with the new code to the old RTTOV-7 code. The new RTTOV-9 optical depth predictors for high resolution sounders will give different radiances and are validated as described below. The new RTTOV-9 code is validated in several ways:

- The RTTOV-9 top of atmosphere radiances computed using either the old and new optical depth predictors are compared with those computed in the same way as in RTTOV but using the LbL model transmittances from a 117 ECMWF profile independent set (Chevallier, 2000). This tests the accuracy of the brightness temperatures simulated by RTTOV-9 but disregarding errors coming from the LbL model.
- The RTTOV-9 top of atmosphere radiances have been compared with observed IASI radiances using NWP analyses to provide the state vector and observed AIRS radiances for one tropical Pacific profile.
- The RTTOV-9 jacobians have been compared for IASI channels with those corresponding to RTTOV-7 and 8 predictors.
- The results of the new profile interpolation code is demonstrated.
- The effect of the modified path length computation on the IASI radiances is shown.
- Validation of the new treatment of cloud in RTTOV-9 is described in Annex A.
- Validation of the updated RTTOV_SCATT code.

There was also an extensive series of comparisons carried out, not described here, between RTTOV-8 and RTTOV-9 transmittances, radiances, jacobians and surface emissivities from the direct, TL, AD and K codes to check there are no differences during the code development except those anticipated. The tests conducted are in the RTTOV-9 test plan document and users can run these tests to verify the performance of the code on their platform.

Comparisons can be made with several different sets of profiles with pre-computed LbL transmittances. The dependent set of profiles and line-by-line transmittances from which the coefficients were computed can be used to check coherency. Also an independent set of profiles and transmittances can be used to check the model accuracy. The validation results described below are mainly for ATOVS, SEVIRI, AIRS and IASI but the performance of the model for all new instruments is checked in terms of transmittance differences from the LbL model and can be compared to similar channels in the above sensors.

4.1 Validation of top of atmosphere radiances

The primary output from RTTOV is the top of atmosphere radiance for each channel and so this is the main parameter for which the RTTOV-9 simulations are checked. The RTTOV-9 radiances are compared with radiances computed from the LbL model used to produce the dependent set transmittances and with radiances computed from other LbL models. In addition they are also compared with observations using co-incident NWP model or measured profiles as an input to RTTOV.

4.1.1 Comparison with independent datasets of line-by-line computed radiances

This comparison determines the accuracy of the regression scheme itself since the *same* LbL models were used to generate the RTTOV coefficients. For both the dependent set and independent profile sets brightness temperatures have been computed using the radiative transfer layer integration within RTTOV-9 to ensure any differences are only due to the LbL and fast model transmittances not the integration of the radiative transfer through the atmosphere. For the RTTOV-7 predictors no changes from RTTOV-7 to RTTOV-9 code were expected and so to verify this comparisons were made with the 117 independent profile set for ATOVS for the RTTOV-7, RTTOV-8 and RTTOV-9 codes with RTTOV-7 optical depth coefficients used in all versions of RTTOV.

Figure 10 documents the comparison between the RTTOV-9 fast model and line-by-line model brightness temperatures for the 117 independent profile set for NOAA-15 ATOVS over five zenith angles in the range 0-60 deg. In this case the line-by-line models were GENLN2 for the infrared and Liebe for the microwave. The figures shows the bias and standard deviations of the RTTOV-LbL differences are very similar for all 3 versions of RTTOV as expected giving confidence that the recoding has not introduced any errors. The mean biases for the three versions of the model are all less than 0.2K shown in Figure 10A.

Equivalent plots for the Meteosat-8 SEVIRI channels are given in Figures 11. Note that in contrast to the ATOVS plots these are for 6 zenith angles out to 63.6 deg as these geostationary imager radiances can measure at angles beyond 70 deg towards the edge of the Earth's disk as seen from geostationary orbit. Also shown in Figure 11 is the effect of using the Planck weighted coefficients which are now recommended for SEVIRI to reduce the biases seen in the 3.9μm channel when RTTOV simulations are compared with observed radiances.

For the accuracy of radiances from other sensors results from similar channels on sensors documented above can be used. For example for AVHRR and other geostationary imagers one can use the SEVIRI values as a guide for the equivalent channels. Also the extended set of results in R7REP2002 can also be used as being representative for the RTTOV-9 model with the RTTOV-7 predictors invoked.

For the new set of RTTOV-9 predictors defined in Tables 1 to 4 a set of LBLRTM line-by-line transmittances for the new 82 diverse ECMWF model profiles on 101 levels were computed as the new dependent set to compute the coefficients from. In addition the old 43 TIGR diverse profile set was used to compute an independent set of transmittances with LBLRTM. Figures 12

and 13 demonstrate the performance of the new RTTOV-9 optical depth predictions for IASI and AIRS respectively by comparing with the independent dataset of LBLRTM transmittances. The variable gases were water vapour, ozone, carbon dioxide, carbon monoxide, methane and nitrous oxide as variable gases. This can be compared with Figure 6 of R8REP2008 which shows the performance for AIRS channels with RTTOV-8 predictors. In addition Figures 14 and 15 give histograms of the distribution of the rms errors for IASI and AIRS.

The more rigorous calculation of the atmospheric path length in RTTOV-9, as described in section 2.4, leads to some differences in the computed top of atmosphere radiances compared with RTTOV-8. The maximum and minimum value of the difference between RTTOV-9 radiances using a constant zenith angle with height and a variable zenith angle is shown in Figure 16. Matricardi (2003) also plots the rms difference. These results are valid for a 90 level atmosphere for the 43 level case the differences would be larger.

As described in section 2.6.3 the line-by-line model for the microwave transmittances has been updated to include a revised half width for the 22GHz water vapour line and ozone absorption at 183GHz. Figure 17a and 17b illustrates the differences for AMSU and SSM/I brightness temperatures between the old and modified models for a set of 117 diverse profiles. For AMSU-A channel 1 the change in brightness temperature is up to +1K for high total column water amounts. For SSM/I channel 3 the effect is larger being up to almost +3K. Figure 17c also shows the effect of ozone on the AMSU-B channel 3 (also MHS channel 3) which is typically -0.2K.

4.1.2 Comparison with other radiative transfer model computed radiances

The results described above in section 4.1.1 all compare the radiances with radiances computed using the same LbL model from which the RTTOV coefficients were generated. Hence errors in the LbL models themselves (i.e. LBLRTM/MPM) are not included in the above estimates. In Saunders *et. al*. (2007) several infrared models (both fast and LbL) were used to compare with RTTOV simulations and although this comparison was only done with RTTOV-7 and RTTOV-8 the results are still valid for RTTOV-9 when using the RTTOV-7 or RTTOV-8 optical depth predictors.

In the microwave region there are less independent LbL models to compare with. The most comprehensive comparison which included RTTOV-6 simulations was the Garand *et. al.* (2001) intercomparison. RTTOV-9 is based on the same basic LbL model as RTTOV-6 so the results from Garand *et. al.* (2001) can still be applied to RTTOV-9 except for the differences noted above in 4.1.1.

4.1.3 Comparison with observations

A comparison of the simulated AIRS radiances with measured AIRS radiances over the tropical Pacific ARM site was presented in Saunders et. al. (2007) in their Figure 5. These results have been extended for this report to include RTTOV-9 predictors and the new LBLRTM generated coefficients as described by Matricardi (2008) and are shown for RTTOV-7, 8 and 9 in Figure 18. RTTOV-7 is based on GENLN2 derived coefficients from HITRAN-96, RTTOV-8 is based on kCARTA with HITRAN-2004 and separate water vapour line and continuum derived coefficients

and RTTOV-9 is based on LBLRTM with HITRAN-2004/2006 and GEISA-2003 depending on the spectral region and gas. Each version of the model used different optical predictors. The results mainly show improvements in the underlying spectroscopic databases used, with RTTOV-9 having fewer outliers and lower biases than RTTOV-7 and to a lesser extent RTTOV-8. Similar results are seen for IASI.

Another validation of the simulated radiances is to compare with real observations together with simulations from an NWP model. Figure 19 shows the statistics for 15 days in April 2008 of IASI radiances simulated from the ECMWF T799 IFS model using RTTOV-9 predictors and GENLN2 or LBLRTM generated coefficients with the corresponding IASI measurements separated into different latitude bands and night (Fig. 19a) and day (Fig. 19b). The model represents water vapour and ozone as dynamically varying constituents and carbon dioxide, methane, nitrous oxide and carbon monoxide fixed to their respective climatological values. The IASI observations show the ozone is not perfectly represented in the model. The differences between the GENLN2 based simulations and the LBLRTM simulations are small relative to the difference between observations and simulations but overall the LBLRTM simulations give a closer fit to the model especially around 1600 cm^{-1} in the middle of the water vapour rotation band. The biases introduced by non-LTE and solar reflection can be seen in the daytime observations (Fig. 19b) at frequencies beyond 2400cm^{-1} especially in the Tropics and N. Hemisphere at this time. It must be emphasised that the biases in Figure 19 are not only a function of RTTOV but also the accuracy of the model fields but nevertheless they demonstrate the agreement with observations where the NWP model is known to be trustworthy is encouraging.

4.2 Validation of jacobians

The accuracy of the jacobians computed by RTTOV are important to document for the radiance assimilation users as they are instrumental in modifying the NWP model analysis variables. This section describes a comparison of the jacobians for IASI channels generated by RTTOV-7, RTTOV-8 and RTTOV-9 predictors.

A diverse profile dataset was used to compute for a few IASI channels the nadir view jacobians for temperature, water vapour and ozone. Computations were made by RTTOV-7, RTTOV-8 and RTTOV-9 coefficients. The prescribed temperature perturbation was +1K, and for water vapour and ozone it was -1% of the layer mean concentration. Note that the RTTOV-7 values were computed on the standard 43 pressure levels and then transformed to 101 levels using the adjoint of the interpolation routine to enable comparisons to be made.

Figure 20 shows a temperature Jacobian for IASI channel 262 (710.25cm^{-1}). The RTTOV-7 Jacobian still has some traces of the interpolation from 43L to 101L but the RTTOV-8 predictors with kCARTA and the RTTOV-9 predictors with LBLRTM give perfectly smooth Jacobians. Users should note the initial RTTOV-9 IASI coefficient file released using GENLN2 gives a large spike in the Jacobian at 820hPa. This coefficient file, originally on the RTTOV-9 web site, should no longer be used and has been replaced by a LBLRTM coefficient file which gives the smoother Jacobians seen in Figure 20.

The water vapour Jacobian for IASI channel 3129 (1427cm^{-1}) is also shown in Figure 20. All 3 versions of the predictors with different line-by-line models give very similar Jacobians with small differences in the stratosphere as can be seen in the Figure. The ozone Jacobians for RTTOV-7, 8 and 9 are also very similar (not shown) at least for a IASI channel with strong ozone absorption.

4.3 Infrared cloudy radiance simulations

A comprehensive validation of the RTTOV-9 cloudy simulations was carried out by Embury and Merchant and their report is attached as Annex-A. They used the DISORT full scattering model to compare with the corresponding parameters computed in RTTOV-9 for water clouds. The main conclusions from their study were:

- RTTOV-9 is a significant improvement on RTTOV-8 for simulating cloudy radiances when compared to DISORT run with equivalent optical properties. This is particularly true for thermal infrared wavelengths, where biases seen in RTTOV-8 are almost removed. This improvement is partly due to the fact that, with RTTOV-9, all calculations are performed on a consistent set of 100 levels. Nonetheless, scattering is significant at thermal wavelengths and the very low biases indicate that the parameterisation of scattering is effective.
- At near-infrared wavelengths, biases are significantly improved up to cloud optical depths of about 10. At greater optical depths, the biases found relative to DISORT were similar in magnitude to those with RTTOV-8, but are, perhaps, rather more consistent between clouds.
- A pattern of over-estimation of radiance for warm clouds and under-estimation for cold clouds is evident, which fits with the method of parameterisation of scattering, in which the absorption optical depth (and thus the thermal emission) is scaled independently of incident radiance.

The reader is referred to Annex-A for more details of the results from this study.

4.4 Validation of new profile interpolation

The new profile interpolation code described in section 2.7 was tested both for the forward model and the Jacobians. For the forward model interpolations the profile differences between a nearest neighbour approach and the piecewise weighted integration adopted in RTTOV-9 are small and not shown. For the Jacobians however going from 43 levels inside RTTOV to 100 levels for the user the differences can be significant as illustrated in Figure 21 where the no interpolation case is compared with the interpolated Jacobians using either method. It is clear the nearest neighbour approach introduces large spikes in the temperature Jacobian due to the "hidden layers" whereas the effect is much reduced for the weighted interpolation of Rochon *et. al*. (2007) referred to as *intavg*. Figure 22 confirms that the effect is not present when going from fewer levels in the user profile to more levels inside RTTOV. Finally Figure 23, like Figure 21, shows the differences for a HIRS water vapour channel. The spikes introduced into the Jacobians by the nearest neighbour interpolation are very damaging to data assimilation and physical retrieval schemes.

4.5 Validation of microwave scattering code

The majority of code changes for RTTOV-9 had no effect on output cloudy/rainy microwave brightness temperatures. The only two that did have a significant effect were (i) changing to the linear in tau approximation described in section 2.5 and (ii) using the internal RTTOV profile interpolation. The latter was implemented so as to produce results as close as possible to the previous version of RTTOV.

All scientific validation was done in the ECMWF IFS system, within the context of the 1D+4D-Var assimilation of rain and cloud-affected SSM/I radiances (Bauer et al. 2006a,b). The results shown here are based on the 1D-Var retrievals of total column water vapour, TCWV, from SSM/I observations using a first guess model with T159 resolution and 60 vertical levels, which is smaller than that used operationally, but is perfectly suitable for this kind of validation. A single 12 hour time window was considered, 00UTC on 1st August 2007, giving approximately 5800 SSM/I observations co-located with a model grid point and passing initial screening tests. No observation was considered over land, over sea ice, or at latitudes greater than 60 degrees. Globally, even a 12 hour period contains a reasonably representative sample of the different meteorological conditions encountered in the 1D+4D-Var assimilation at ECMWF.

Four experiments were considered. Experiment CTRL was a control run based on cycle 32r3 of the ECMWF system, which uses RTTOV-8. Experiment A1 used RTTOV-9 and included all RTTOV-SCATT upgrades except for the use of the internal interpolation and the change to a linear-in-tau clear sky source function. This experiment was expected to demonstrate essentially no change in simulated brightness temperatures. Experiment A2 included additionally the use of internal interpolation. This meant that the clear sky brightness temperatures and transmittances were now being generated on the 60 model levels rather than the 43 fixed RTTOV levels. Experiment A3 is as experiment A2 but additionally using linear-in-tau source functions in both the core clear-sky RTTOV routines, and in the microwave scattering code when hydrometeor amounts are very small. Experiment A3 is the configuration that was distributed in RTTOV-9.

It should be noted that there is one difference compared to the distributed versions of RTTOV-8 and RTTOV-9 that is common to all four of the experiments: one term of the sea surface emissivity parameterisation has been disabled. This was done for compatibility with the current ECMWF system, and though it results in systematic changes in the surface emissivity resulting in clear sky brightness temperature changes of 4K, these changes are globally very uniform, and will not significantly affect the results of the comparison between experiment and control.

First guess brightness temperatures were calculated at all 5800 SSM/I observation points, whether clear, cloudy or rainy. Differences between experiments A1 and CTRL were negligible, as expected. For channel 19v of SSM/I, no first guess changed more than 0.03K and 99% of first guesses changed by less than 0.005K (figure not shown). Figure 24 examines histograms of the difference between experiments A2, A3 and CTRL for channel 19v of SSM/I. Results in other channels are similar. Panel (a) shows the changes to clear-sky column brightness temperatures, i.e. those generated by the core RTTOV routines ignoring cloud and precipitation. Internal interpolation and the linear-in-tau approximation both generally reduce simulated brightness

temperatures. Their combined effect (the red histogram) is a reduction of order 0.2K. Panel (b) shows the changes to the total brightness temperature. i.e. now including the effects of cloud and rain where appropriate. These changes are very similar to those seen when considering only clear-sky radiative transfer, suggesting that they mainly come from the effects of the linear-in-tau approximation and internal interpolation on the core RTTOV routines. Overall, RTTOV-9 results in reductions of around 0.1 to 0.2K in simulated brightness temperature. There is no significant improvement or degradation in the fit of first guess to SSM/I observations (statistics not shown).

A further test of the impact of the changes was to look at the 1D-Var retrievals. However, these retrievals were not significantly affected either. Figure 25 compares TCWV retrieval increments between experiment A3 and control. The sample shown contains the 1165 observations which generated successful retrievals in both experiments. Separately, there were 1213 successful retrievals in CTRL and 1266 in experiment A3, but the increase is unlikely to be significant, and is probably linked to the small mean changes in first guess brightness temperatures. The reason that only roughly 20% of observations result in successful retrievals is first, that clear-sky observations are discarded, and second, that a number of very stringent quality control checks are made. The figure shows that changes to the retrieval were small. The main effect was a slight increase in retrieved TWCV of order of 0.1 kg m^{-2}, shown in Figure 25, which is consistent with the decrease in first guess brightness temperatures.

In summary, the majority of upgrades had no scientific impact, but some impact was unavoidable from the changes to (i) linear-in-tau source functions in clear-sky, and (ii) using model levels rather than RTTOV levels. However, this impact was small, resulting in typically a 0.1 to 0.2K reduction in simulated SSM/I channel 19v brightness temperatures, common to clear, cloudy and precipitating skies.

5. Summary and Future Developments

The latest version of RTTOV, RTTOV-9 has been validated in several ways to show the same or improved performance for the prediction of satellite top of atmosphere radiances both for clear air, cloudy and precipitating profiles. It builds on previous versions of RTTOV. The main improvements have been:

- Parameterised aerosol scattering for a range of user aerosol components
- New cloud and aerosol parameterised scattering for infrared sensors inside RTTOV
- Linear in optical depth approximation for the Planck function to improve the accuracy of the radiance computation
- Include reflected solar radiation for wavelengths below 5 microns.
- Now six variable gas profiles can be supplied to RTTOV (H_2O, O_3, CO_2, + N_2O, CO, CH_4)
- Further optimisation of optical depth computations for all gases for high resolution IR sensors (RTTOV-9 predictors)
- An altitude dependent variation of local zenith angle and optionally allow for atmospheric refraction

- The input profile levels can be defined by user and the radiances and transmittances output are on the same levels allowing better mapping of computed jacobians on to user levels than for previous versions of RTTOV.

Plans are now underway to develop RTTOV-10 with several new features which will include the zeeman effect for high peaking microwave channels, better treatment of the input profile at the top, improvement of microwave emissivity at low frequencies for land and ocean and addition of non-LTE effects for shortwave infrared channels.

6. Acknowledgements

The RTTOV-9 developments and validation described here were carried out as part of the EUMETSAT funded NWP-SAF activities by the Met Office, ECMWF and MétéoFrance. The University of Edinburgh provided the results for the validation of the new RTTOV-9 cloudy radiance simulations. Tom Blackmore provided the plots in Figure 10.

7. References

Amorati, R., and Rizzi, R., 2002: Radiances simulated in presence of clouds by use of a fast radiative transfer model and a multiple-scattering scheme. *Applied Optics*, **41**, *No. 9, 1604-1614*.

Baran, A.J., Francis, P.N., Labonnote, L.C., and Doutriaux-Boucher, M., 2001: A scattering phase function for ice cloud: tests of applicability using aircraft and satellite multi-angle multi-wavelength radiance measurements of cirrus. *Q. J. R. Meteorol. Soc*., **127**, *2395-2416*.

Baran, A.J., 2003: Simulation of infrared scattering from ice aggregates by use of a size-shape distribution of circular ice cylinders. *Applied Optics*, **42**, *No.15, 2811-2818*.

Baran, A.J. & Francis, P.N., 2004: On the radiative properties of cirrus cloud at solar and thermal wavelengths: A test of model consistency using high resolution airborne radiance measurements. *Q. J. Roy. Meteorol. Soc.* **130** *763-778.*

Bauer, P., P. Lopez, A. Benedetti, D. Salmond, and E. Moreau, 2006a: Implementation of 1D+4D-Var assimilation of precipitation-affected microwave radiances at ECMWF. I: 1D-Var. *Q. J. Roy. Meteorol. Soc.,* **132***, 2277-2306.*

Bauer, P., P. Lopez, D. Salmond, A. Benedetti, S. Saarinen and E. Moreau, 2006b: Implementation of 1D+4D-Var assimilation of precipitation-affected microwave radiances at ECMWF. II: 4D-Var. *Q. J. Roy. Meteorol. Soc.,* **132***, 2307-2332*.

Boudala, F.S., Isaac, G.A., Fu, Q. & Cober, S.G., 2002: Parameterization of effective ice particle size for high-latitude clouds. *Int. J. Climatol.,* **22,** *1267-1284*.

Chevallier, F. 2000 TIGR-like sampled databases of atmospheric profiles from the ECMWF 50 level forecast model. NWP-SAF report 1. *NWP SAF Report available from*
http://www.ecmwf.int/publications/library/do/references/list/202

Chevallier, F., S. Di Michele and A.P. McNally 2006: Diverse profile datasets from the ECMWF 91-level short range forecasts. *NWPSAF-EC-TR-010.* *http://www.metoffice.com/research/interproj/nwpsaf/rtm/profiles_91L.pdf*

Chou, M.-D., Lee, K.-T., Tsay, S.-C., and Fu, Q., 1999: Parameterization for Cloud Longwave scattering for use in Atmospheric Models. *Journal of Climate*, **12**, *159-169.*

Doherty, A.M. and T. R. Sreerekha and U. M. O'Keeffe and S. J. English, 2007: Ice hydrometeor microphysical assumptions in radiative transfer models at AMSU-B frequencies, *Quart. J. Roy. Meteorol. Soc.,* **133***, 1205-1212.*

Draine, B., T., and Flatau, P., J., 1994: Discrete-dipole approximation for scattering calculations. *J. Opt. Soc. Am. A. Opt. Image Sci.*, **11**, *1491-1499.*

Eyre J.R. and H.M. Woolf 1988: Transmittance of atmospheric gases in the microwave region: a fast model. *Applied Optics* **27** *3244-3249*

Eyre J.R. 1991: A fast radiative transfer model for satellite sounding systems. *ECMWF Research Dept. Tech. Memo.* **176** Available at http://www.ecmwf.int/publications/library/ecpublications/_pdf/tm/001-300/tm176.pdf

Fu, Q., 1996: An accurate parameterization of the solar radiative properties of cirrus clouds., *J. Clim.,* **9,** *2058-2082.*

Gosse, S., Labrie, D., and Chylek, P., 1995: Refractive index of ice in the 1.4-7.8 μm spectral range. *Appl. Opt.,* **34**, *6582-6586.*

Hasselman, K., Barnet, T.P., Bouws, E., Carlson, H., Cartwright, D.E., Enke, K., Ewing, J.A., Gienapp, H., Hasselman, P., Kruseman, P., Meerburg, A., Muller, P., Olbers, D.J., Richter, K., Sell, W., and Walden, H., 1973, Measurements of Wind Wave Growth and Swell Decay during the Joint North Sea Wave Project (JONSWAP) *Report from Deutsches Hydrographisches Institut, Hamburg, Germany.*

Hess, M., Koepke, P., and Schult, I., 1998: Optical Properties of Aerosols and Clouds: the software package OPAC. *Bull. American. Meteorol. Soc.,* **79**, *831-844.*

John, V. O. and S. A. Buehler, 2004: The impact of ozone lines on AMSU-B radiances, *Geophys. Res. Lett.*, **31**, *L2 1108*

Kobayashi S., M. Matricardi , D. Dee and S. Uppala. 2008: Use of SSU and AMSU-A observations in reanalyses. *Extended abstract in 3rd WCRP International Conference on Reanalysis Tokyo 28 Jan – 1 Feb 2008. See http://wcrp.ipsl.jussieu.fr/Workshops/Reanalysis2008/abstract.html*

Kurucz, R.L., 1992: Synthetic infrared spectra, in *Infrared Solar Physics, IAU Symposium 154, edited by D.M. Rabin and J.T. Jefferies, Kluwer, Acad., Norwell, MA.*

Liebe, H. J. 1989: MPM, an atmospheric millimeter wave propagation model. *Int. J. Infrared and Millimeter Waves*, **10**, *631-650.*

Liebe H.J., G.A. Hufford and M.G. Cotton . 1993: Propagation modeling of moist air and suspended water/ice particles at frequencies below 1000 GHz. *AGARD 52nd Specialists' Meeting of the Electromagnetic Wave Propagation Panel, Palma de Mallorca, Spain 17-21 May 1993.*

Liljegren, J. C., S. A Boukabara, K. Cady-Pereira, S. A Clough, 2005: The effect of the half-width of the 22-GHz water vapor line on retrievals of temperature and water vapor profiles with a twelve-channel microwave radiometer. *IEEE Trans. Geosci. and Remote Sensing*, **43**, *1102-1108.*

Macke, A., Mueller, J., and Raschke, E., 1996: Single scattering properties of Atmospheric Ice Crystals. *Journal of the Atmospheri Sciences*, **53**, *No.19, 2813-2825.*

Matricardi, M and Saunders, R.W. 1999: A fast radiative transfer model for simulation of IASI radiances. *Applied Optics,* **38***, 5679-5691*.

Matricardi, M. 2003: RTIASI-4 A new version of the ECMWF fast radiative transfer model for the infrared atmospheric sounding interferometer. *ECMWF Research Dept. Tech. Memo.* **425**. **474** (available at: http:/www.ecmwf.int/publications/library/references/list/14)

Matricardi, M., Chevallier F, Kelly G, Thepaut J-N 2004: An improved general fast radiative transfer model for the assimilation of radiance observations. *Q. J. Roy. Meteorol. Soc.* **130** *153-173*

Matricardi, M., 2005: The inclusion of aerosols and clouds in RTIASI, the ECMWF fast radiative transfer model for the Infrared Atmospheric Sounding Interferometer. *ECMWF Technical Memorandum* **474** (available at: http:/www.ecmwf.int/publications/library/references/list/14)

Matricardi, M. 2008: The generation of RTTOV regression coefficients for IASI and AIRS using a new profile training set and a new line-by-line database. *ECMWF Research Dept. Tech. Memo.* **564.**
(available at: http://www.ecmwf.int/publications/library/do/references/list/14)

Matricardi, M. and A. McNally 2008: An assessment of the accuracy of the RTTOV fast radiative transfer model using IASI data. *Proceedings of ITSC-16, Angra dos Reis, Brazil 7-13 May 2008.*

McFarquhar, G.M., Iacobellis, S. & Somerville, R.C.J., 2003: SCM simulations of tropical ice clouds using observationally based parameterizations of microphysics. *J. Clim.,* **16,** *1643-1664*.

Mishchenko, M. I., 1991: Light scattering by randomly oriented axially symmetric particles. *Appl. Opt*., **32**, *871-882.*

Mishchenko, M. I., and Macke, A., 1998: Incorporation of physical optics effects and computation of the Legendre expansion for ray-tracing phase functions involving δ-function transmission. *J. of Geophys. Res.,* **103**, *1799-1805.*

Nussenzveig, H. M., and Wiscombe, W.J., 1980: Efficiency factors in Mie scattering, *Phys. Rev. Lett.*, **45**, *1490-1493*.

Ou S.-C. and K.-N. Liou 1995: Ice microphysics and climatic temperature feedback. *Atmos. Res.* **35** *127-138.*

Rayer P.J. 1995: Fast transmittance model for satellite sounding. *Applied Optics,* **34** *7387-7394*.

Rizzi, R. and M. Matricardi 1998: The use of TOVS clear radiances for numerical weather prediction using an updated forward model.*, Q. J. Roy. Meteorol. Soc.* **124** *1293-1312*

Rochon, Y.J., L. Garand, D.S. Turner, and S. Polavarapu, 2007: Jacobian mapping between vertical coordinate systems in data assimilation, *Q. J. Roy. Meteorol. Soc*. **133** *1547-1558*.

R7REP2002 RTTOV-7 science and validation report available at:
http://www.metoffice.gov.uk/research/interproj/nwpsaf/rtm/rtm_rttov7.html

R8REP2006 RTTOV-8 science and validation report available at:
http://www.metoffice.gov.uk/research/interproj/nwpsaf/rtm/rtm_rttov8.html

Saunders R.W., M. Matricardi and P. Brunel 1999a: A fast radiative transfer model for assimilation of satellite radiance observations - RTTOV-5. *ECMWF Research Dept. Tech. Memo.* **282** *(available from http://www.ecmwf.int/publications/library/do/references/list/14).*

Saunders R.W., M. Matricardi and P. Brunel 1999b: An Improved Fast Radiative Transfer Model for Assimilation of Satellite Radiance Observations. *Q. J. Roy. Meteorol. Soc. ,* **125,** *1407-1425*.

Strow, L.L., H.E. Motteler, R.G. Benson, S.E. Hannon, and S. De Souza-Machado. 1998: Fast computation of monochromatic infrared atmospheric transmittances using compressed look-up tables. *J. Quant. Spectrosc. Rad. Trans.,* **59**, *481-493*.

Takano, Y., and Liou, K., N., 1989: Solar radiative transfer in cirrus clouds. I. Single scattering optical properties of hexagonal ice crystals. *J. Atmos. Sci*., **46**, *20-36.*

Van de Hulst, H.C., 1981: *Light* Scattering by Small Particles. *Dover Publications, New York.*

Warren, S.G., 1984: Optical constants of ice from ultraviolet to the microwave. *Appl. Opt*., **23**, *1206-1225.*

Wyser, K., 1998: The effective radius in cirrus clouds. *J. Clim.,* **11,** *1793-1802*.

Yang, P., and Liou, K., N., 1996: Finite-difference time domain method for light scattering by small ice crystals in three-dimensional space. *J. Opt. Soc. Am*., **13**, *2072-2085*.

Yang, P., and Liou, K., N., 1998: Single-scattering properties of complex ice crystals in terrestrial atmosphere. *Contrib. Atmos. Phys.*, **71**, *291-304*.

Yang, P., Liou, K., N., Wyser, K., and Mitchell, D., 2000: Parameterization of the scattering and absorption properties of individual ice crystals. *J. Geophys. Res.*, **105**, *4699-4718*.

Predictor	Fixed Gases
$X_{j,1}$	$\sec(\theta)$
$X_{j,2}$	$\sec^2(\theta)$
$X_{j,3}$	$\sec(\theta)T_r(j)$
$X_{j,4}$	$\sec(\theta)T_r^2(j)$
$X_{j,5}$	$T_r(j)$
$X_{j,6}$	$T_r^2(j)$
$X_{j,7}$	$\sec(\theta)T_{fw}(j)$
$X_{j,8}$	$\sec(\theta)T_{fu}(j)$

Table 1. RTTOV-9 predictors used for fixed gases. See Table 4 for definition of terms.

Predictor	H_2O	CO_2	O_3
$X_{j,1}$	$(\sec(\theta)W_r(j))^2$	$\sec(\theta)CO2_r(j)$	$\sec(\theta)O_r(j)$
$X_{j,2}$	$\sec(\theta)W_w(j)$	$T_r^2(j)$	$\sqrt{\sec(\theta)O_r(j)}$
$X_{j,3}$	$(\sec(\theta)W_w(j))^2$	$\sec(\theta)T_r(j)$	$\sec(\theta)O_r(j)\delta T(j)$
$X_{j,4}$	$\sec(\theta)W_r(j)\delta T(j)$	$\sec(\theta)T_r^2(j)$	$(\sec(\theta)O_r(j))^2$
$X_{j,5}$	$\sqrt{\sec(\theta)W_r(j)}$	$T_r(j)$	$\sqrt{\sec(\theta)O_r(j)}\,\delta T(j)$
$X_{j,6}$	$\sqrt[4]{\sec(\theta)W_r(j)}$	$\sec(\theta)$	$\sec(\theta)O_r^2(j)O_w(j)$
$X_{j,7}$	$\sec(\theta)W_r(j)$	$\sec(\theta)T_w(j)$	$\frac{O_r(j)}{O_w(j)}\sqrt{\sec(\theta O_r(j)}$
$X_{j,8}$	$(\sec(\theta)W_r(j))^3$	$(\sec(\theta)CO2_w(j))^2$	$\sec(\theta)O_r(j)O_w(j)$
$X_{j,9}$	$(\sec(\theta)W_r(j))^4$	T_w^3	$O_r(j)\sec(\theta)\sqrt{O_w(j)\sec(\theta)}$
$X_{j,10}$	$\sec(\theta)W_r(j)\delta T(j)\lvert\delta T(j)\rvert$	0	$\sec(\theta)O_w(j)$
$X_{j,11}$	$(\sqrt{\sec(\theta)W_r(j)})\delta T(j)$	0	$(\sec(\theta)O_w(j))^2$
$X_{j,12}$	$\frac{\sec(\theta)W_r^2(j)}{W_{tw}(j)}$	0	0
$X_{j,13}$	$\frac{\sqrt{\sec(\theta)W_r(j)}W_r(j)}{W_{tw}(j)}$	0	0

For frequencies [1095.25 to 1750cm^{-1}] **For frequencies [1995 to 2295cm^{-1}]**

$X_{j,14}$	$\sec(\theta)CH4_r(j)$	$X_{j,10}$	$\sec(\theta)CO_r(j)$
$X_{j,15}$	$(\sec(\theta)CH4_r(j))^2\,\delta T$	$X_{j,11}$	$\sec(\theta)T_w(j)\sqrt{T_r(j)}$

For frequencies [1900.25 to 1994.75cm^{-1}] **For frequencies [2295.25 to 2660cm^{-1}]**

$X_{j,14}$	$\sec(\theta)CO2_r(j)$	$X_{j,10}$	$\sec(\theta)T_w(j)\sqrt{T_r(j)}$

For frequencies [1995 to 2295cm^{-1}] **For frequencies [690.5 to 1100 cm^{-1}]**

$X_{j,14}$	$\sec(\theta)CO2_r(j)$	$X_{j,3}$	$\sec^2(\theta)T_r(j)$	$X_{j,4}$	$(\sec(\theta)T_r\,j))^2$
$X_{j,15}$	$\sec(\theta)CO_r(j)$	$X_{j,6}$	$\sec(\theta)^2$	$X_{j,7}$	$(\sec(\theta)T_w(j))^2$

Table 2. RTTOV-9 predictors used for H_2O, CO_2 and O_3. See Table 4 for definition of terms.

Predictor	CO	N_2O	CH_4
$X_{j,1}$	$\sec(\theta)\, CO_r(j)$	$\sec(\theta)\, N2O_r(j)$	$\sec(\theta)\, CH4_r(j)$
$X_{j,2}$	$\sqrt{\sec(\theta)\, CO_r(j)}$	$\sqrt{\sec(\theta)\, N2O_r(j)}$	$\sqrt{\sec(\theta)\, CH4_r(j)}$
$X_{j,3}$	$\sec(\theta)\, CO_r(j)\, \delta T(j)$	$\sec(\theta)\, N2O_r(j)\, \delta T(j)$	$\sec(\theta)\, CH4_r(j)\, \delta T(j)$
$X_{j,4}$	$(\sec(\theta)\, CO_r(j))^2$	$(\sec(\theta)\, N2O_r(j))^2$	$(\sec(\theta)\, CH4_r(j))^2$
$X_{j,5}$	$\sqrt{\sec(\theta)\, CO_r(j)}\, \delta T(j)$	$N2O_r(j)\, \delta T(j)$	$CH4_r(j)\, \delta T(j)$
$X_{j,6}$	$\sqrt[4]{\sec(\theta)\, CO_r(j)}$	$\sqrt[4]{\sec(\theta)\, N2O_r(j)}$	$\sqrt[4]{\sec(\theta)\, CH4_r(j)}$
$X_{j,7}$	$\sec(\theta)\, CO_r(j)\, \delta T(j) \lvert \delta T(j) \rvert$	$\sec(\theta)\, N2O_w(j)$	$\sec(\theta)\, CH4_{tw}(j)$
$X_{j,8}$	$\dfrac{\sec(\theta)\, CO_r^2(j)}{CO_w(j)}$	$\sec(\theta)\, N2O_{tw}(j)$	$CH4_{tw}(j)$
$X_{j,9}$	$\dfrac{\sqrt{\sec(\theta)\, CO_r(j)}\, CO_r(j)}{CO_w(j)}$	$N2O_{tw}(j)$	$(\sec(\theta)\, CH4_w(j))^2$
$X_{j,10}$	$\dfrac{\sec(\theta)\, CO_r^2(j)}{\sqrt{CO_w(j)}}$	$\dfrac{\sqrt{\sec(\theta)\, N2O_r(j)}\, N2O_r(j)}{N2O_w(j)}$	$\sec(\theta)\, CH4_w(j)$
$X_{j,11}$	$\dfrac{\sec(\theta)\, CO_r^2(j)}{\sqrt[4]{CO_w(j)}}$	0	$\dfrac{\sqrt{\sec(\theta)\, CH4_r(j)}\, CH4_r(j)}{CH4_w(j)}$

For frequencies [1050 to 1350cm^{-1}]

$X_{j,11}$	$\sec(\theta)\, CH4_r(j)$
$X_{j,12}$	$\sec(\theta)\, CH4_w(j)$

For frequencies [1995 to 2295cm^{-1}]

$X_{j,11}$	$\sec(\theta)\, CO_r(j)$
$X_{j,12}$	$\sec(\theta)^2\, CO_r(j)\, CO_w(j)$

Table 3. RTTOV-9 predictors used for CO, N_2O and CH_4. See Table 4 for definition of terms

$$T(l) = [T^{profile}(l+1) + T^{profile}(l)] / 2 \qquad T^*(l) = [T^{reference}(l+1) + T^{reference}(l)] / 2$$
$$W(l) = [W^{profile}(l+1) + W^{profile}(l)] / 2 \qquad W^*(l) = [W^{reference}(l+1) + W^{reference}(l)] / 2$$
$$O(l) = [O^{profile}(l+1) + O^{profile}(l)] / 2 \qquad O^*(l) = [O^{reference}(l+1) + O^{reference}(l)] / 2$$
$$CO(l) = [CO^{profile}(l+1) + CO^{profile}(l)] / 2 \qquad CO^*(l) = [CO^{reference}(l+1) + CO^{reference}(l)] / 2$$
$$CH_4(l) = [CH_4^{profile}(l+1) + CH_4^{profile}(l)] / 2 \qquad CH_4^*(l) = [CH_4^{reference}(l+1) + CH_4^{reference}(l)] / 2$$
$$N_2O(l) = [N_2O^{profile}(l+1) + N_2O^{profile}(l)] / 2 \qquad N_2O^*(l) = [N_2O^{reference}(l+1) + N_2O^{reference}(l)] / 2$$
$$CO_2(l) = [CO_2^{profile}(l+1) + CO_2^{profile}(l)] / 2 \qquad CO_2^*(l) = [CO_2^{reference}(l+1) + CO_2^{reference}(l)] / 2$$

$$T_r(l) = \frac{T(l)}{T^*(l)} \qquad \delta T(l) = T(l) - T^*(l) \qquad W_r(l) = \frac{W(l)}{W^*(l)} \qquad O_r(l) = \frac{O(l)}{O^*(l)}$$

$$CO_r(l) = \frac{CO(l)}{CO^*(l)} \qquad CH4_r(l) = \frac{CH_4(l)}{CH_4^*(l)} \qquad N2O_r(l) = \frac{N_2O(l)}{N_2O^*(l)} \qquad CO2_r(l) = \frac{CO_2(l)}{CO_2^*(l)}$$

$$T_w(l) = \{\sum_{i=1}^{l} P(i)[P(i) - P(i-1)]\, T(i)\} / \{\sum_{i=1}^{l} P(i)[P(i) - P(i-1)]\, T^*(i)\}$$
$$T_{fu}(l) = \{\sum_{i=1}^{l} T(i)\} / \{\sum_{i=1}^{l} T^*(i)\}$$
$$T_{fw}(l) = \{\sum_{i=2}^{l} T(i)\} / \{\sum_{i=2}^{l} T^*(i)\}$$
$$W_w(l) = \{\sum_{i=1}^{l} P(i)[P(i) - P(i-1)]\, W(i)\} / \{\sum_{i=1}^{l} P(i)[P(i) - P(i-1)]\, W^*(i)\}$$
$$W_{tw}(l) = \{\sum_{i=1}^{l} P(i)[P(i) - P(i-1)] T(i)\, W(i)\} / \{\sum_{i=1}^{l} P(i)[P(i) - P(i-1)] T^*(i)\, W^*(i)\}$$
$$O_w(l) = \{\sum_{i=1}^{l} P(i)[P(i) - P(i-1)]\, O(i)\} / \{\sum_{i=1}^{l} P(i)[P(i) - P(i-1)]\, O^*(j)\}$$
$$CO_w(l) = \{\sum_{i=1}^{l} P(i)[P(i) - P(i-1)]\, CO(i)\} / \{\sum_{i=1}^{l} P(i)[P(i) - P(i-1)]\, CO^*(j)\}$$
$$CO_{tw}(l) = \{\sum_{i=1}^{l} P(i)[P(i) - P(i-1)]\, T(j) CO(i)\} / \{\sum_{i=1}^{l} P(i)[P(i) - P(i-1)]\, T^*(j) CO^*(j)\}$$
$$CH4_w(l) = \{\sum_{i=1}^{l} P(i)[P(i) - P(i-1)]\, CH_4(i)\} / \{\sum_{i=1}^{l} P(i)[P(i) - P(i-1)]\, CH_4^*(j)\}$$
$$CH4_{tw}(l) = \{\sum_{i=1}^{l} P(i)[P(i) - P(i-1)] T(j)\, CH_4(i)\} / \{\sum_{i=1}^{l} P(i)[P(i) - P(i-1)]\, T^*(j) CH_4^*(j)\}$$
$$N2O_w(l) = \{\sum_{i=1}^{l} P(i)[P(i) - P(i-1)]\, N_2O(i)\} / \{\sum_{i=1}^{l} P(i)[P(i) - P(i-1)]\, N_2O^*(j)\}$$
$$N2O_{tw}(l) = \{\sum_{i=1}^{l} P(i)[P(i) - P(i-1)] T(j) N_2O(i)\} / \{\sum_{i=1}^{l} P(i)[P(i) - P(i-1)]\, T^*(j) N_2O^*(j)\}$$
$$CO2_w(l) = \{\sum_{i=1}^{l} P(i)[P(i) - P(i-1)]\, CO_2(i)\} / \{\sum_{i=1}^{l} P(i)[P(i) - P(i-1)]\, CO_2^*(j)\}$$

The $P(i)$'s are the values of the pressure at each level. $T^{profile}(l)$, $W^{profile}(l)$, $O^{profile}(l)$, $CO^{profile}(l)$, $CH_4^{profile}(l)$, $N_2O^{profile}(l)$ and $CO_2^{profile}(l)$ are the temperature and variable gases mixing ratio profiles. $T^{reference}(l)$, $W^{reference}(l)$, $O^{reference}(l)$, $CO^{reference}(l)$, $CH_4^{reference}(l)$, $N_2O^{reference}(l)$ and $CO_2^{reference}(l)$ are corresponding reference profiles. For these variables *l* refers to the *l*th level; otherwise *l* is the *l*th layer, i.e.the layer below the *l*th level (layers are numbered from 1 to 100). Note that we take $P(0) = 2P(1) - P(2)$ and $T_{fw}(1) = (P(2) - P(1))P(1)T(1) / T^*(1)$. Here θ is the zenith angle.

Table 4. Definition of profile variables used in predictors defined in tables 1, 2 and 3.

Interval 1 [645 to 850 cm^{-1}]

$$\hat{\Gamma}_{i,j}^{tot} = \hat{\Gamma}_{i,j}^{fix}\left(\frac{\hat{\Gamma}_{i,j}^{fix+CO_2}}{\hat{\Gamma}_{i,j}^{fix}}\right)\left(\frac{\hat{\Gamma}_{i,j}^{fix+H_2O+CO_2}}{\hat{\Gamma}_{i,j}^{fix+CO_2}}\right)\left(\frac{\hat{\Gamma}_{i,j}^{fix+H_2O+CO_2+O_3}}{\hat{\Gamma}_{i,j}^{fix+H_2O+CO_2}}\right)$$

Interval 2 [850.25 to 949.75 cm^{-1}]

$$\hat{\Gamma}_{i,j}^{tot} = \hat{\Gamma}_{i,j}^{fix}\left(\frac{\hat{\Gamma}_{i,j}^{fix+CO_2}}{\hat{\Gamma}_{i,j}^{fix}}\right)\left(\frac{\hat{\Gamma}_{i,j}^{fix+H_2O+CO_2}}{\hat{\Gamma}_{i,j}^{fix+CO_2}}\right)$$

Interval 3 [950 to 1100 cm^{-1}]

$$\hat{\Gamma}_{i,j}^{tot} = \hat{\Gamma}_{i,j}^{fix}\left(\frac{\hat{\Gamma}_{i,j}^{fix+CO_2}}{\hat{\Gamma}_{i,j}^{fix}}\right)\left(\frac{\hat{\Gamma}_{i,j}^{fix+H_2O+CO_2}}{\hat{\Gamma}_{i,j}^{fix+CO_2}}\right)\left(\frac{\hat{\Gamma}_{i,j}^{fix+H_2O+CO_2+O_3}}{\hat{\Gamma}_{i,j}^{fix+H_2O+CO_2}}\right)$$

Interval 4 [1100.25 to 1199.75 cm^{-1}]

$$\hat{\Gamma}_{i,j}^{tot} = \hat{\Gamma}_{i,j}^{fix}\left(\frac{\hat{\Gamma}_{i,j}^{fix+CH_4}}{\hat{\Gamma}_{i,j}^{fix}}\right)\left(\frac{\hat{\Gamma}_{i,j}^{fix+CH_4+N_2O}}{\hat{\Gamma}_{i,j}^{fix+CH_4}}\right)\left(\frac{\hat{\Gamma}_{i,j}^{fix+H_2O+CH_4+N_2O}}{\hat{\Gamma}_{i,j}^{fix+CH_4+N_2O}}\right)\left(\frac{\hat{\Gamma}_{i,j}^{fix+H_2O+CH_4+N_2O+O_3}}{\hat{\Gamma}_{i,j}^{fix+H_2O+CH_4+N_2O}}\right)$$

Interval 5 [1200 to 1250 cm^{-1}]

$$\hat{\Gamma}_{i,j}^{tot} = \hat{\Gamma}_{i,j}^{fix}\left(\frac{\hat{\Gamma}_{i,j}^{fix+CH_4}}{\hat{\Gamma}_{i,j}^{fix}}\right)\left(\frac{\hat{\Gamma}_{i,j}^{fix+CH_4+N_2O}}{\hat{\Gamma}_{i,j}^{fix+CH_4}}\right)\left(\frac{\hat{\Gamma}_{i,j}^{fix+CH_4+N_2O+CO_2}}{\hat{\Gamma}_{i,j}^{fix+CH_4+N_2O}}\right)\left(\frac{\hat{\Gamma}_{\vec{\nu}^*,j}^{fix+CH_4+N_2O+CO_2+wv}}{\hat{\Gamma}_{\vec{\nu}^*,j}^{fix+CH_4+N_2O+CO_2}}\right)\left(\frac{\hat{\tau}_{i,j}^{fix+CH_4+N_2O+CO_2+H_2O+O_3}}{\hat{\tau}_{i,j}^{fix+CH_4+N_2O+CO_2+H_2O}}\right)$$

Interval 6 [1250.25 to 1350 cm^{-1}]

$$\hat{\Gamma}_{i,j}^{tot} = \hat{\Gamma}_{i,j}^{fix}\left(\frac{\hat{\Gamma}_{i,j}^{fix+CH_4}}{\hat{\Gamma}_{i,j}^{fix}}\right)\left(\frac{\hat{\Gamma}_{i,j}^{fix+CH_4+N_2O}}{\hat{\Gamma}_{i,j}^{fix+CH_4}}\right)\left(\frac{\hat{\Gamma}_{i,j}^{fix+CH_4+N_2O+CO_2}}{\hat{\Gamma}_{i,j}^{fix+CH_4+N_2O}}\right)\left(\frac{\hat{\Gamma}_{i,j}^{fix+CH_4+N_2O+CO_2+H_2O}}{\hat{\Gamma}_{i,j}^{fix+CH_4+N_2O+CO_2}}\right)$$

Interval 7 [1350.25 to 1400 cm^{-1}]

$$\hat{\Gamma}_{i,j}^{tot} = \hat{\Gamma}_{i,j}^{fix}\left(\frac{\hat{\Gamma}_{i,j}^{fix+CH_4}}{\hat{\Gamma}_{i,j}^{fix}}\right)\left(\frac{\hat{\Gamma}_{i,j}^{fix+CH_4+CO_2}}{\hat{\Gamma}_{i,j}^{fix+CH_4}}\right)\left(\frac{\hat{\Gamma}_{i,j}^{fix+H_2O+CH_4+CO_2}}{\hat{\Gamma}_{i,j}^{fix+CH_4+CO_2}}\right)$$

Table 5. The combination of gases used to compute the LbL transmittances.

Interval 8 [1400.25 to 1649.75 cm^{-1}]

$$\hat{\Gamma}^{tot}_{i,j} = \hat{\Gamma}^{fix}_{i,j}\left(\frac{\hat{\Gamma}^{fix+CH_4}_{i,j}}{\hat{\Gamma}^{fix}_{i,j}}\right)\left(\frac{\hat{\Gamma}^{fix+H_2O+CH_4}_{i,j}}{\hat{\Gamma}^{fix+CH_4}_{i,j}}\right)$$

Interval 9 [1650 to 1750 cm^{-1}]

$$\hat{\Gamma}^{tot}_{i,j} = \hat{\Gamma}^{fix}_{i,j}\left(\frac{\hat{\Gamma}^{fix+CH_4}_{i,j}}{\hat{\Gamma}^{fix}_{i,j}}\right)\left(\frac{\hat{\Gamma}^{fix+H_2O+CH_4}_{i,j}}{\hat{\Gamma}^{fix+CH_4}_{i,j}}\right)\left(\frac{\hat{\Gamma}^{fix+H_2O+CH_4+O_3}_{i,j}}{\hat{\Gamma}^{fix+H_2O+CH_4}_{i,j}}\right)$$

Interval 10 [1750.25 to 1850 cm^{-1}]

$$\hat{\Gamma}^{tot}_{i,j} = \hat{\Gamma}^{fix}_{i,j}\left(\frac{\hat{\Gamma}^{fix+H_2O}_{i,j}}{\hat{\Gamma}^{fix}_{i,j}}\right)\left(\frac{\hat{\Gamma}^{fix+H_2O+O_3}_{i,j}}{\hat{\Gamma}^{fix+H_2O}_{i,j}}\right)$$

Interval 11 [1850.25 to 1900 cm^{-1}]

$$\hat{\Gamma}^{tot}_{i,j} = \hat{\Gamma}^{fix}_{i,j}\left(\frac{\hat{\Gamma}^{fix+N_2O}_{i,j}}{\hat{\Gamma}^{fix}_{i,j}}\right)\left(\frac{\hat{\Gamma}^{fix+CO_2+N_2O}_{i,j}}{\hat{\Gamma}^{fix+N_2O}_{i,j}}\right)\left(\frac{\hat{\Gamma}^{fix+H_2O+CO_2+N_2O}_{i,j}}{\hat{\Gamma}^{fix+CO_2+N_2O}_{i,j}}\right)\left(\frac{\hat{\Gamma}^{fix+H_2O+CO_2+N_2O+O_3}_{i,j}}{\hat{\Gamma}^{fix+H_2O+CO_2+N_2O}_{i,j}}\right)$$

Interval 12 [1900.25 to 1994.75 cm^{-1}]

$$\hat{\Gamma}^{tot}_{i,j} = \hat{\Gamma}^{fix}_{i,j}\left(\frac{\hat{\Gamma}^{fix+CO_2}_{i,j}}{\hat{\Gamma}^{fix}_{i,j}}\right)\left(\frac{\hat{\Gamma}^{fix+H_2O+CO_2}_{i,j}}{\hat{\Gamma}^{fix+CO_2}_{i,j}}\right)\left(\frac{\hat{\Gamma}^{fix+H_2O+CO_2+O_3}_{i,j}}{\hat{\Gamma}^{fix+H_2O+CO_2}_{i,j}}\right)$$

Interval 13 [1995 to 2295 cm^{-1}]

$$\hat{\Gamma}^{tot}_{i,j} = \hat{\Gamma}^{fix}_{i,j}\left(\frac{\hat{\Gamma}^{fix+CO}_{i,j}}{\hat{\Gamma}^{fix}_{i,j}}\right)\left(\frac{\hat{\Gamma}^{fix+CO+N_2O}_{i,j}}{\hat{\Gamma}^{fix+CO}_{i,j}}\right)\left(\frac{\hat{\Gamma}^{fix+CO+N_2O+CO_2}_{i,j}}{\hat{\Gamma}^{fix+CO+N_2O}_{i,j}}\right)\left(\frac{\hat{\Gamma}^{fix+CO+N_2O+CO_2+H_2O}_{i,j}}{\hat{\Gamma}^{fix+CO+N_2O+CO_2}_{i,j}}\right)\left(\frac{\hat{\Gamma}^{fix+CO+N_2O+CO_2+H_2O+O_3}_{i,j}}{\hat{\Gamma}^{fix+CO+N_2O+CO_2+H_2O}_{i,j}}\right)$$

Interval 14 [2295.25 to 2359.75 cm^{-1}]

$$\hat{\Gamma}^{tot}_{i,j} = \hat{\Gamma}^{fix}_{i,j}\left(\frac{\hat{\Gamma}^{fix+CO_2}_{i,j}}{\hat{\Gamma}^{fix}_{i,j}}\right)\left(\frac{\hat{\Gamma}^{fix+H_2O+CO_2}_{i,j}}{\hat{\Gamma}^{fix+CO_2}_{i,j}}\right)$$

Table 5. The combination of gases used to compute the LbL transmittances (cont).

Interval 15 [2360 to 2660 cm^{-1}]

$$\hat{\Gamma}^{tot}_{i,j} = \hat{\Gamma}^{fix}_{i,j} \left(\frac{\hat{\Gamma}^{fix+CH_4}_{i,j}}{\hat{\Gamma}^{fix}_{i,j}} \right) \left(\frac{\hat{\Gamma}^{fix+CH_4+N_2O}_{i,j}}{\hat{\Gamma}^{fix+CH_4}_{i,j}} \right) \left(\frac{\hat{\Gamma}^{fix+CH_4+N_2O+CO_2}_{i,j}}{\hat{\Gamma}^{fix+CH_4+N_2O}_{i,j}} \right) \left(\frac{\hat{\Gamma}^{fix+CH_4+N_2O+CO_2+H_2O}_{i,j}}{\hat{\Gamma}^{fix+CH_4+N_2O+CO_2}_{i,j}} \right)$$

Interval 16 [2660.25 to 2760 cm^{-1}]

$$\hat{\Gamma}^{tot}_{i,j} = \hat{\Gamma}^{fix}_{i,j} \left(\frac{\hat{\Gamma}^{fix+CH_4}_{i,j}}{\hat{\Gamma}^{fix}_{i,j}} \right) \left(\frac{\hat{\Gamma}^{fix+H_2O+CH_4}_{i,j}}{\hat{\Gamma}^{fix+CH_4}_{i,j}} \right)$$

Table 5. The combination of gases used to compute the LbL transmittances (cont).

Predictor	Fixed gases	CO_2	O_3
$X_{j,1}$	$\sec(\theta)$	$\sec(\theta) CO2_r(j)$	$\sec(\theta) O_r(j)$
$X_{j,2}$	$\sec^2(\theta)$	$T_r^2(j)$	$\sqrt{\sec(\theta) O_r(j)}$
$X_{j,3}$	$\sec(\theta) T_r(j)$	$\sec(\theta) T_r(j)$	$\frac{\sec(\theta) O_r(j)}{O_w(j)}$
$X_{j,4}$	$\sec(\theta) T_r^2(j)$	$\sec(\theta) T_r^2(j)$	$(\sec(\theta) O_r(j))^2$
$X_{j,5}$	$T_r(j)$	$T_r(j)$	$\sqrt{\sec(\theta) O_r(j)}\, \delta T(j)$
$X_{j,6}$	$T_r^2(j)$	$\sec(\theta) T_w(j)$	$\sec(\theta) O_r^2(j) O_w(j)$
$X_{j,7}$	$\sec(\theta) T_{fw}(j)$	$(\sec(\theta) CO2_w(j))^2$	$\frac{O_r(j)}{O_w(j)} \sqrt{\sec(\theta O_r(j)}$
$X_{j,8}$	$\sec(\theta) T_{fu}(j)$	$\sec(\theta)\, T_w(j) \sqrt{T_r(j)}$	$(\sec(\theta)\, O_w(j))^{1.75}$
$X_{j,9}$	$\sec(\theta)\ \ T_r^3$	$\sqrt{\sec(\theta) CO2_r(j)}$	$O_r(j) \sec(\theta) \sqrt{O_w(j) \sec(\theta)}$
$X_{j,10}$	$\sec(\theta)\ \sqrt{\sec(\theta) T_r(j)}$	$T_r^3(j)$	$\sec(\theta) O_w(j)$
$X_{j,11}$	0	$\sec(\theta)\, T_r^3(j)$	$(\sec(\theta) O_w(j))^2$
$X_{j,12}$	0	$\sec(\theta)\, T_r^2(j)\, T_w^3(j)$	$\sqrt{\sec(\theta)}\, O_w^2(j)\, \delta T(j)$
$X_{j,13}$	0	$(T_r(j)\, T_w(j))^2$	$\sec(\theta) T_r^3(j)$
		[2000 cm^{-1}-2295 cm^{-1}]	
$X_{j,14}$	$\sec(\theta) CO_r(j)$		

Table 6. Predictors used in RTTOV-9 for Fixed gases, CO_2 and ozone channels in the shortwave region of the spectrum.

Predictor	CO	N_2O	CH_4
$X_{j,1}$	$\sec(\theta)\, CO_r(j)$	$\sec(\theta)\, N2O_r(j)$	$\sec(\theta)\, CH4_r(j)$
$X_{j,2}$	$\sqrt{\sec(\theta)\, CO_r(j)}$	$\sqrt{\sec(\theta)\, N2O_r(j)}$	$\sqrt{\sec(\theta)\, CH4_r(j)}$
$X_{j,3}$	$\sec(\theta)\, CO_r(j)\, \delta T(j)$	$\sec(\theta)\, N2O_r(j)\, \delta T(j)$	$\sec(\theta)\, CH4_r(j)\, \delta T(j)$
$X_{j,4}$	$(\sec(\theta)\, CO_r(j))^2$	$(\sec(\theta)\, N2O_r(j))^2$	$(\sec(\theta)\, CH4_r(j))^2$
$X_{j,5}$	$\sqrt{\sec(\theta)\, CO_r(j)}\, \delta T(j)$	$N2O_r(j)\, \delta T(j)$	$CH4_r(j)\, \delta T(j)$
$X_{j,6}$	$\sqrt[4]{\sec(\theta)\, CO_r(j)}$	$\sqrt[4]{\sec(\theta)\, N2O_r(j)}$	$\sqrt[4]{\sec(\theta)\, CH4_r(j)}$
$X_{j,7}$	$\sec(\theta)\, CO_r(j)\, \delta T(j) \lvert \delta T(j) \rvert$	$\sec(\theta)\, N2O_w(j)$	$\sec(\theta)\, CH4_{tw}(j)$
$X_{j,8}$	$\dfrac{\sec(\theta)\, CO_r^2(j)}{CO_w(j)}$	$\sec(\theta)\, N2O_{tw}(j)$	$CH4_{tw}(j)$
$X_{j,9}$	$\dfrac{\sqrt{\sec(\theta)\, CO_r(j)}\, CO_r(j)}{CO_w(j)}$	$(\sec(\theta)\ \ N2O_{tw}(j))^2$	$(\sec(\theta)\, CH4_w(j))^2$
$X_{j,10}$	$\dfrac{\sec(\theta)\, CO_r^2(j)}{\sqrt{CO_w(j)}}$	$\dfrac{\sqrt{\sec(\theta)\, N2O_r(j)}\, N2O_r(j)}{N2O_w(j)}$	$\sec(\theta)\, CH4_w(j)$
$X_{j,11}$	$(\sec(\theta)\ CO_{tw}(j))^{0.4}$	$(\sec(\theta)\ \ N2O_{tw}(j))^3$	$\dfrac{\sqrt{\sec(\theta)\, CH4_r(j)}\, CH4_r(j)}{CH4_w(j)}$
$X_{j,12}$	$(\sec(\theta)\ CO_{tw}(j))^{0.25}$	$\sec(\theta)^2\, N2O_{tw}(j)\, \delta T(J)$	
		[2000 cm^{-1}-2295 cm^{-1}]	
$X_{j,13}$		$\sec(\theta)\, CO_r(j)$	
$X_{j,14}$		$\sec(\theta)^2\, CO_r(j)\, CO_w(j)$	

Table 7. Predictors used in RTTOV-9 for CO, N_2O and CH_4 channels in the shortwave region of the spectrum.

Predictor	H_2O	H_2O	H_2O
$X_{j,1}$	$(\sec(\theta) W_r(j))^2$	$(\sec(\theta) W_r(j))^2$	$(\sec(\theta) W_r(j))^2$
$X_{j,2}$	$\sec(\theta) W_w(j)$	$\sec(\theta) W_w(j)$	$\sec(\theta) W_w(j)$
$X_{j,3}$	$(\sec(\theta) W_w(j))^2$	$(\sec(\theta) W_w(j))^2$	$(\sec(\theta) W_w(j))^2$
$X_{j,4}$	$\sec(\theta) W_r(j) \delta T(j)$	$\sec(\theta) W_r(j) \delta T(j)$	$\sqrt{\sec(\theta) W_r(j)}$
$X_{j,5}$	$\sqrt{\sec(\theta) W_r(j)}$	$\sqrt{\sec(\theta) W_r(j)}$	$\sqrt{\sec(\theta) W_r(j)}$
$X_{j,6}$	$\sqrt[4]{\sec(\theta) W_r(j)}$	$\sqrt[4]{\sec(\theta) W_r(j)}$	$\sqrt[4]{\sec(\theta) W_r(j)}$
$X_{j,7}$	$\sec(\theta) W_r(j)$	$\sec(\theta) W_r(j)$	$\sec(\theta) W_r(j)$
$X_{j,8}$	$(\sec(\theta) \ W_w(j))^{1.5}$	$(\sec(\theta) \ W_w(j))^{1.5}$	$(\sec(\theta) \ W_w(j))^{1.5}$
$X_{j,9}$	$(\sec(\theta) \ W_r(j))^{1.5}$	$(\sec(\theta) \ W_r(j))^{1.5}$	$(\sec(\theta) \ W_r(j))^{1.5}$
$X_{j,10}$	$\sec(\theta) W_r(j) \delta T(j) \lvert \delta T(j) \rvert$	$\sec(\theta) W_r(j) \delta T(j) \lvert \delta T(j) \rvert$	
	$(\sqrt{\sec(\theta) W_r(j)}) \delta T(j)$		
$X_{j,11}$	$(\sqrt{\sec(\theta) W_r(j)}) \delta T(j)$	$(\sqrt{\sec(\theta) W_r(j)}) \delta T(j)$	$(\sec(\theta) \ W_w(j))^{1.25}$
$X_{j,12}$	$(\sec(\theta) \ W_w(j))^{1.25}$	$(\sec(\theta) \ W_w(j))^{1.25}$	$(\sec(\theta) W_r(J))^{1.5} \ \delta T(j)$
$X_{j,13}$	$(\sqrt{\sec(\theta) \ W_r(j)}) \ W_r(j)$	$(\sqrt{\sec(\theta) \ W_r(j)}) \ W_r(j)$	$\frac{\sec(\theta) W_r^2(j)}{W_w(j)}$
$X_{j,14}$	$\sec(\theta) CO2_r(j)$	0	$(\sec(\theta) CH4_r(J))^{1.25}$
$X_{j,15}$	$\sec(\theta) CO_r(j)$	0	
	$(\sec(\theta) CH4_r(J))^{1.25} \ \delta T(j)$		
	[2000 cm^{-1}-2295 cm^{-1}]	***[2000 cm^{-1}-2359.75 cm^{-1}]***	***[2360 cm^{-1}-2760 cm^{-1}]***

Table 8. Predictors used in RTTOV-9 for Water vapour (line absorption) channels in the shortwave region of the spectrum.

Aerosol type	Aerosol component	N (cm^{-3})
Continental clean	Water soluble	2600
	Insoluble	0.15
Continental average	Water soluble	7000
	Insoluble	0.4
	Soot	8300
Continental polluted	Water soluble	15700
	Insoluble	0.6
	Soot	34300
Urban	Water soluble	28000
	Insoluble	1.5
	Soot	130000
Desert	Water soluble	2000
	Mineral (nuc.)	296.5
	Mineral (acc.)	30.5
	Mineral (coa.)	0.142
Maritime clean	Water soluble	1520
	Seal Salt (acc.)	20
	Sea Salt (coa.)	3.2E-03
Maritime polluted	Water soluble	9000
	Sea salt (acc.)	20
	Sea salt (coa.)	3.2E-03
	Soot	5180
Maritime tropical	Water soluble	590
	Sea salt (acc.)	10
	Sea salt (coa.)	1.3E-03
Arctic	Water soluble	1300
	Insoluble	0.001
	Sea salt (acc.)	1.9
	Soot	5300
Antarctic	Sulphate droplets	42.9
	Sea salt (acc.)	0.47E-01
	Mineral transported	0.53E-02

Table 9. Composition of aerosol types included in RTTOV-9.

Aerosol components
Insoluble
Water-soluble
Soot
Sea salt (acc. mode)
Sea salt (coa. mode)
Mineral (nuc. mode)
Mineral (acc. mode)
Mineral (coa. mode)
Mineral-transported
Sulphate droplets
Volcanic ash

Table 10. The aerosol components included in RTTOV-9.

Cloud type	$\bar{N}$(cm^{-3})	LWC($g\ m^{-3}$)
Stratus Continental	250	0.28
Stratus Maritime	80	0.30
Cumulus Continental Clean	400	0.26
Cumulus Continental Polluted	1300	0.30
Cumulus Maritime	65	0.44

Table 11. The water cloud types included in RTTOV-9.

Crystal length (μ m)	Method	Wavelength
4	T-matrix	Whole IASI spectrum
7.5	T-matrix	Whole IASI spectrum
15	T-matrix	Whole IASI spectrum
25	T-matrix	Whole IASI spectrum
35	T-matrix	Whole IASI spectrum
45	T-matrix	≥ 5μm
45	GO	<5μm
60	T-matrix	≥ 6μm
60	GO	<6μm
80	T-matrix	≥ 11μm
80	GO	<11μm
100	T-matrix	≥ 14μm
100	GO	<14μm
130	GO	Whole IASI spectrum

Table 12. The wavelength range covered by the GO and T-matrix method.

				Crystal length (μm)							
4	7.5	15	25	35	45	60	80	100	130	175	225
275	350	450	550	650	750	900	1150	1400	1750	2500	3500

Table 13. The length of the hexagonal crystals used in RTTOV-9.

Size distribution	**IWC(g m^{-3})**	**D_{ge}(μm)**
Heym. and Platt:-20ºC to -25ºC	0.024607	48.88
Heym. and Platt:-25ºC to -30ºC	0.025970	45.01
Heym. and Platt:-30ºC to -35ºC	0.022151	63.63
Heym. and Platt:-35ºC to -40ºC	0.028025	45.71
Heym. and Platt:-40ºC to -45ºC	0.005053	21.15
Heym. and Platt:-45ºC to -50ºC	0.002578	21.38
Heym. and Platt:-50ºC to -55ºC	0.002740	15.52
Heym. and Platt:-55ºC to -60ºC	0.000712	28.42
Takano and Liou: Cs	0.011171	35.25
Takano and Liou: Ci uncinus	0.254639	118.29
Takano and Liou: Warm	0.029529	28.20
Takano and Liou: Cold	0.010839	12.20
FIRE I: 1 November 1986	0.005773	61.23
FIRE I: 2 November 1986	0.015930	82.30
FIRE I: 22 October 1986	0.017963	88.35
FIRE I: 25 October 1986	0.032104	95.89
FIRE I: 28 October 1986	0.017084	93.16
FIRE II: 26 November 1991	0.014382	78.40
FIRE II: 5 December 1991	0.008185	68.61
CEPEX IWC: 10^{-4} to 10^{-3}	0.001176	23.80
CEPEX IWC: 10^{-3} to 10^{-2}	0.000608	29.10
CEPEX IWC: 10^{-2} to 10^{-1}	0.029735	47.32
CEPEX IWC: 10^{-1} to 0.32	0.113694	71.01
CEPEX 4 April:2250	0.014286	22.87
CEPEX 4 April:2341	0.002879	23.82
CEPEX 4 April:2342	0.003774	28.64
CEPEX 4 April:2347	0.027347	51.74
CEPEX 4 April:2348	0.051146	59.45
FU 1	0.012161	60.64
FU 2	0.033705	48.94

Table 14. The ice water content and generalized effective diameter for the ice crystal size distributions used in RTTOV-9 assuming the cirrus clouds are made of hexagonal ice crystals.

Size distribution	***IWC*** **(g m^{-3})**	D_{ge} **(μ m)**
Heym. and Platt:-20ºC to -25ºC	0.041199	133.09
Heym. and Platt:-25ºC to -30ºC	0.028480	86.84
Heym. and Platt:-30ºC to -35ºC	0.034519	130.04
Heym. and Platt:-35ºC to -40ºC	0.022984	66.29
Heym. and Platt:-40ºC to -45ºC	0.002386	29.26
Heym. and Platt:-45ºC to -50ºC	0.001004	24.37
Heym. and Platt:-50ºC to -55ºC	0.000471	8.88
Heym. and Platt:-55ºC to -60ºC	0.000399	39.55
Takano and Liou: Cs	0.003558	26.43
Takano and Liou: Ci uncinus	0.489046	166.46
Takano and Liou: Warm	0.019690	46.27
Takano and Liou: Cold	0.001455	5.61
FIRE I: 1 November 1986	0.004330	64.05
FIRE I: 2 November 1986	0.016316	88.42
FIRE I: 22 October 1986	0.025973	124.37
FIRE I: 25 October 1986	0.051856	139.28
FIRE I: 28 October 1986	0.026433	133.47
FIRE II: 26 November 1991	0.012638	76.16
FIRE II: 5 December 1991	0.005550	58.79
CEPEX IWC: 10^{-4} to 10^{-3}	0.000235	14.35
CEPEX IWC: 10^{-3} to 10^{-2}	0.001998	25.24
CEPEX IWC: 10^{-2} to 10^{-1}	0.027598	76.40
CEPEX IWC: 10^{-1} to 0.32	0.172762	128.97
CEPEX 4 April:2250	0.001700	9.01
CEPEX 4 April:2341	0.000348	9.45
CEPEX 4 April:2342	0.000733	15.82
CEPEX 4 April:2347	0.014495	45.51
CEPEX 4 April:2348	0.034329	57.97
FU 1	0.008983	63.03
FU 2	0.012709	32.52

Table 15. Ice water content and generalized effective diameter for the ice crystal size distributions used in RTTOV-9 assuming the cirrus clouds are made of ice crystal aggregates.

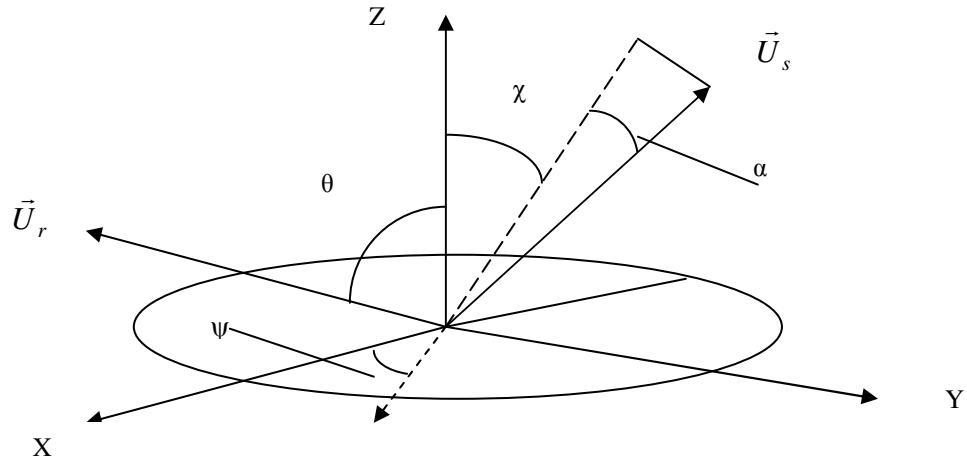

Figure 1. The geometry of reflection

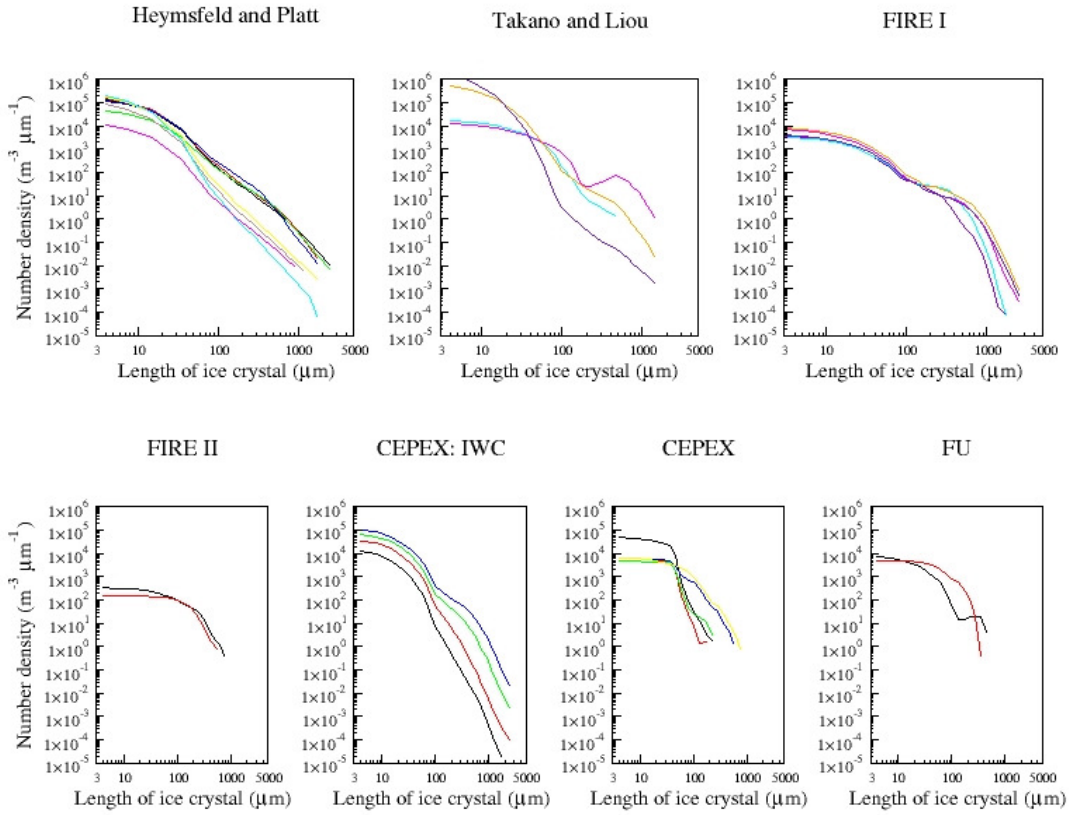

Figure 2. The ice crystal size distributions used in RTTOV-9

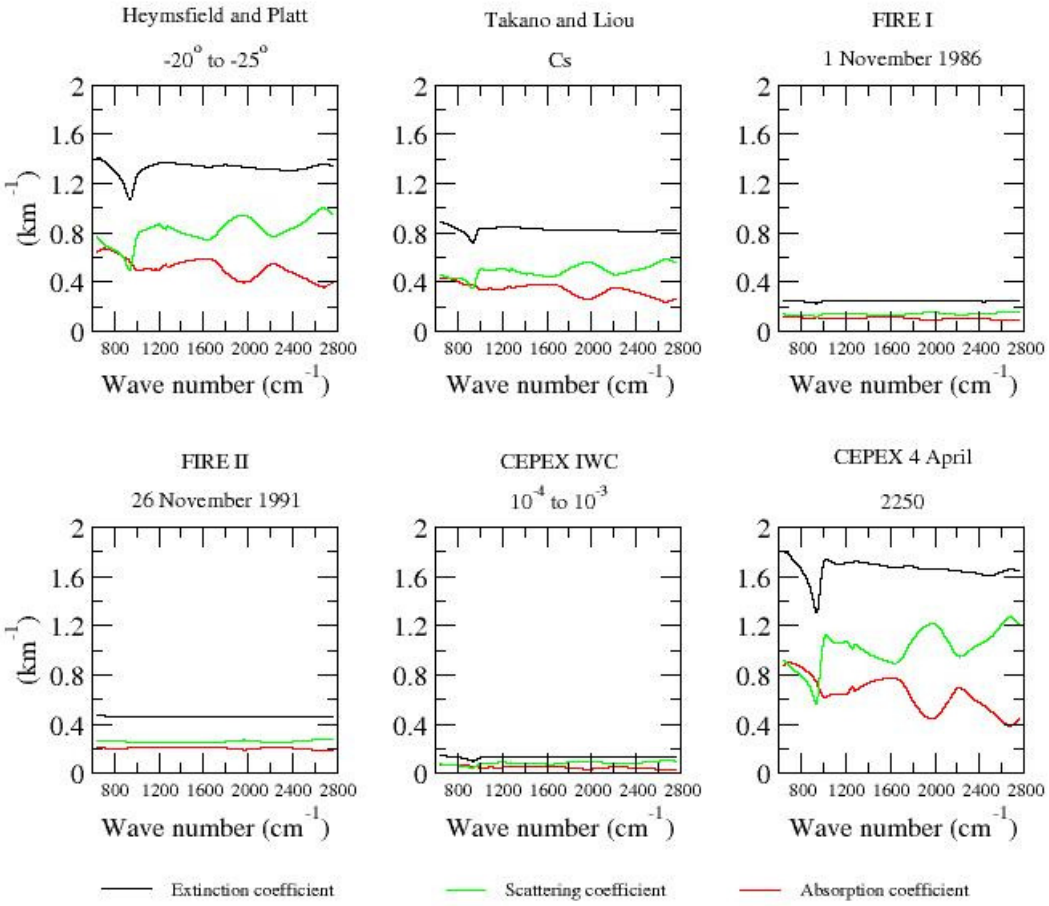

Figure 3. The absorption, scattering and extinction coefficient for a selected number of cirrus cloud types made of hexagonal ice crystals.

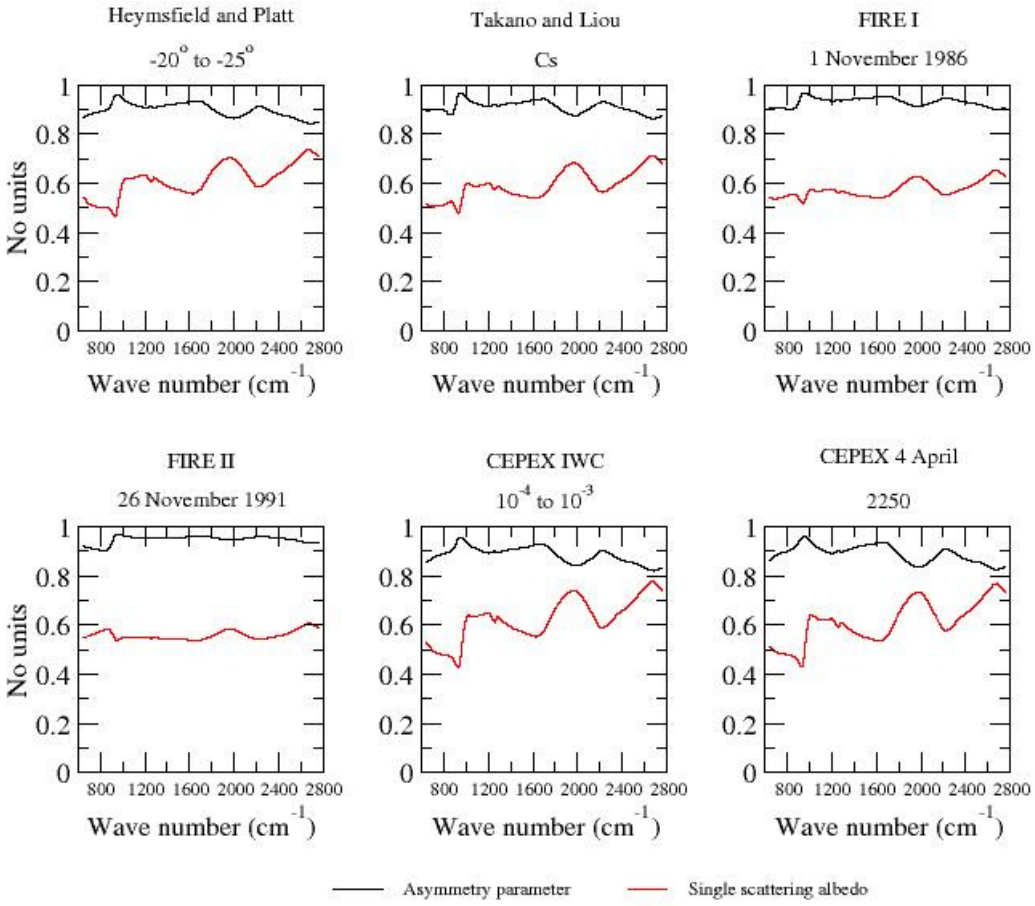

Figure 4. The single scattering albedo and asymmetry parameter for a selected number of cirrus cloud types made of hexagonal ice crystals.

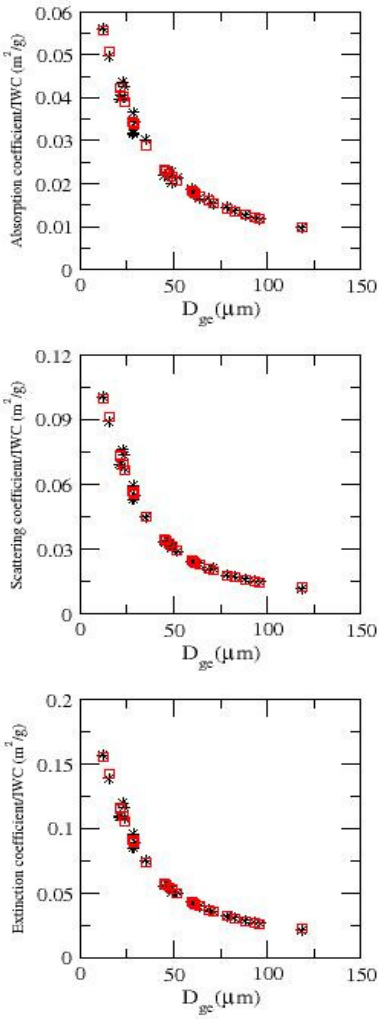

Figure 5. The absorption coefficient/IWC, the scattering coefficient/IWC and the extinction coefficient/IWC as a function of the generalized diameter D_{ge}. Cirrus clouds are assumed to be made of hexagonal ice crystals.

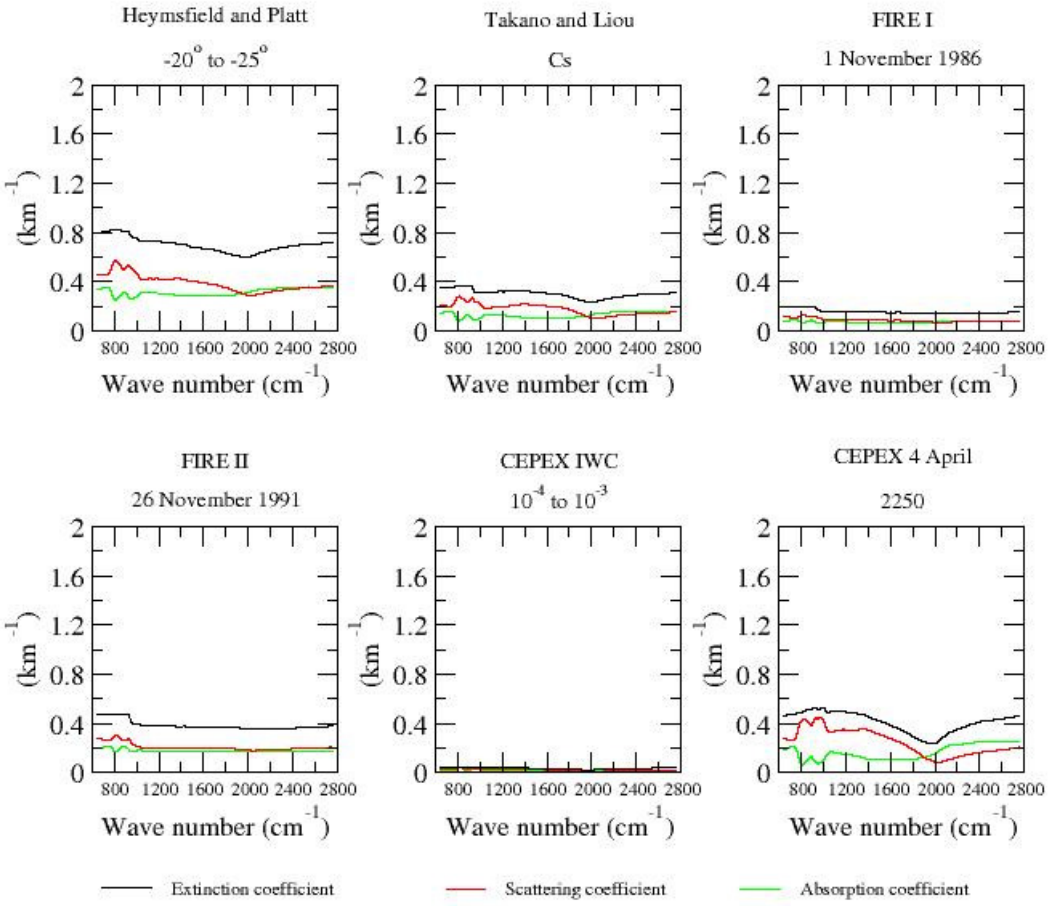

Figure 6. The absorption, scattering and extinction coefficient for a selected number of cirrus cloud types made of ice crystal aggregates.

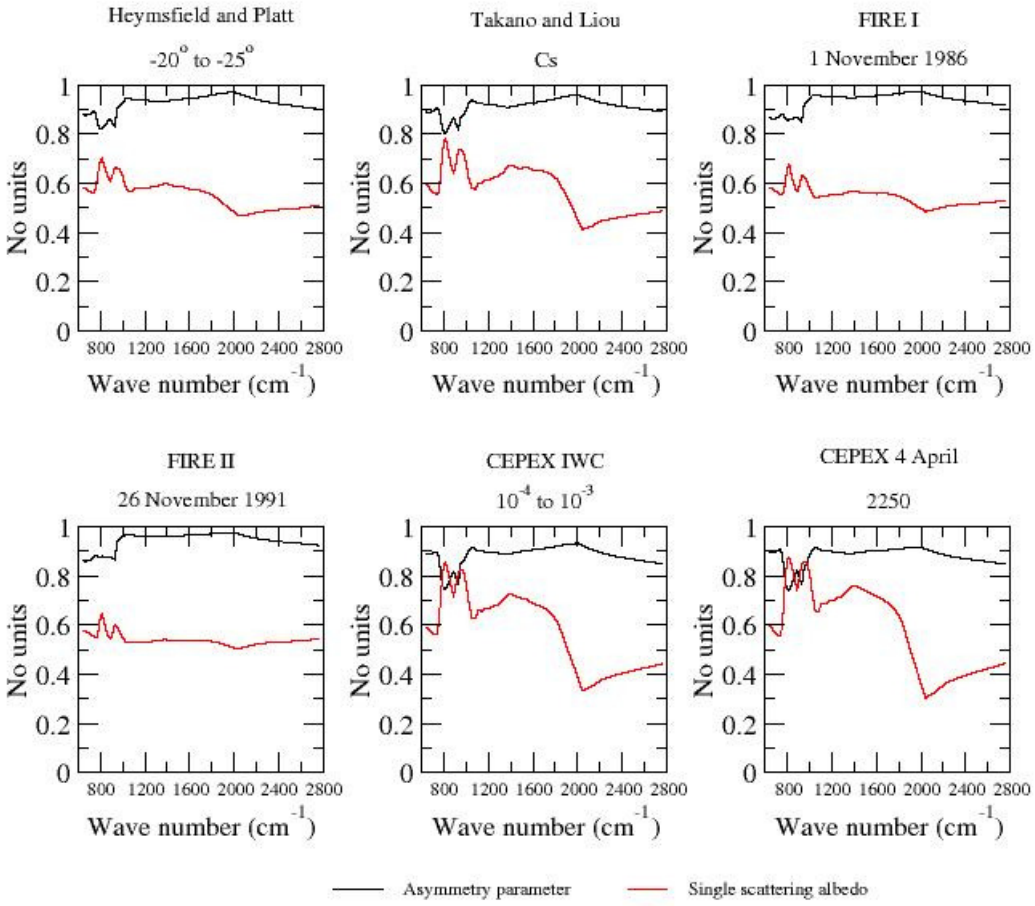

Figure 7. The single scattering albedo and asymmetry parameter for a selected number of cirrus cloud types made of ice crystal aggregates

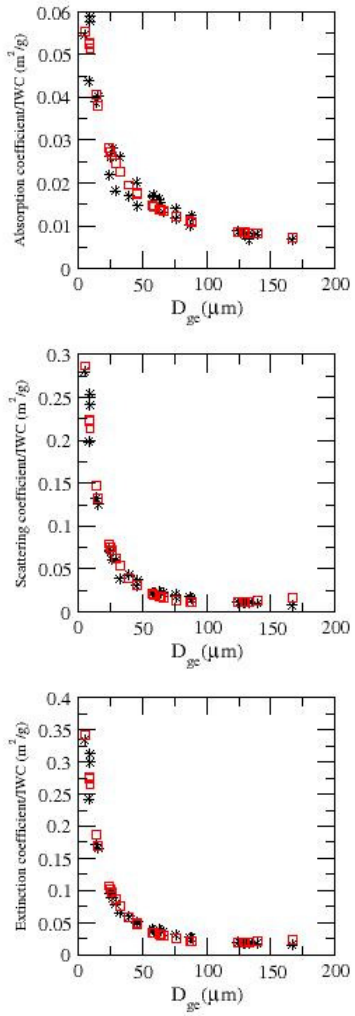

Figure 8. The absorption coefficient/IWC, the scattering coefficient/IWC and the extinction coefficient/IWC as a function of the generalized diameter D_{ge}. Cirrus clouds are assumed to be made of ice crystal aggregates.

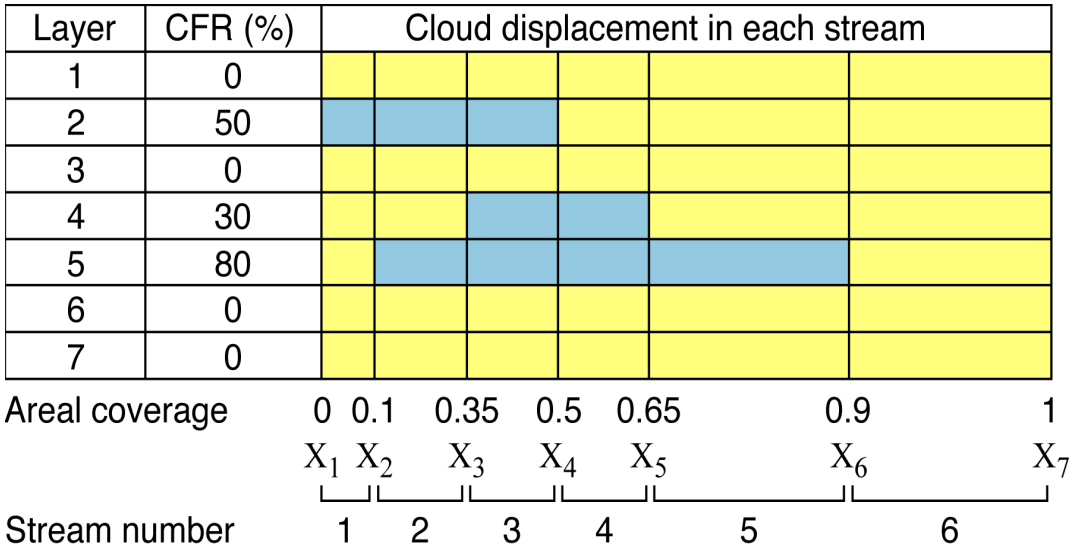

Figure 9. The cloud distribution in each stream.

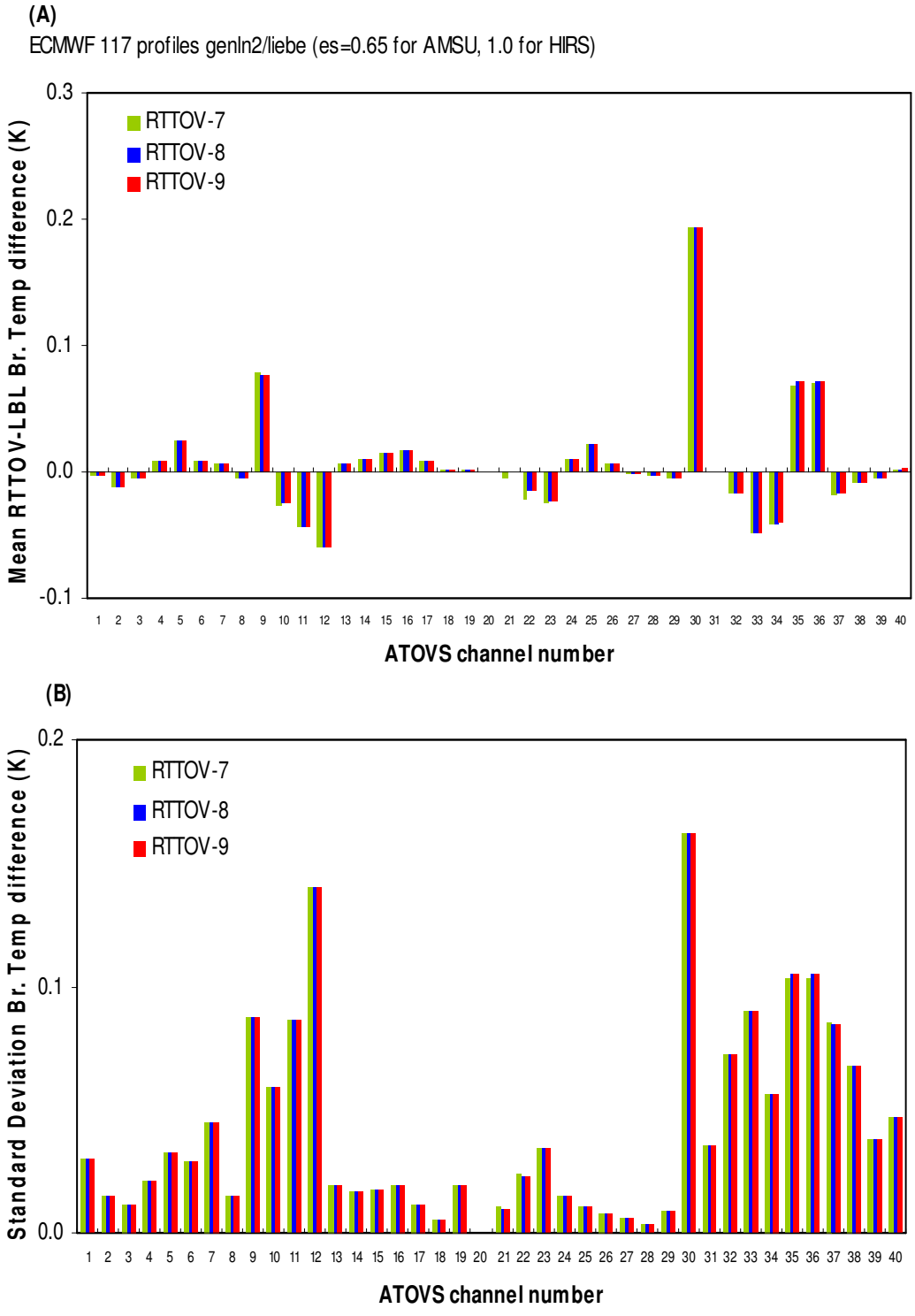

Figure 10. Bias (A) and standard deviation (B) of Line-by-Line vs RTTOV ATOVS simulated radiances for 117 diverse profiles. The same coefficient files are used for all 3 versions of the model.

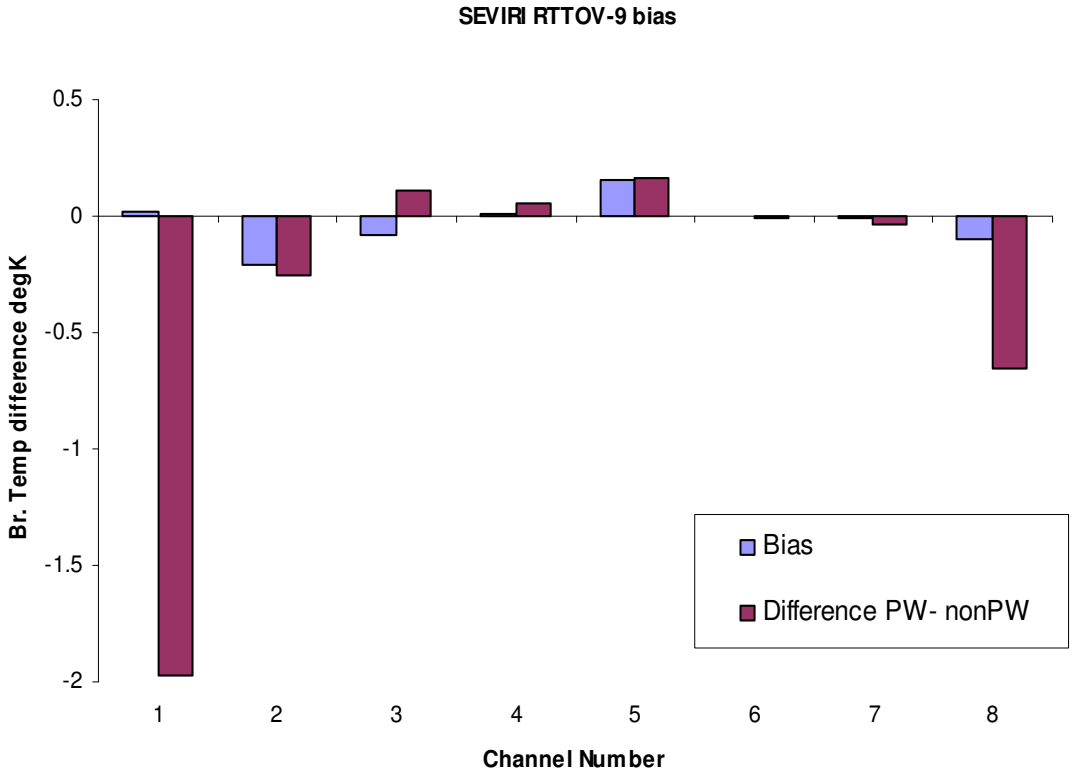

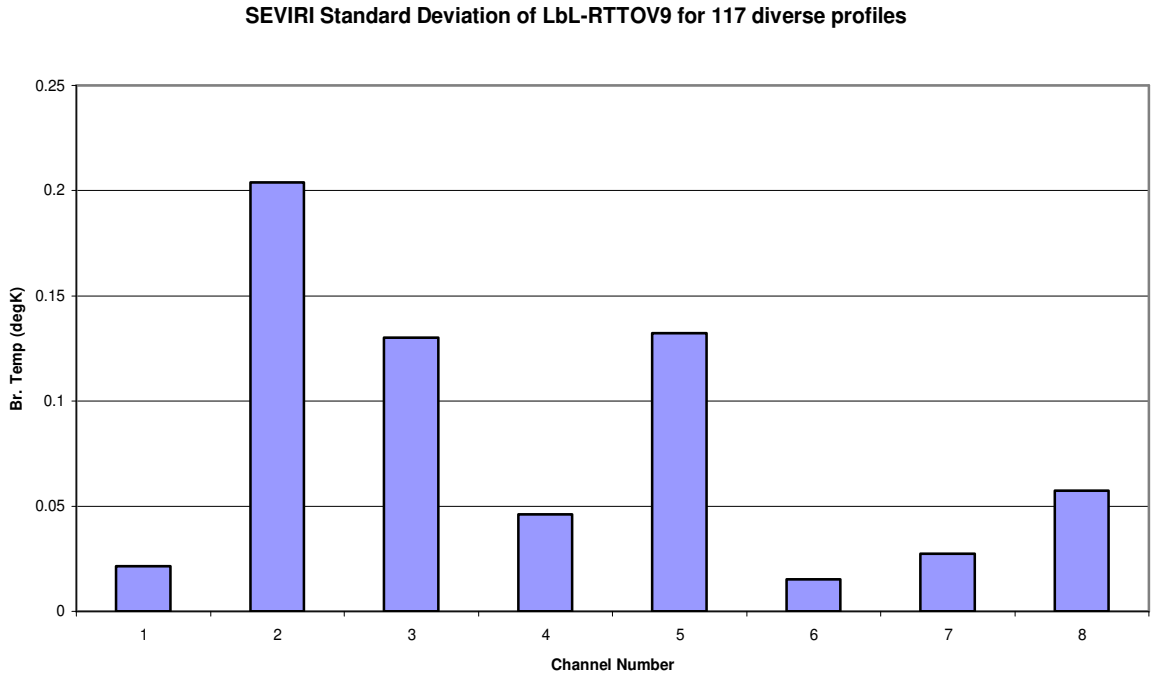

Figure 11.Comparison of Line-by-Line vs RTTOV-9 SEVIRI (MSG-1) simulated radiances for 117 diverse profiles. Top panel shows mean bias (blue) and also difference in bias (red) for plank weighted coefficients. Bottom panel shows standard deviation of difference.

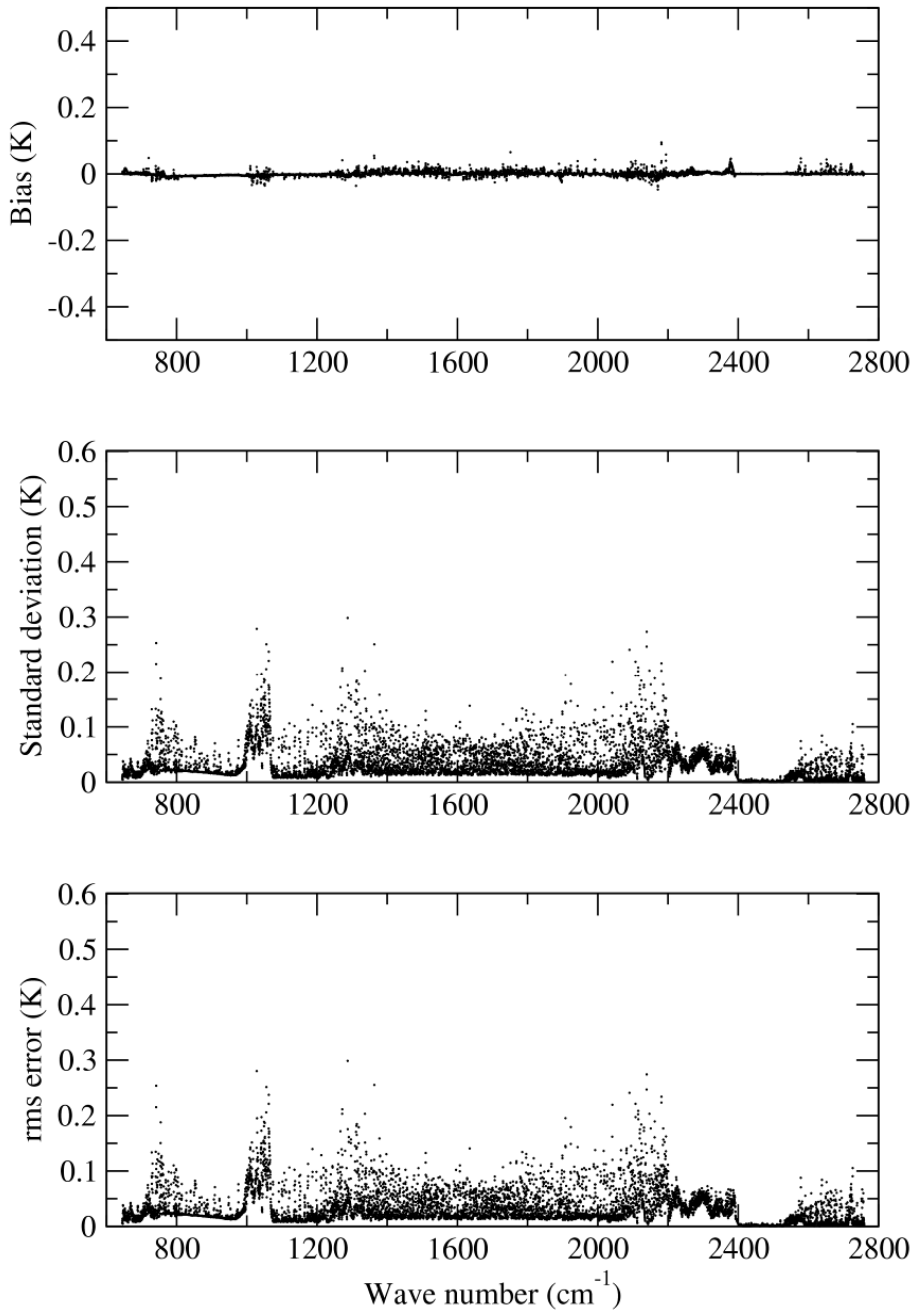

Figure 12. Mean value, standard deviation and rms of the difference between fast model and LBLRTM computed brightness temperatures for 83 diverse profiles and 6 viewing angles. Results are shown for the IASI channels.

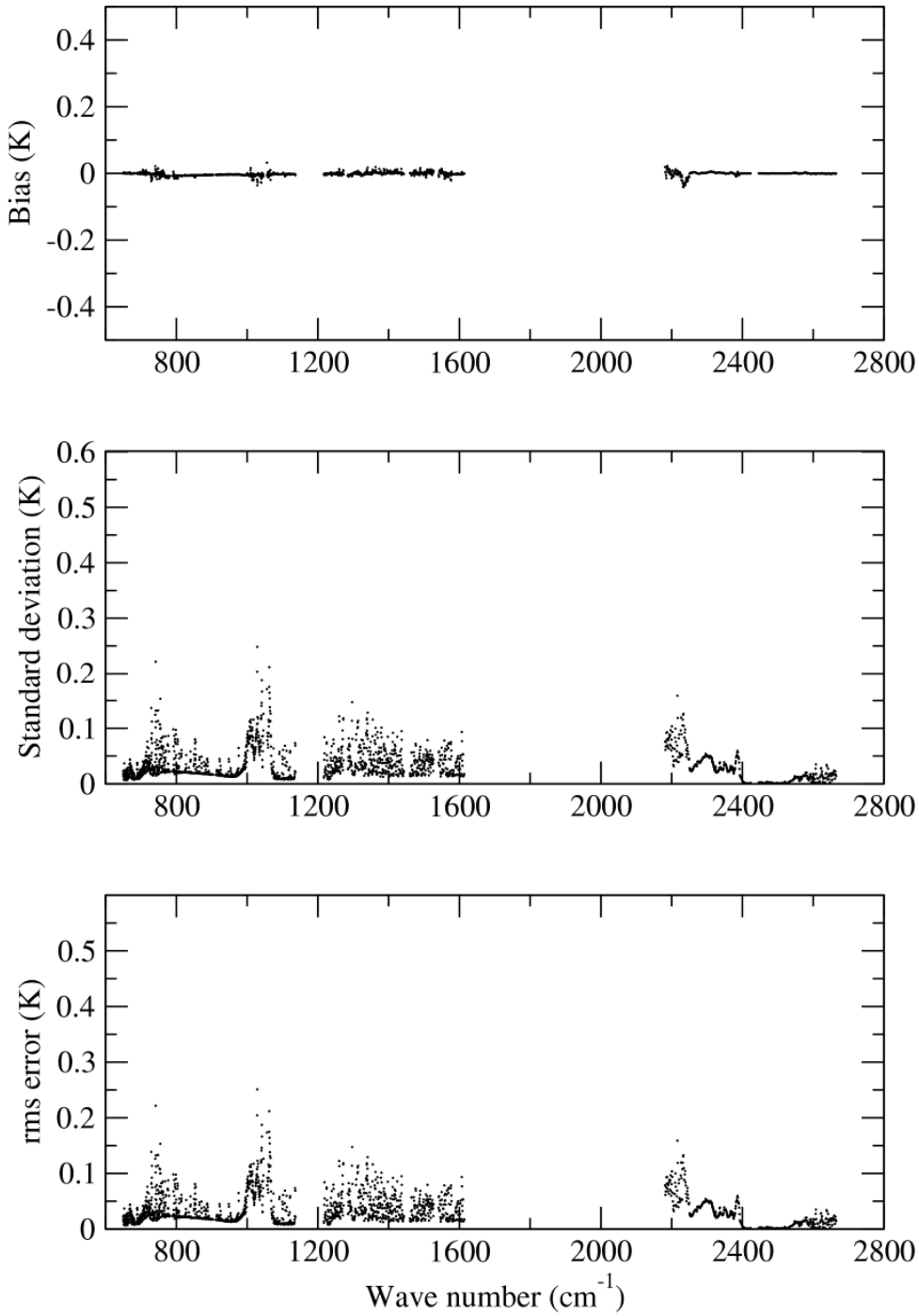

Figure 13. Mean value, standard deviation and rms of the difference between fast model and LBLRTM computed brightness temperatures for 83 diverse profiles and 6 viewing angles. Results are shown for the AIRS channels.

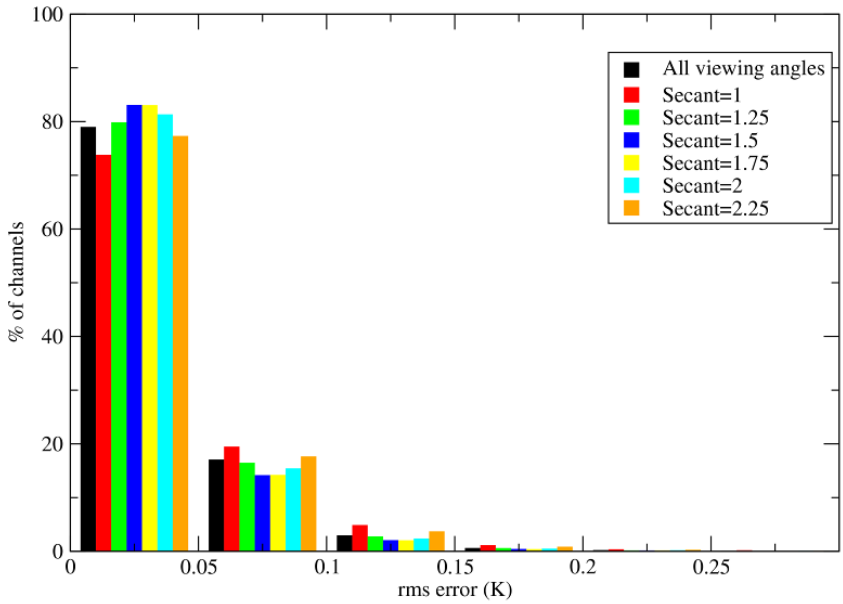

Figure 14. Histogram of the distribution of channels with rms error for six viewing angles. Results are shown for the IASI channels.

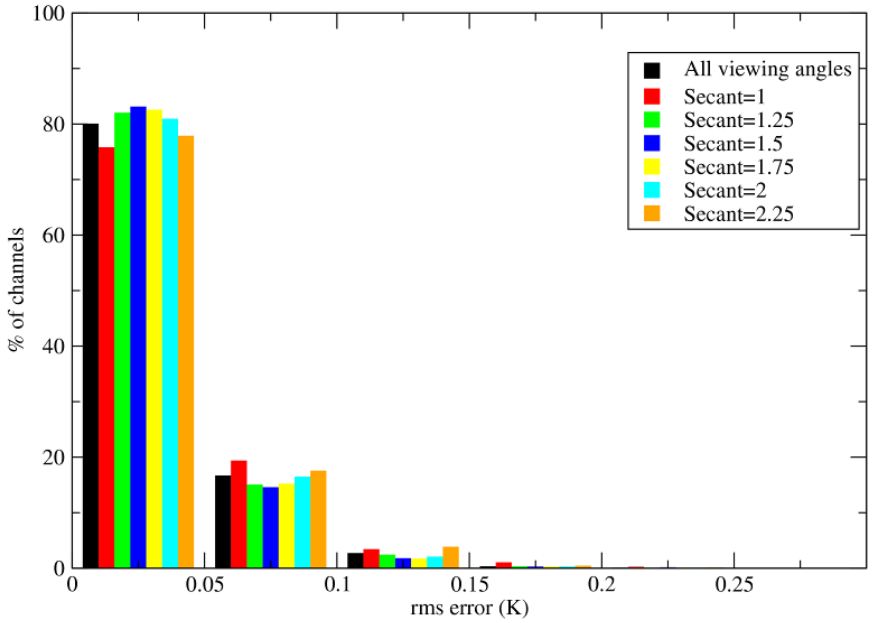

Figure 15. Histogram of the distribution of channels with rms error for six viewing angles. Results are shown for the AIRS channels

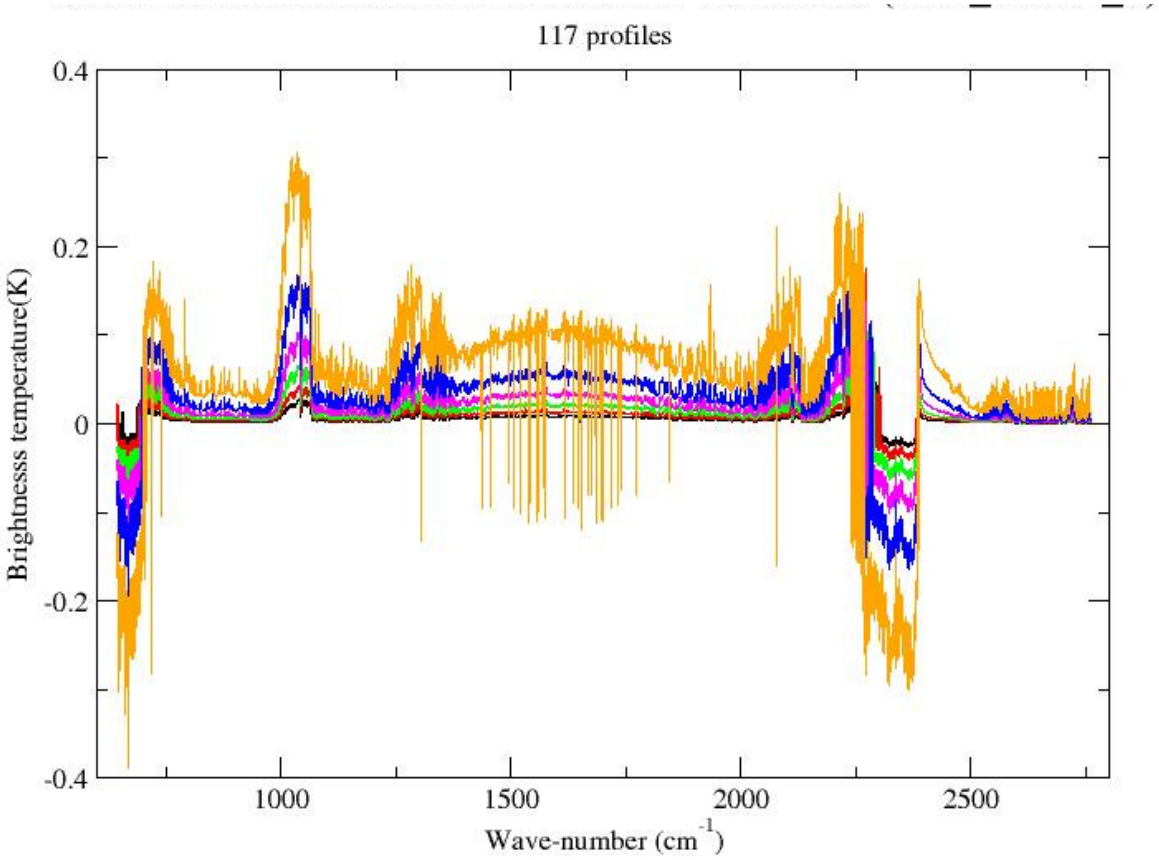

Figure 16. The maximum value of the differences between assuming a plane parallel atmosphere (RTTOV-8) and taking proper account of the local zenith angle variation with height (RTTOV-9) for IASI. The colours define the zenith angle at the surface increasing from 28 deg (black) to 53 deg (orange).

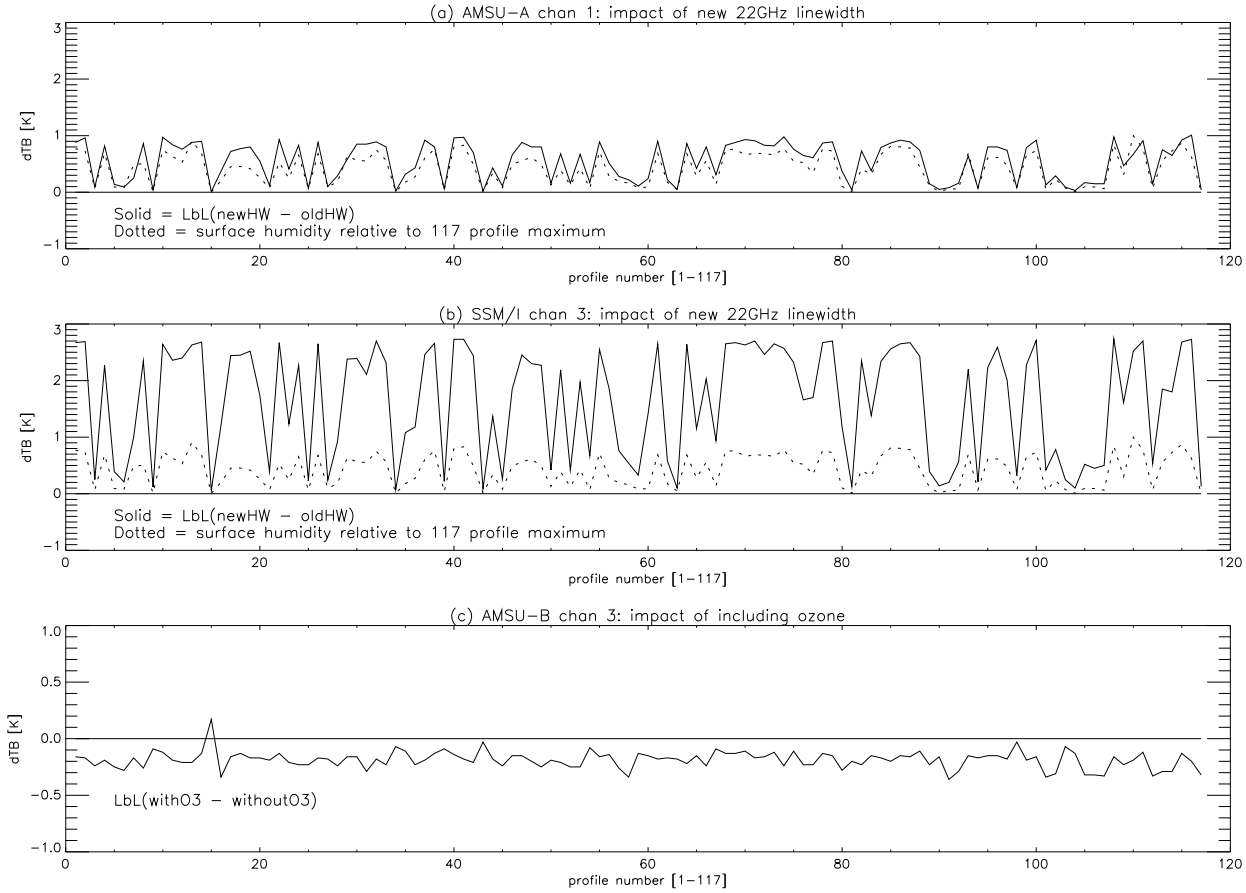

Figure 17. Impact on ToA brightness temperature of new microwave spectroscopy for an independent set of 117 profiles (a) effect on AMSU-A channel 1 of reducing the halfwidth of the 22GHz water vapour line (b) effect of halfwidth change on SSM/I channel 3 (c) effect of including ozone in the fixed gases on AMSU-B channel 3. As a guide to interpreting (a) and (b), a surface humidity index is shown dotted.

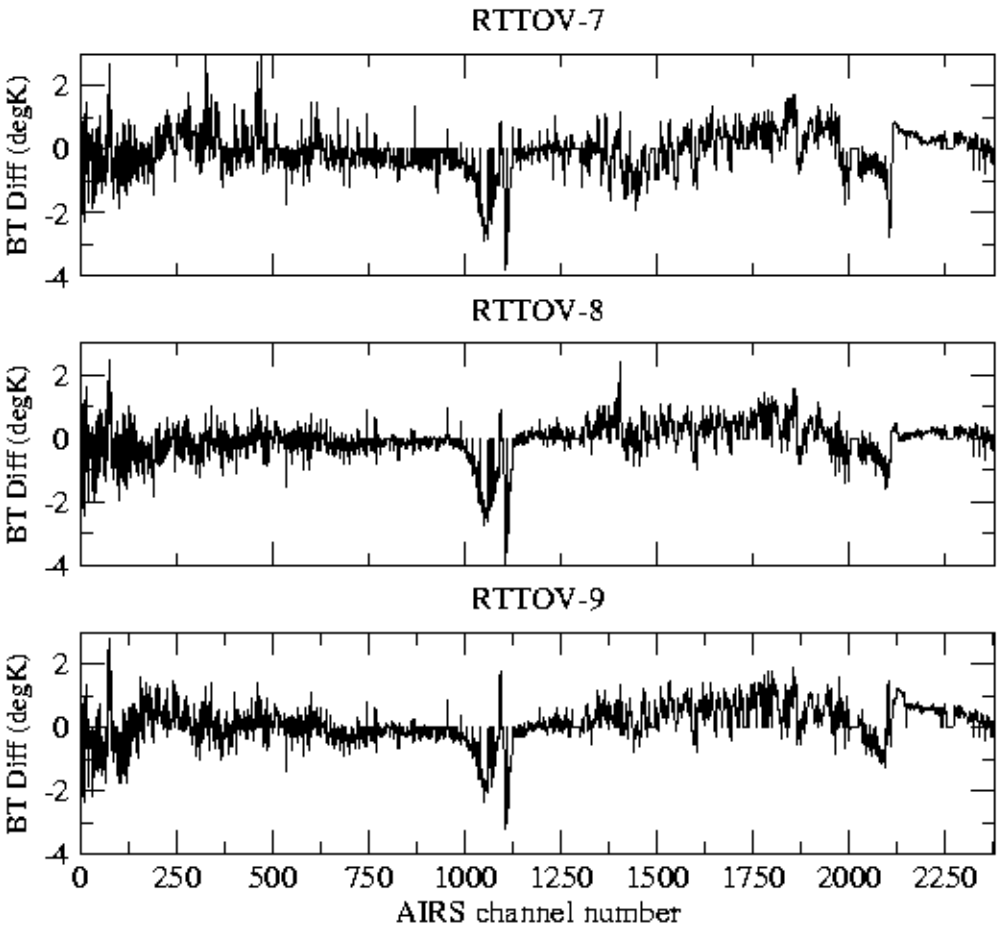

Figure 18: A comparison of RTTOV simulated AIRS radiances minus measured AIRS radiance for a tropical Pacific ARM profile. The values computed using GENLN2 RTTOV-7 and RTTOV-8 predictors and the new LBLRTM RTTOV-9 predictors are plotted.

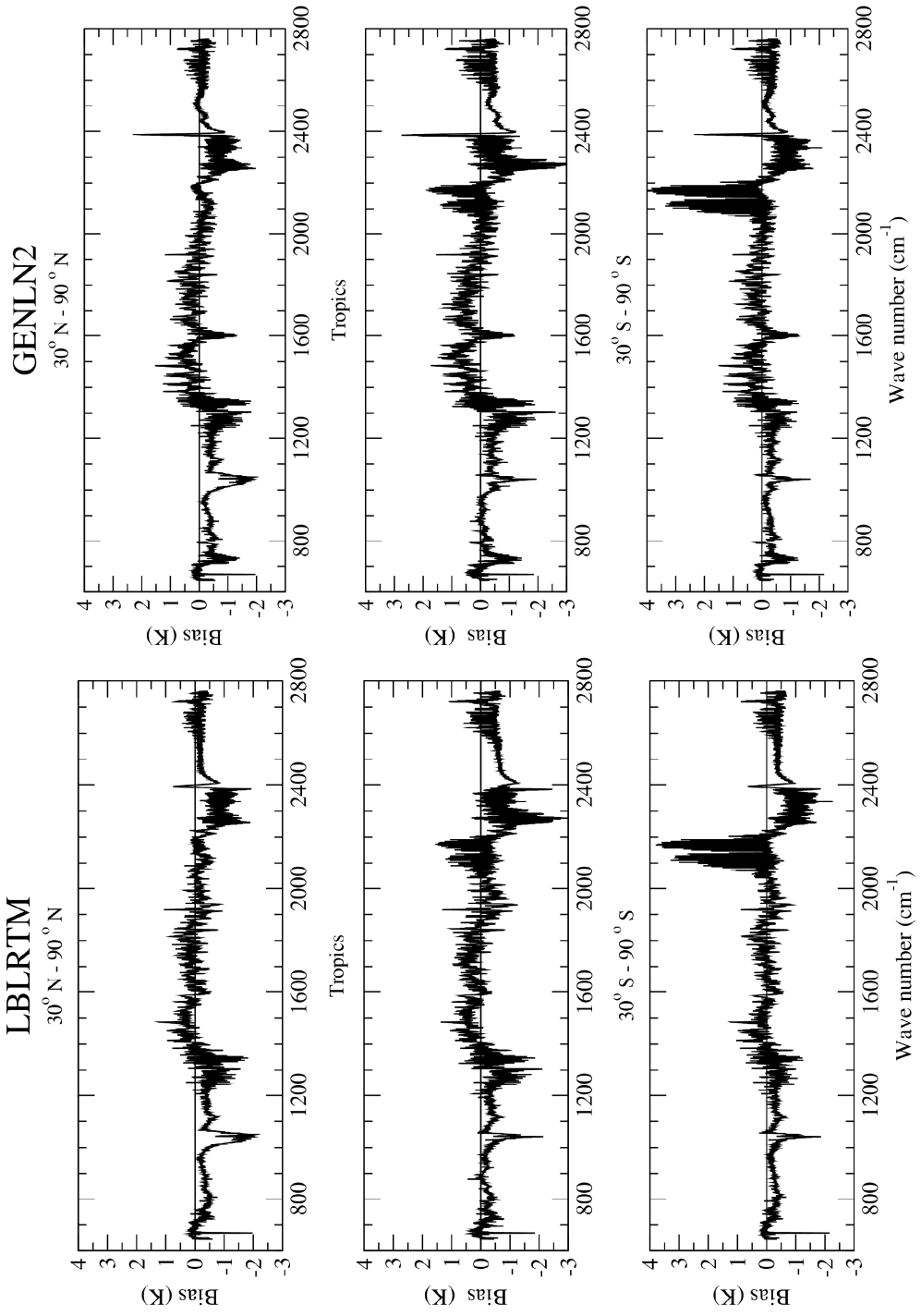

Figure 19A Observed minus simulated IASI radiances using GENLN2 (left panel) and LBLRTM (right panel) from 1-15 April 2008 from the ECMWF T799 model which includes trace gases specified with a climatological distribution. These plots are only for the radiances measured during night and for 3 latitude bands.

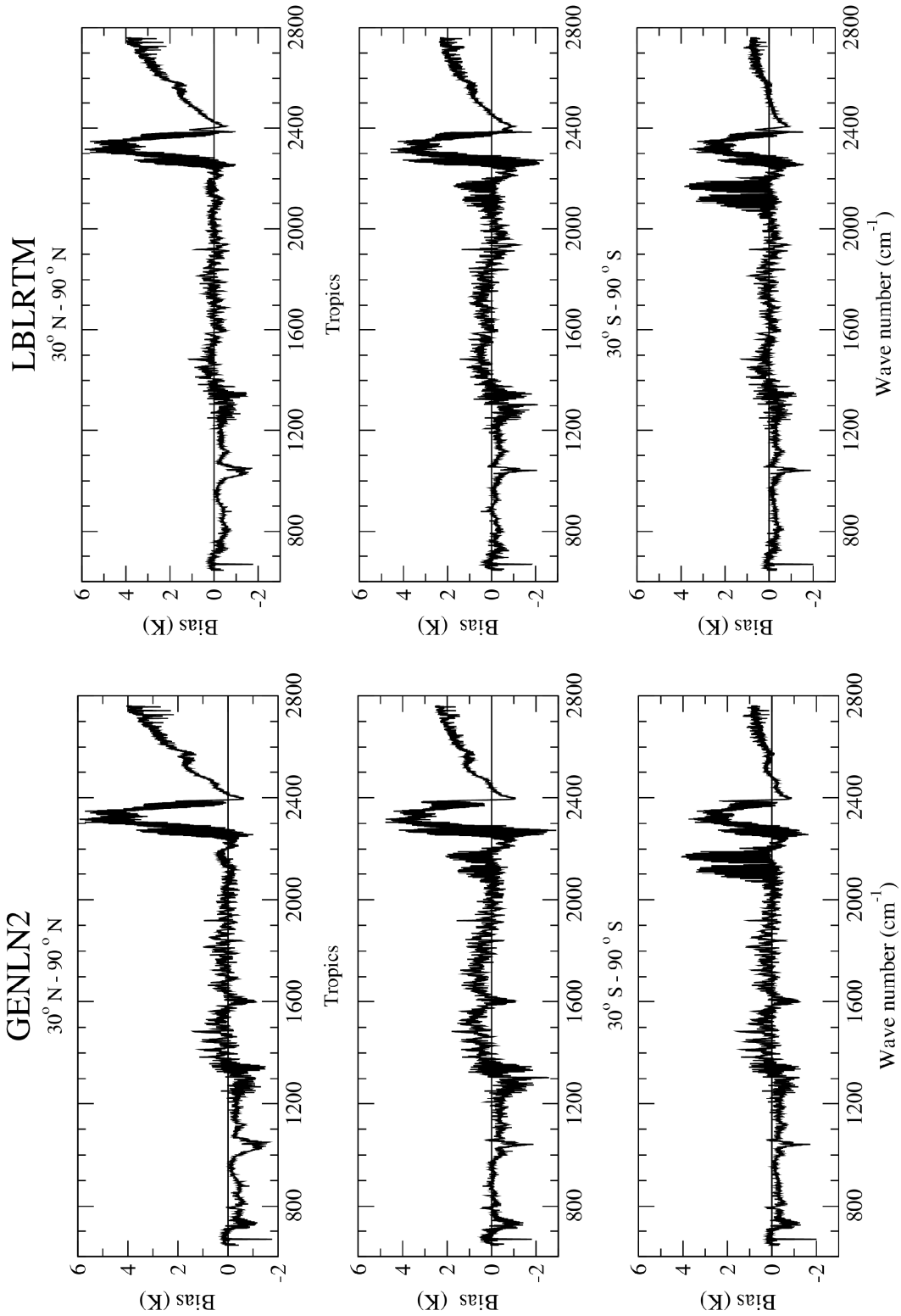

Figure 19b as for 19a but for radiances during the day.

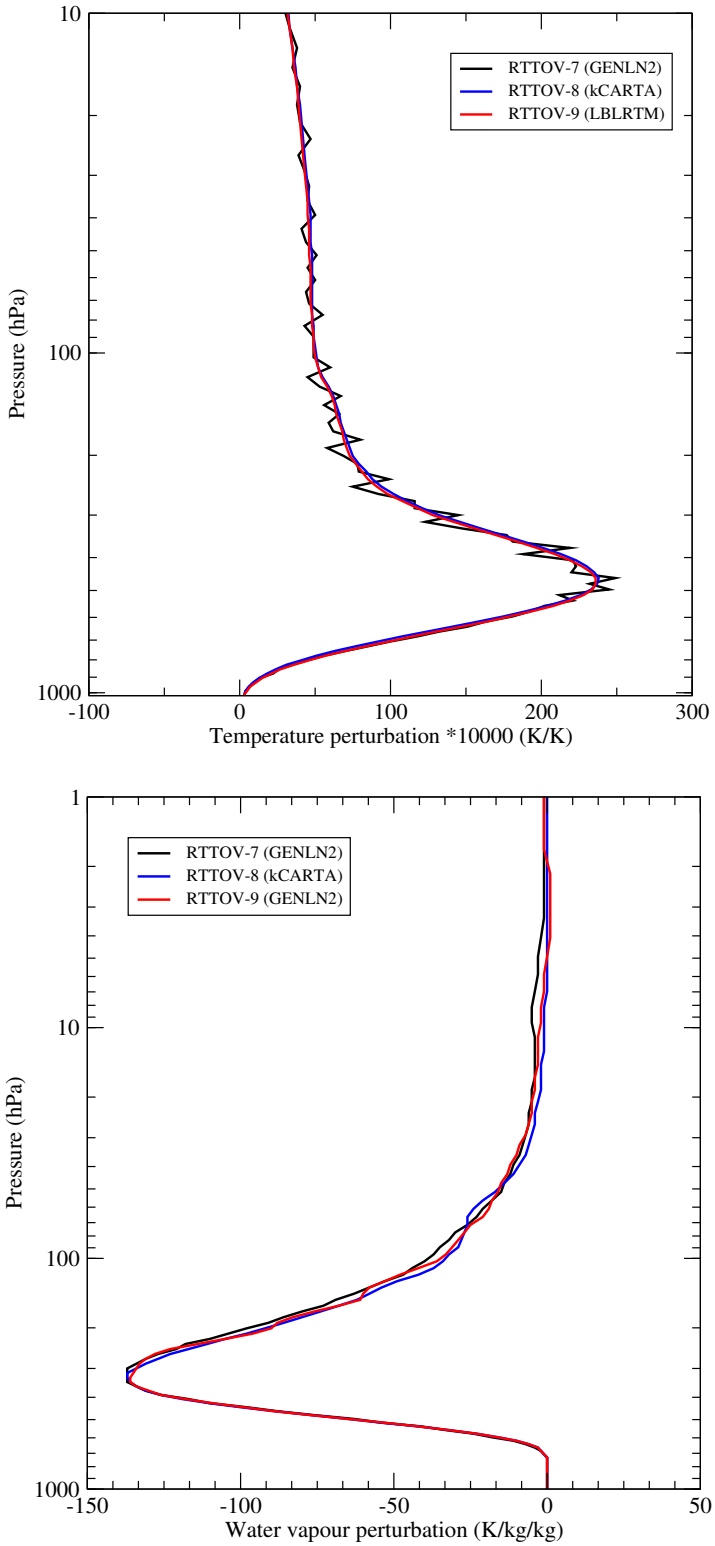

Figure 20. Comparison of IASI temperature Jacobians(top panel) for IASI channel 262 (710.25cm^{-1}) on the AIRS 101 levels. The RTTOV-7 Jacobian was originally on 43L which leads to the wiggles. Comparison of IASI water vapour Jacobians (bottom panel) for IASI channel 3129 (1427.0cm^{-1}) on the AIRS 101 levels.

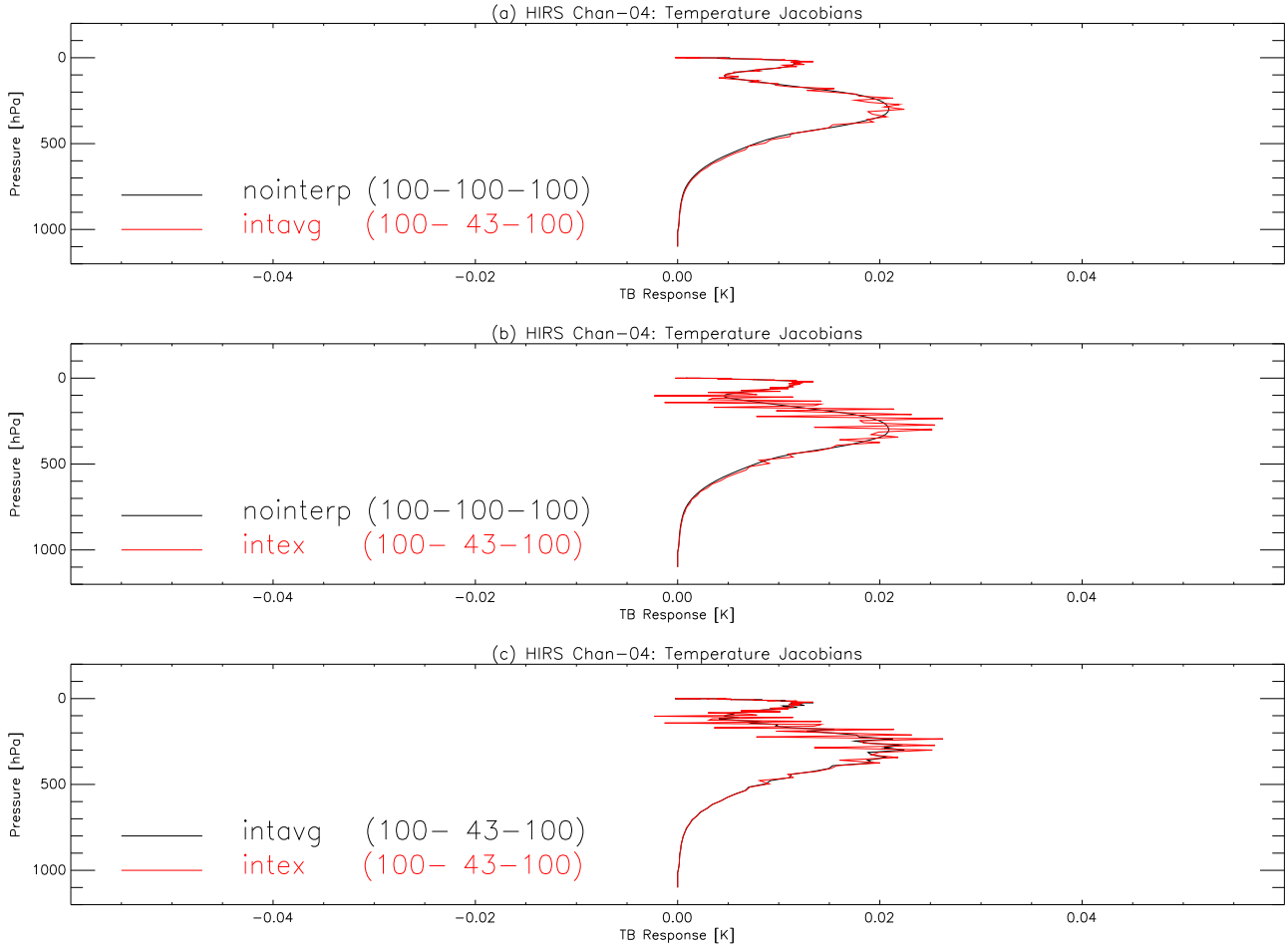

Figure 21. Comparison of temperature Jacobians for a temperature sounding channel of HIRS (channel 4) where the user profile has more levels than the coefficient file (a) RTTOV-9 interpolator vs. no interpolation (b) 'nearest neighbour' interpolator vs. no interpolation (c) the two interpolators.

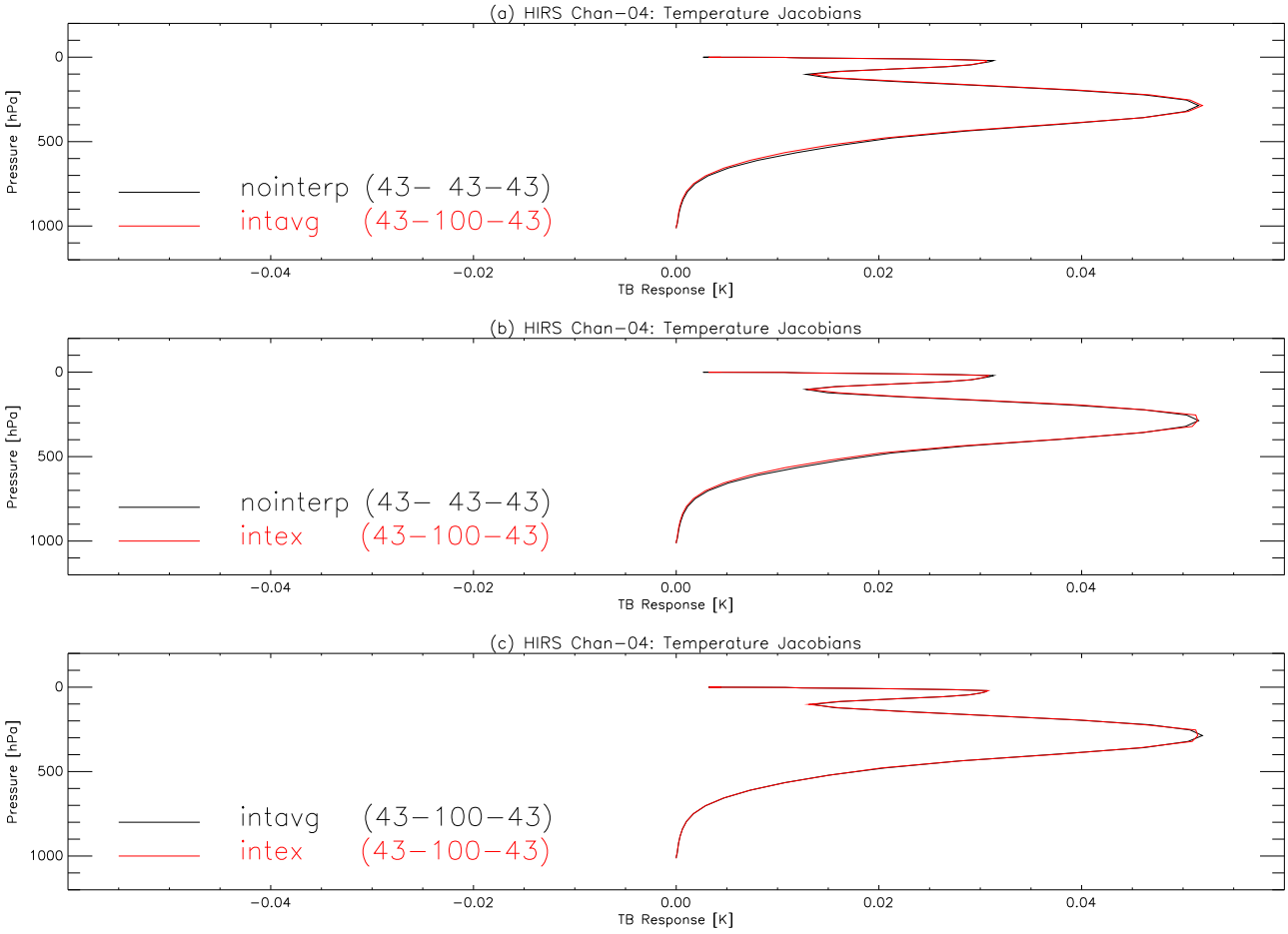

Figure 22. As for Figure 21 but here the user profile has less levels than the coefficient file. Both interpolators use all levels and therefore perform similarly. The amplitude is larger than for Figure 21 because the temperature increments are impressed over thicker layers.

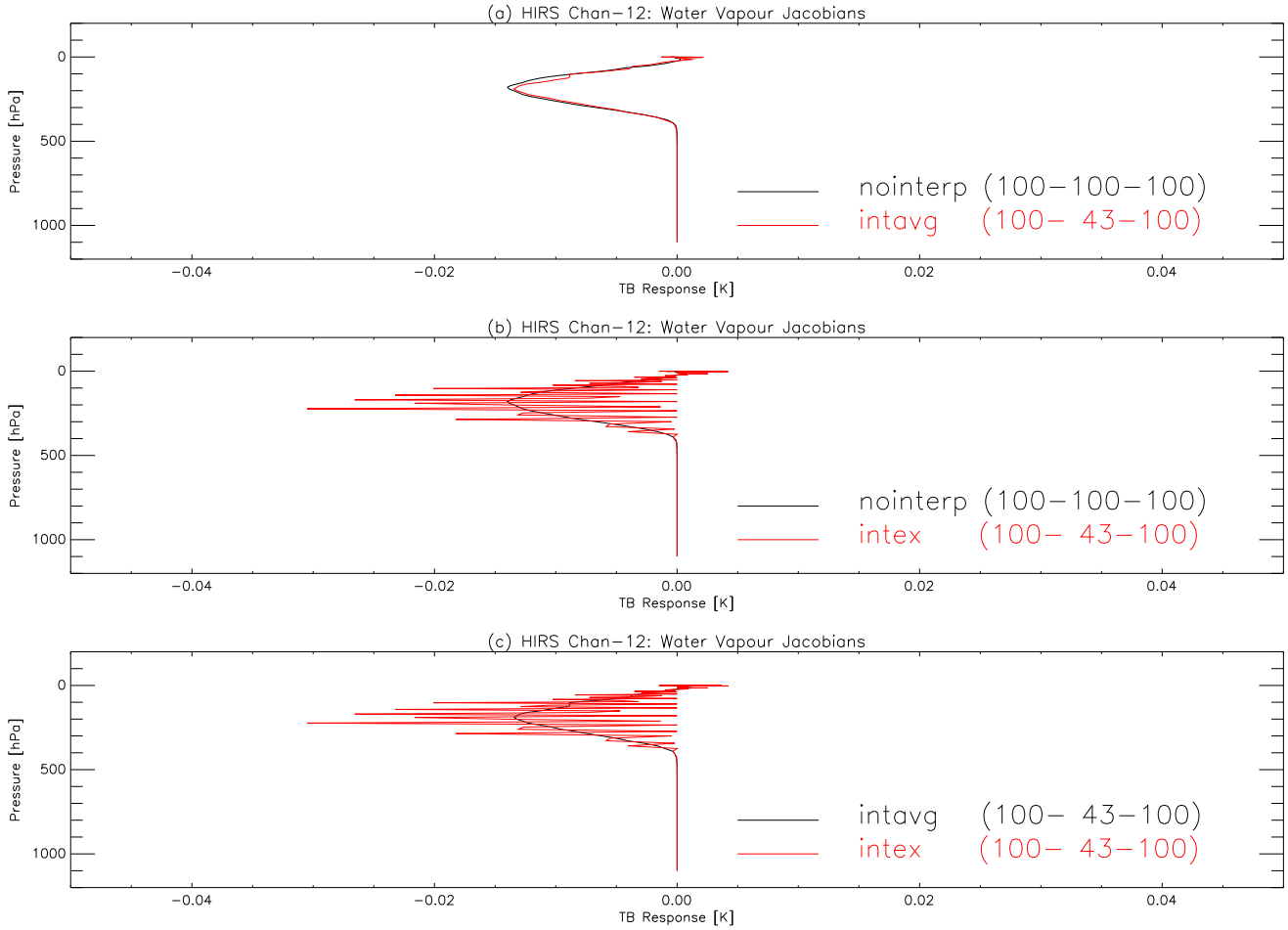

Figure 23. Comparison of water vapour Jacobians for a HIRS channel dominated by water vapour where the user profile has more levels than the coefficient file (a) RTTOV-9 interpolator vs. no interpolation (b) 'nearest neighbour' interpolator vs. no interpolation (c) the two interpolators.

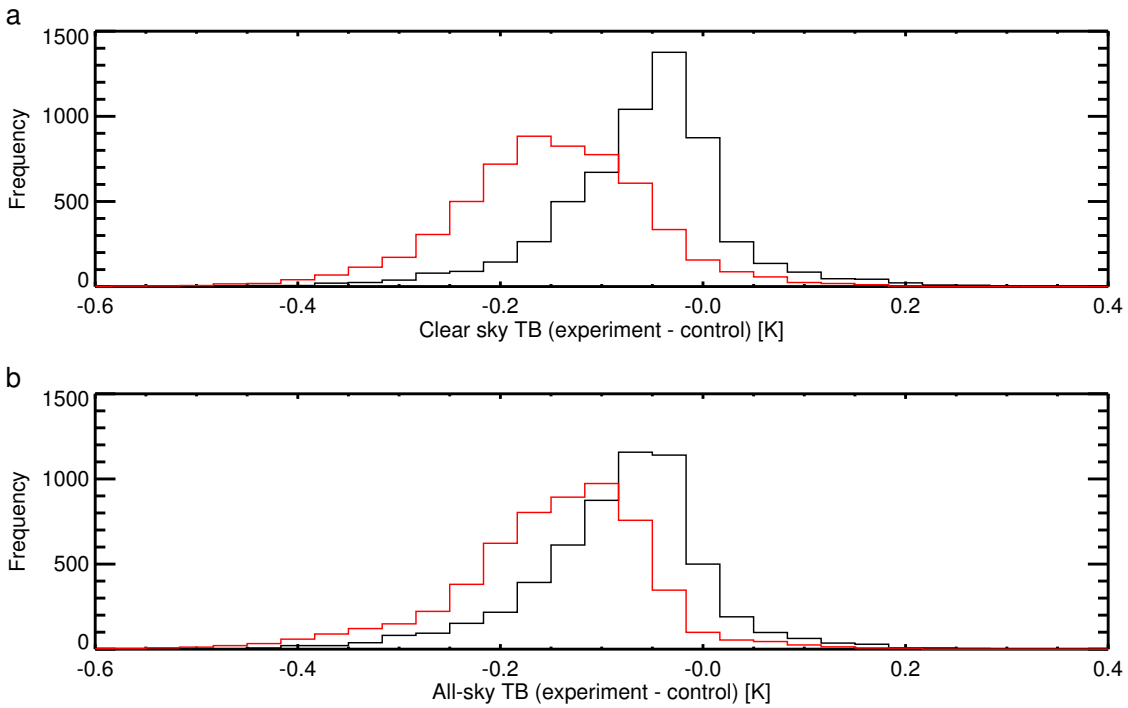

Figure 24. Comparison between RTTOV-87 and RTTOV-91 RTTOV_SCATT computed brightness temperatures for the SSM/I 19v channel. The black line is for the case where the linear in tau changes are disabled in the RTTOV-91 code and the red line is where they are invoked.

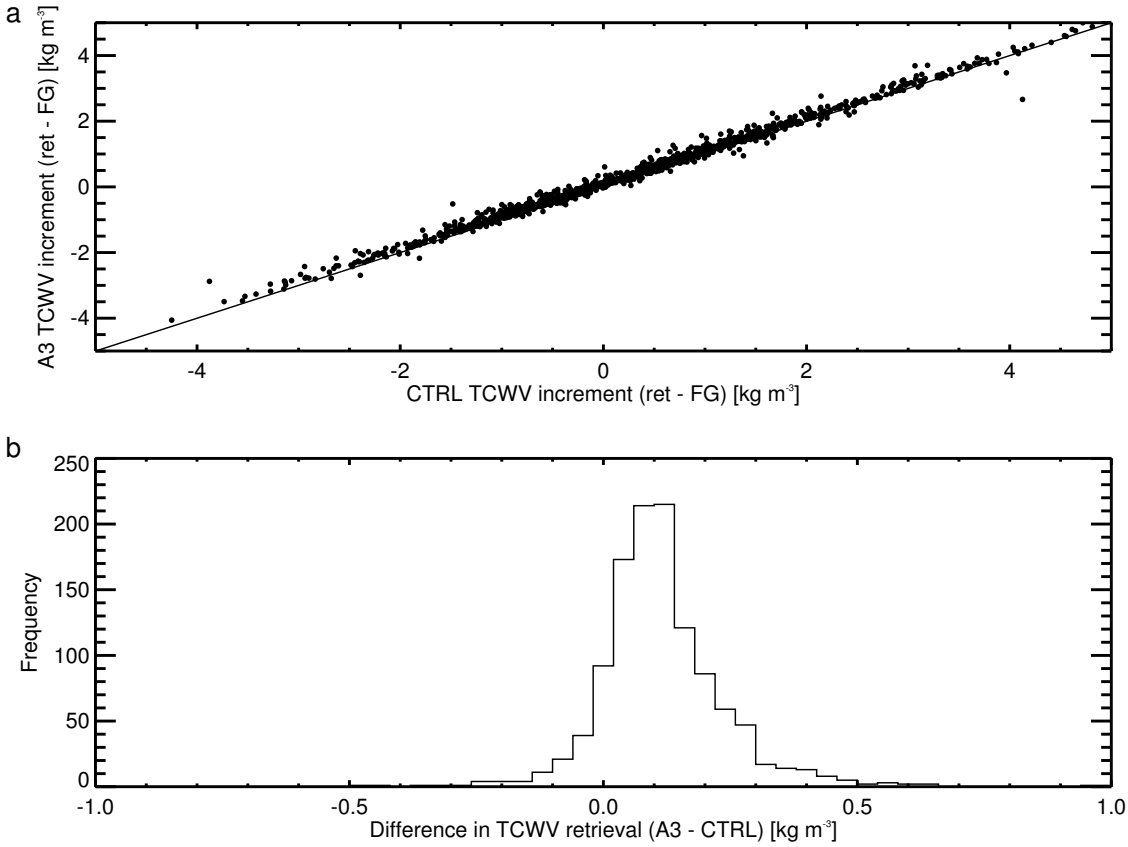

Figure 25. Comparisons between 1D-Var retrievals of total column water vapour in cloudy and rainy areas using the old RTTOV-87RTTOV_SCATT model and the new RTTOV-91 RTTOV_SCATT model.

End of Report